Two-Proton-Spectroscopy in ^{17}Ne

Dissertation der Fakultät für Physik

der

Ludwig-Maximilians-Universität München

vorgelegt von

Marcus J. Chromik

aus Kiel

München, den 27. März 2001

1. Gutachter: Prof. Dr. D. Habs

2. Gutachter: Prof. Dr. M. Thoennessen

Tag der mündlichen Prüfung: 21.5.2001

Meiner Familie

Abstract

In the framework of this thesis a two-proton spectroscopy experiment was performed in order to investigate the excitation and the deexcitation of the low-lying states in ^{17}Ne. Motivation for these investigations was the search for simultaneous two-proton decay (also referred to as "two-proton radioactivity"), since the first excited state ($J^\pi = 3/2^-$, $E^* = 1.288$ MeV) is bound by 192 keV with respect to one-proton emission but unbound with respect to two-proton emission by 344 keV. Therefore this state can decay via a simultaneous two-proton decay to ^{15}O, since the widths of the low-lying states in ^{16}F are too small ($\simeq 40$ keV) for a sequential decay via their tails. However, this two-proton decay is in competition with the γ-decay back to the ground state in ^{17}Ne. In an earlier experiment evidence (limited by the low statistics and resolution) for this long-searched decay mode has been found leaving an unclear picture of the lifetime for this exotic decay mode.

Thus a second experiment at the National Superconducting Cyclotron Laboratory of the Michigan State University was performed, optimized for high detection efficiency of this specific reaction. The exotic (60 MeV/A) ^{17}Ne beam was produced via projectile fragmentation from a (100 MeV/A) ^{20}Ne beam bombarding a ^{9}Be target and further purified with a Wien filter. The low-lying excited states in ^{17}Ne were populated via intermediate energy Coulomb excitation on a ^{197}Au target and two-proton decays of ^{17}Ne were detected in a detector setup not only allowing the complete kinematic detection of all reaction products but also the identification of background reactions, which misled the interpretation of the first experiment.

In the decay energy spectrum of ^{17}Ne sequential two-proton decays from the second excited state in ^{17}Ne ($J^\pi = 5/2^-$, $E^* = 1.764$ MeV) were observed, but no evidence for a simultaneous two-proton decay of the $3/2^-$ state could be found. Monte Carlo simulations were performed in order to extract the resulting cross section for the excitation of the $5/2^-$ state and to use the non-observation of two-proton decays from the $3/2^-$ state to determine a lower limit on the lifetime of the two-proton decay of the $3/2^-$ state in ^{17}Ne. A value of $\tau_{2p} > 26$ ps was obtained, in agreement with theoretical predictions.

From the observed transitions from the $5/2^-$ state and from a previously performed γ-spectroscopy experiment, where the γ-decay of the $3/2^-$ state in

^{17}Ne has been observed which is in competition with the simultaneous two-proton decay, the B(E2) values for the excitation of the $3/2^-$ and the $5/2^-$ state in ^{17}Ne could be derived to $B(\mathrm{E2},^{17}\mathrm{Ne}, 1/2^- \rightarrow 3/2^-) = 66^{+18}_{-25}$ e^{2}fm^4 and $B(\mathrm{E2},^{17}\mathrm{Ne}, 1/2^- \rightarrow 5/2^-) = 124 \pm 18$ e^{2}fm^4, respectively, using the virtual photon method.

The measured B(E2) values were compared to shell model calculations in the context of the weak coupling model. A comparison of results derived with different configuration spaces indicates a break down of the weak coupling model due to the different contributions of the $(\nu p)^{-2}(\nu sd)^2(\pi sd)^2$ and the $(\nu p)^{-3}(\nu sd)^2(\pi sd)^2$ admixtures for ^{18}Ne and ^{17}Ne, respectively. Only recently performed shell model calculations using the full $(\mathrm{p}_{1/2},\mathrm{d}_{5/2},\mathrm{s}_{1/2})^n$ model space could reproduce the data.

Contents

1 Introduction and Motivation **1**

1.1 Two-Proton Decay: A New Two Particle Decay 2

1.1.1 Proton Decay as a Spectroscopic Tool 2

1.1.2 Postulate of the Two-Proton Decay 3

1.2 Candidates for Simultaneous 2p-Decay 5

1.2.1 ^{12}O 5

1.2.2 ^{31}Ar 7

1.2.3 First Evidence for Simultaneous Emission of Two Protons in ^{18}Ne 7

1.2.4 ^{17}Ne: A New Candidate for the Simultaneous Two-Proton Decay? 9

1.2.5 The Mass of ^{17}Ne 10

1.3 Lifetime Calculations for the 2p-Decay 11

1.3.1 The Diproton Model 11

1.3.2 A Lifetime Limit for the Simultaneous Democratic 2p-Decay 11

1.3.3 The Three-Body Breakup Model 12

2 First Experiments on the 2p-Decay of ^{17}Ne 14

2.1 The Competing γ-Decay 14

2.1.1 Lifetime of the Competing γ-Decay 16

2.2 First Search for the Simultaneous 2p-Decay of ^{17}Ne 17

2.2.1 Setup of the First Experiment 17

2.2.2 Data Analysis of the First Experiment 18

2.2.3 Conclusions from the First Experiment 23

2.2.4 Extracted Lifetimes from the Experiment 23

2.3 Comparison of the Lifetime Models with the First Experiment . 24

3 Experimental Setup and Procedure 25

3.1 Production of the ^{17}Ne Beam 25

3.1.1 The A1200 Fragment Separator 26

3.1.2 The **R**eaction **P**roduct **M**ass **S**eparator 28

3.2 Experimental Setup 29

3.2.1 Projectile Identification 30

3.2.2 Projectile Tracking: the CRDC's 30

3.2.3 The Multi Stage Particle Telescope 31

3.3 Electronics 33

3.4 Comparison of the Setups 36

3.5 Experimental Procedure 37

3.5.1 Alignment of the Setup 37

3.5.2 Beam Tuning 37

3.5.3 Calibration Procedure 38

3.5.4 Beam Current and Trigger Rates 39

4 Data Analysis **40**

4.1 Calibration 40

4.1.1 Calibration of the CRDC's 40

4.1.2 Energy Calibration of the Fragment Detectors 43

4.1.3 Energy Calibration of the Proton Detectors 44

4.1.4 Determination of the Experimental Efficiency 47

4.2 Identification of the Reaction Channels 50

4.2.1 Identification of the ^{17}Ne Projectiles 50

4.2.2 Identification of the ^{15}O Reaction Products 51

4.2.3 Identification of the Emitted Protons 53

4.2.4 Identification of 2p-Bands in the First DSSD 57

4.3 Particle Tracking 59

4.3.1 Tracking with the CRDC's 59

4.3.2 Backwards-Tracking with the Proton Detectors 62

4.3.3 Determination of the Breakup Position Along the Beam Axis 63

4.3.4 Comment on the Backtracking 67

4.3.5 Combination of the ΔE- and the Breakup Position Gates 68

4.3.6 Angular Scattering 70

4.4 Decay Energy Spectrum of ^{17}Ne 74

4.4.1 Summary of Applied Gates 74

4.4.2 Effects of the Reaction Point Gates 75

4.4.3 The Decay Energy Spectrum 77

4.4.4 Investigation of the Peak around 900 keV 80

5 Simulation of the Results **82**

5.1 General Description of the PBREAK Code 82

5.2 Ingredients of the Simulation 83

5.2.1 ^{17}Ne 83

5.2.2 Reaction in the Target 83

5.2.3 Particle Detection 84

5.2.4 Generation of the Simulated Data Stream 85

5.3 Simulation Inputs and Performance Tests 85

5.4 Extraction of Properties for the Calculation of the Cross Sections 89

5.4.1 The Simulated Decay Energy Spectrum 89

5.4.2 Detection and Analysis Efficiency 91

5.4.3 Simulation of the Opening Angle of the Detector 94

5.4.4 Extracted Excitation Cross Sections 95

6 Extraction and Discussion of the Results 96

6.1 Lifetime Limit for the Simultaneous 2p-Decay of the $\frac{3}{2}^-$ State. 96

6.2 Extraction of the Experimental B(E2) Values 98

6.2.1 Calculation of the Virtual Photon Numbers 99

6.2.2 Excitation Process of the $\frac{3}{2}^-$ State 99

6.2.3 Excitation Process of the $\frac{5}{2}^-$ State 100

6.3 Discussion 101

7 Outlook 107

7.1 New Goals for Two Proton Spectroscopy Experiments 107

7.2 Future 2p-Spectroscopy Experiments 109

7.2.1 Production Mechanism 110

7.2.2 Setup for Lifetimes τ_{2p} Shorter than $\simeq$5 ns 110

7.2.3 Setup for Lifetimes τ_{2p} Longer than $\simeq$ 500 ns 111

7.2.4 Consequences for the Search for the Simultaneous 2p-Decay in ^{17}Ne 113

List of Figures

1.1 2p-decay modes 4

1.2 Chart of nuclei, Z≥N, Z≤12 6

1.3 Decay scheme of ^{18}Ne 8

1.4 Level scheme of the low-lying states in ^{17}Ne, ^{16}F and ^{15}O 9

1.5 Predictions of the three-body breakup model 12

2.1 The γ-decay of the $\frac{3}{2}^-$ state of ^{17}Ne 15

2.2 Experimental setup for the first search for the 2p-decay 19

2.3 Particle identification 20

2.4 2p-decay energy spectrum derived from the first experiment . . 22

3.1 The A1200 fragment separator 27

3.2 The **R**eaction **P**roducts **M**ass **S**eparator 29

3.3 Overview of experimental setup of the new experiment 30

3.4 The multi stage particle telescope 32

3.5 Electronics setup 34

4.1 Snapshots from the Pad-Signals of the CRDC's 41

4.2 Calibration of the TAC signal of the CRDC's 42

4.3 Fit of the TAC calibration data 42

4.4 Particle identification for the calibration data 43

4.5 Example of the calibration of the fragment detectors 44

4.6 Proton identification for the energy calibration 45

4.7 Energy calibration for a typical element of the CsI-array 46

4.8 Example of calibration characteristics for the DSSD's 46

4.9 Efficiency losses in the particle detectors. 49

4.10 Time-of-flight spectrum 50

4.11 Identification of the ^{15}O reaction products 52

4.12 Identification of the two proton events (I) 53

4.13 Identification of the two proton events (II) 54

4.14 Principle of the hit identification in the DSSD's 55

4.15 Identification of the individual protons 56

4.16 Identification of 2p-bands in the first DSSD 57

4.17 Explanation of the band structure of the first DSSD 58

4.18 Principle of the drift ellipsoid method 60

4.19 Result of the drift ellipsoid method 61

4.20 Principle of the backwards tracking 63

4.21 Comparison of all tracking methods 64

4.22 Determination of the breakup point along the z-axis 65

4.23 Breakup positions along the z-axis for two example cases 66

4.24 Uncertainty of the breakup position along the z-axis 68

4.25 The ΔE and the breakup position gates 69

4.26 Demonstration of the angular scattering effects 71

4.27 Agreement of the identification of straggling events 73

4.28 Effects of the reaction point gates 76

4.29 Transformation error for breakup reaction in the target. 77

4.30 Decay energy spectrum of ^{17}Ne 79

4.31 Investigation of the peak at $\simeq$ 900 keV 81

5.1 Particle ID: data and simulation 87

5.2 Tracking: data and simulation 88

5.3 Determination of the decay energy 91

5.4 Simulated decay energy spectrum 92

5.5 Efficiency curve to detect 2p-decays 93

5.6 Simulation of the Coulomb deflection 94

6.1 Summary of the excitation and deexcitation processes 101

6.2 Configuration space used in the shell model calculations 104

7.1 Proposed setup for future studies of ^{17}Ne 111

7.2 Lifetime limits for the 2p-decay of ^{48}Ni 112

List of Tables

1.1 Input and output of the IMME calculations 10

1.2 2p-decay widths for ^{48}Ni 13

2.1 B(M1) values and lifetimes for the $\frac{3}{2}^- \rightarrow \frac{1}{2}^-$ transition in ^{17}Ne and ^{17}N 16

2.2 Lifetimes for the simultaneous 2p-decay of the $\frac{3}{2}^-$ state in ^{17}Ne . 24

3.1 Settings of the A1200 fragment separator 28

3.2 Geometrical properties of the detectors 33

3.3 Count- and trigger rates 39

4.1 Energy losses in the proton calibration 47

4.2 Detection efficiency in the detectors 48

4.3 Deposited energies in detectors 51

4.4 Range of expected energy losses for the 2p-decay events 52

5.1 Peak position obtained from χ^2-fits. 90

6.1 Properties entering the lifetime calculation 97

6.2 Calculated virtual photon numbers 99

6.3 Comparison of calculated and experimental B(E2) values. 106

Chapter 1

Introduction and Motivation

The existence of bound nuclear systems is limited either by the occurrence of proton or neutron emission from the ground state or by instability against fission for very heavy systems. The boundaries in the nuclear chart on the p- or n-rich side are called driplines. The nuclei beyond the proton- or neutron driplines are unstable with respect to the emission of a proton or a neutron, respectively. The region between the stable nuclei and the neutron dripline opens up a wide area of still unknown nuclei, which are subject of intensive investigations motivating the construction of next-generation of Radioactive Ion Beam facilities all over the world. So far the neutron dripline is only known for oxygen and lighter nuclei. In heavier systems the neutron dripline or even the region of nuclei which are believed to play an important role in the r-process is far from being within reach. This process is one of the mechanisms to explain the nucleosynthesis and the element specific abundances in our universe. Although the proton dripline is reached for nuclei with $Z < 83$ [Woo97, Dav96], nuclei close to the proton dripline pose a variety of questions, e.g. most properties of nuclei which are involved in the rapid proton capture process (rp-process), another mechanism of nucleosynthesis, of are unknown. For those nuclei the knowledge of proton capture cross sections is essential. Moreover, the proton dripline offers the possibility to go beyond to study proton unstable systems and exotic decay mechanisms like the proton decay or even the two-proton decay. The following chapter will briefly discuss the two-proton decay including some examples and cover the basic models to calculate the lifetime of two-proton decays.

1.1 Two-Proton Decay: A New Two Particle Decay

Two particle decay modes are still considered to be an area of substantial experimental and theoretical effort in nuclear physics. In general a two particle decay can be described as a transformation from a nucleus A to a nucleus C without the possibility to populate a state of the intermediate nucleus B. A famous example is the double β-decay, which has received interest due to its possible impact on the understanding of the nature of the neutrino. The double β-decay can occur, when a single β-decay to the neighbouring nucleus is energetically forbidden, while the 2β-decay to the next neighbour is allowed [Fae94]. The current generation of exotic beam facilities opens up a way to study another two particle decay mode, namely the two-proton decay (2p-decay), which can occur in nuclei close to the proton dripline. In the following section this exotic decay mechanism will be explained and compared to the proton decay (sometimes also referred to as proton radioactivity).

1.1.1 Proton Decay as a Spectroscopic Tool

The proton dripline represents one of the fundamental limits for the existence of nuclei. Nuclei beyond the proton dripline are energetically unstable with respect to the emission of a proton. Proton decays (or proton radioactivity) can be observed in nuclei which are particle-stable, if the emission of the proton happens from an excited or isomeric state. Ground state proton emitters by definition are located beyond the proton dripline, neverless allowing to target a variety of questions. Lifetime measurements of proton emitters grant access to detailed spectroscopic information. In contrast to the theory of α-emitters, the proton decay does not have the complication of the preformation factor. Thus, at least for spherical nuclei, the lifetime of a proton emitter reflects the potential built up by the nuclear, the Coulomb and the centrifugal barrier. Since the first two components of the potential are rather well known, the latter one delivers detailed information on the single particle state occupied by the emitted proton of the studied nucleus [Dav96].

The centrifugal barrier as a function of the radial distance is given in practical units by [May83]:

$$V_{\mathrm{L}}(r) = \frac{20.9 l(l+1)}{mr^2}\,[\mathrm{MeV}]\,, \tag{1.1}$$

where r is given in units of fm and the reduced mass m in u. For the Coulomb potential and for $r > R_c$ one obtains

$$V_C(r) = 1.44 \frac{Z_1 Z_2}{r} \,[\mathrm{MeV}]\,, \tag{1.2}$$

where Z_1, Z_2 are the protons numbers of the nuclei and r is the radial distance in units of fm. Since the point-like charge approximation is not valid for very short distances, Eq. (1.2) is replaced for $r < R_c$ by

$$V_C(r) = 1.44 \frac{Z_1 Z_2}{2R_c} \left[3 - \left[\frac{r}{R_c}\right]^2\right] \,[\mathrm{MeV}]\,, \tag{1.3}$$

where R_c, the distance of touching spheres, is given by:

$$R_c = 1.2(A_1^{1/3} + A_2^{1/3}) \,[\mathrm{fm}]\,. \tag{1.4}$$

The probability of tunneling through the barrier is then given by:

$$W_{\mathrm{tunnel}} = \exp\left(-\frac{2}{\hbar}\int_R^{R'} \sqrt{2m\,[U(r) - E]}dr\right), \tag{1.5}$$

where $U(r)$ is the resulting potential and E the Q-value of the reaction. R and R' are the limits for the integration which have to be adapted to the characteristics of the potential. For a more detailed treatment of the potential barriers see [Buc92] and [Mus95]. The example of the discovery of proton radioactivity first observed in ^{151}Lu [Hof82] shows the sensitivity of the barrier penetration probability to the centrifugal barrier, since it was possible to distinguish the proton emitting $h_{11/2}$ single particle state from $s_{1/2}$ or $d_{3/2}$ alternatives.

For deformed proton emitters the picture looks different. The orbital angular momentum l_p of the emitted proton is no longer a good quantum number in the parent nucleus. The calculated lifetimes for proton emission from the deformed nucleus ^{141}Ho [Dav98] (with a deformation parameter of $\beta_2 \simeq 0.3$), assuming a spherical structure result in 1 μs, 10 μs and 37 ms for the $2s_{1/2}$, $1d_{3/2}$ and $0h_{11/2}$ proton orbitals, respectively, and therefore cannot explain the observed halflife of 4.2(4) ms. Obviously, the picture changes dramatically, when tunneling through a deformed barrier opening up a new approach to study deformed nuclei.

1.1.2 Postulate of the Two-Proton Decay

In 1960 Goldansky [Gol60] predicted the existence of a two-proton decay mode which might be observable in nuclei beyond or close to the proton dripline. The two-proton decay might proceed via three possible mechanisms:

(1) SEQUENTIAL 2p-decay: sequential emission of two protons via an intermediate state.

(2) SIMULTANEOUS 2p-decay: no intermediate state is involved in the decay process.

(2a) Uncorrelated ("democratic") emission: the emission of two protons, which may be described as a three-body breakup process.

(2b) Correlated ("diproton") emission: the emission of a ^{2}He cluster with strong proton-proton correlations.

Fig. 1.1 illustrates the essential difference between the simultaneous and the sequential 2p-decay. For the sequential 2p-decay it is necessary that the intermediate state is close enough to the decaying state. Mandatory requirement for a simultaneous 2p-decay is the energetical situation displayed in the left part of Fig. 1.1. The intermediate state is located high enough to guarantee that a decay through this state or its tail is strongly suppressed. The energetical picture is analogue to the situation of the double-β decay. The energetic decay scheme schematically displayed in the right-hand part of Fig. 1.1 does not necessarily exclude a simultaneous decay, however all previous searches for simultaneous 2p-emissions concluded the absence of an intermediate state to be mandatory for the observation of a simultaneous 2p-decay.

For the simultaneous 2p-decay two scenarios are conceivable. In case of a

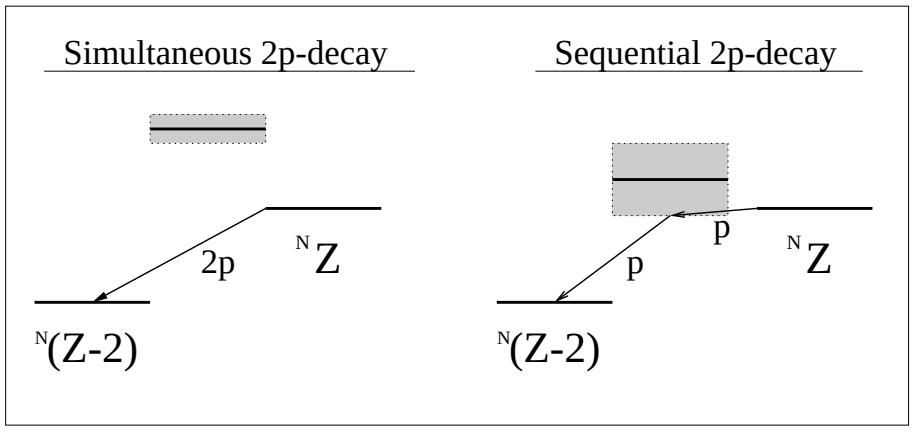

Figure 1.1: The two alternative modes of the 2p-decay: the simultaneous and sequential decay. A simultaneous 2p-decay is possible whenever the ground state of the intermediate system is energetically too high for a decay through that state or its tail.

strong proton-proton correlation one would expect that two protons tunnel as a ^{2}He cluster through the potential barrier before being repulsed from each

other by the Coulomb force. The other extreme case would be a three-body decay (called "three-body decay" or "democratic" in [Gol60]). Experimentally, these two modes could be distinguished by a measurement of the opening angle of the two protons in the center-of-mass system. In case of the simultaneous diproton-like 2p-decay a strong angular correlation would be expected, e.g. very narrow opening angles if the Q-value is sufficiently high. In case of the simultaneous "democratic" 2p-emission the distribution of the opening angle would be isotropic. It should be noted that the definition used for the sequential 2p-decay and the simultaneous 2p-decay is based only on the energetical picture of the decay. This definition is established in the literature and will be used throughout this thesis, although one could argue that a "democratic" 2p-decay which could proceed via a virtual excitation of an intermediate state might not be called simultaneous. Furtheron it should be noticed that the term "two-proton spectroscopy" (2p-spectroscopy) will be used independent of the nature of the 2p-decay.

1.2 Candidates for Simultaneous 2p-Decay

Until recently all searches for a simultaneous 2p-decay have shown evidence for sequential emissions only [Chr97]. In most cases follow-up experiments were needed to clarify the situation. In the following section ^{12}O and ^{31}Ar will be discussed as prototypes for these investigations. In both cases the search for the simultaneous 2p-decay also demonstrated the usefulness of proton- and two-proton spectroscopy in order to obtain structural information beyond the driplines. The third example ^{18}Ne discusses the first known case of a simultaneous emission of two protons from an excited state. A similar situation is given for ^{17}Ne, another candidate for a simultaneous 2p-decay from an excited state. Fig. 1.2, accordingly, shows a part of the nuclear chart for nuclei with Z>N and Z$\leq$12 together with the proton dripline.

1.2.1 ^{12}O

For a long time ^{12}O was considered to be a promising candidate for a ground state (g.s.) simultaneous 2p-emitter, since the mass of the intermediate system ^{11}N (g.s.) + p was assumed to be energetically located about 0.2 MeV above the ground state of ^{12}O. Although the ground state in ^{11}N was predicted to have a relatively large width ($\Gamma \simeq$1.5 MeV), a sequential 2p-decay was expected to be strongly suppressed (see [Ajz91]). Between 30% and 90% of the

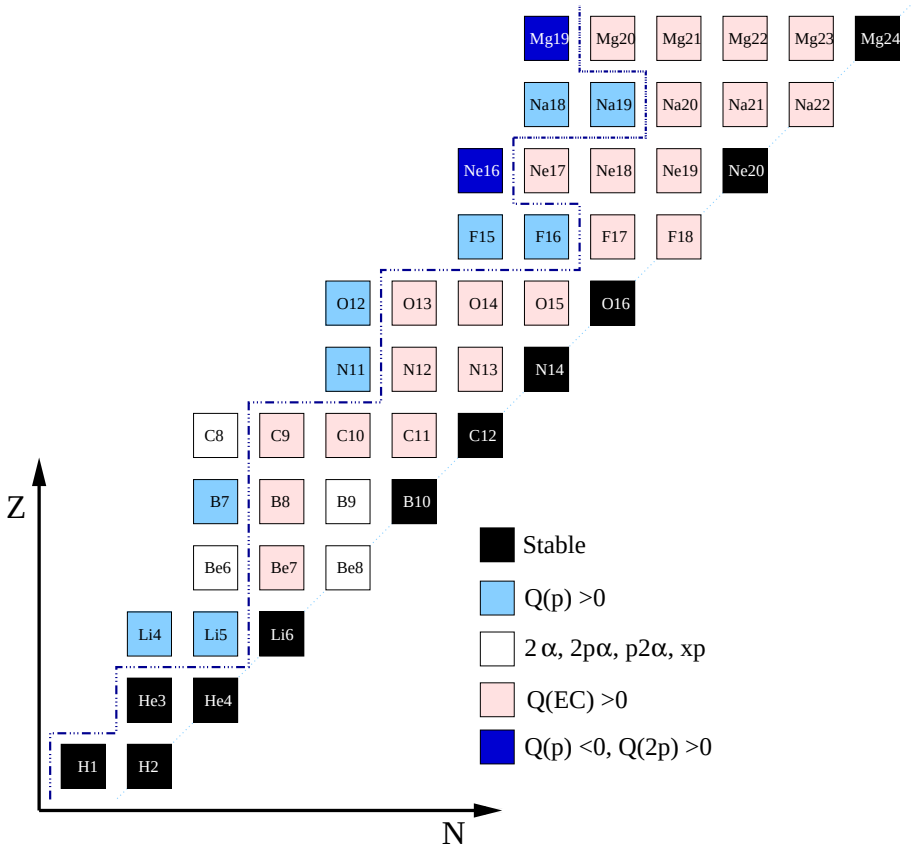

Figure 1.2: Low-Z part of the nuclear chart. Only nuclei with Z≥N, Z≤12 are shown. The dashed-dotted line represents the proton dripline. The light proton emitters are shown in light blue. ^{16}Ne and ^{19}Mg in their ground state are expected to be bound with respect to the emission of one proton but unbound with respect to the emission of two protons. ^{17}Ne and ^{18}Ne are particle stable in the ground state but candidates for the simultaneous 2p-decay from an excited state, as will be shown later. ^{6}Be and ^{12}O turned out to be sequential 2p-emitter.

decay strength was predicted to be associated with a simultaneous 2p-decay. Measurements of Kryger et al. [Kry95] led to the conclusion that the decay proceeds completely sequential, which could be only explained either by an unrealistically large width of the ground state in ^{11}N or by a lower-lying ground state for ^{11}N. Indeed, new measurements revealed that the ground state of ^{11}N lies about 0.5 MeV lower than expected before [Azh98a, Oli00, Mar00]. Thus the sequential decay was energetically allowed [Azh98b]. It should be noted here that an experimental distinction between the simultaneous democratic mode and the sequential mode was not possible in this case. The angular distribution of the opening angle of the protons in the center-of-mass frame is expected to be isotropic in both cases. The difference of the kinetic energies of

the two emitted protons in the cm-system would be expected to peak around zero in case of the simultaneous democratic mode (three-body breakup), because due to an equal distribution of phase space between the two protons, they would be emitted with almost the same energy as already mentioned by Goldansky [Gol60]. In case of the sequential 2p-decay through an intermediate state (here the ground state in ^{11}N) one would expect the kinetic energies of the two protons in the cm-system to be 0.33 MeV and 1.45 MeV, respectively. However, since the ground state width of ^{11}N is that large ($\Gamma \simeq$1.5 MeV) the maximization of phase space has a larger impact on the distribution of the decay energy between the two protons.

1.2.2 ^{31}Ar

^{31}Ar is an example for a β-delayed two-proton emitter. The 2p-emission follows the β-decay to the isobaric analogue state (IAS) in ^{31}Cl [Baz92]. The 2p-decay was studied and three decay lines with weak statistics could be identified [Muk98]. The main argument for a simultaneous democratic 2p-decay was found in the absence of evidence for distinct decay steps in the two-dimensional plot of the proton energies. Besides the weak statistics, a possible presence of intermediate states in ^{30}S is not discussed in [Baz92] and [Muk98]. So far, only a few states in ^{30}S are known in the relevant energy region. However, a comparison with the mirror nucleus ^{30}Si [ToI96] gives rise to the expectation of a large number of (yet unobserved) intermediate states allowing for a sequential decay pattern in ^{31}Ar. The use of a highly segmented setup in a recent experiment indeed proved the existence of nuclear levels in ^{30}S up to an excitation energy of 8 MeV [Fyn00], thus leading to a completely sequential decay pattern for the 2p-decay in ^{31}Ar. This recent experiment on ^{31}Ar and ^{30}S is a conclusive example demonstrating how the method of 2p-spectroscopy can be used as a powerful tool to study nuclei far from stability.

1.2.3 First Evidence for Simultaneous Emission of Two Protons in ^{18}Ne

Recently the simultaneous emission of two protons from a resonance in ^{18}Ne was observed with the reaction ^{17}F+p [Gom01]. A low-energy radioactive ^{17}F beam with 33 MeV and 44 MeV was impinched on a 40 μm thick (CH_2) target. Initially, the experiment was designed to study the 3^+ state in ^{18}Ne by observing single-proton emission out of the resonance in ^{18}Ne. The level

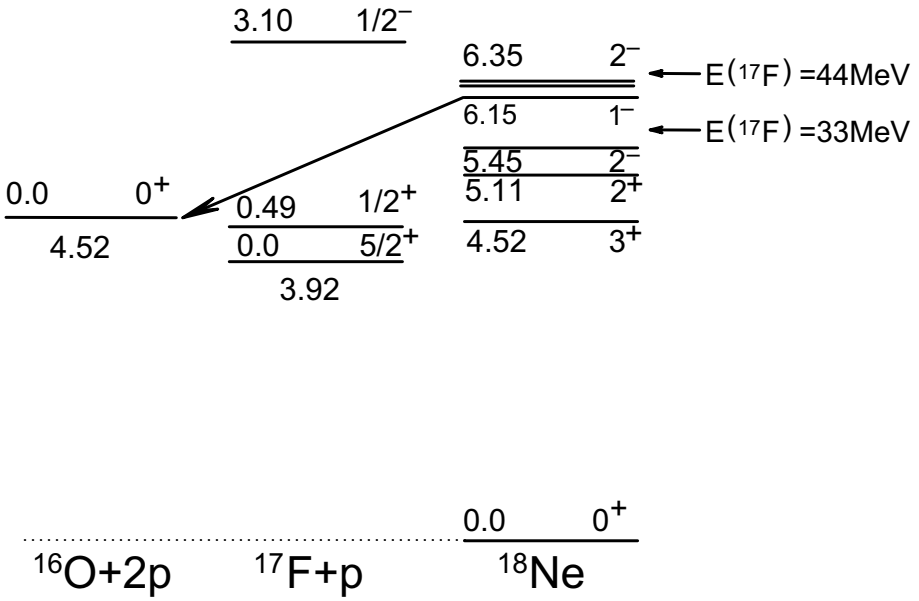

Figure 1.3: Decay scheme of ^{18}Ne, taken from [Gom01]. The arrow indicates the observed two-proton emission. No intermediate states in ^{17}F are present. The two arrows on the right indicate which levels can be populated with the two incident beam energies. The simultaneous two-proton emission was only observed for the beam energy of 44 MeV and not at 33 MeV as expected.

scheme is shown in Fig. 1.3. The target stopped the fluorine ions, however, the protons penetrated the target and were detected in a double sided strip detector. In addition to single-proton emissions also two-proton emissions were observed, yet only for incident beam energies of 44 MeV. This was interpreted as an evidence for a decay out of the ($J^\pi = 1^-$, $E^* = 6.15$ MeV) state in ^{18}Ne, which would not be populated with the incident energy of 33 MeV. As a critical comment to these data it can be stated that the thick target [Gom01] used here limited the energy resolution of the protons. Moreover, the data did neither allow to reconstruct the decay energy spectrum nor to study the individual center-of-mass energies of the protons and their energy difference. The only energy to be measured was the relative energy of the protons in the laboratory frame which was compared to Monte Carlo simulations for a diproton emission. The easiest way to obtain a better energy resolution would be to use a much thinner target, aiming at an exclusive population of the 1^-state in ^{18}Ne. This would eliminate all the uncertainties of the interaction point in the target, the energy loss straggling and the angular straggling, therefore allowing to distinguish between diproton emission and three-body breakup reactions.

1.2.4 ^{17}Ne: A New Candidate for the Simultaneous Two-Proton Decay?

Measurements of the levels in ^{17}Ne with the three neutron pickup reaction ^{20}Ne(^{3}He,^{6}He)^{17}Ne [Gui95, Gui98] showed that the first excited $\frac{3}{2}^-$ state in ^{17}Ne is bound with respect to the one-proton emission to ^{16}F, but unbound with respect to the two-proton emission to ^{15}O. Thus, this state is a potential

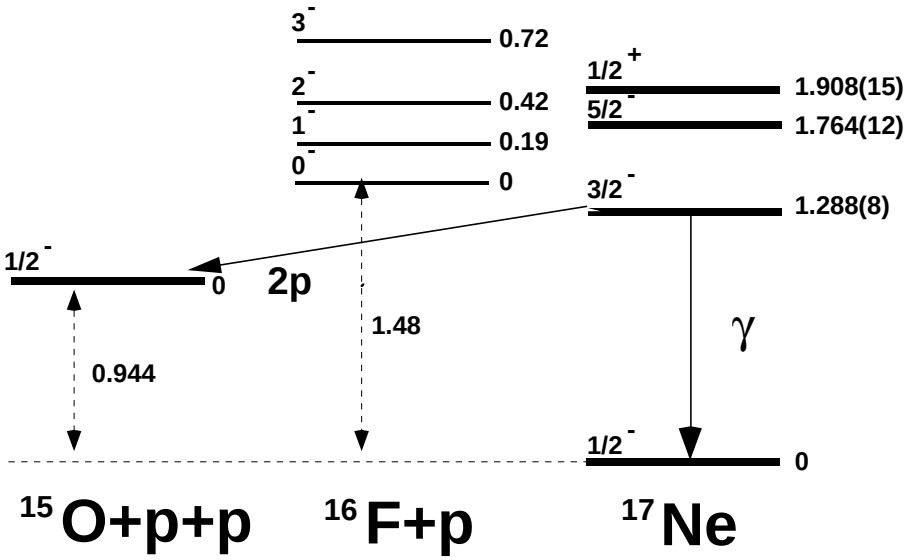

Figure 1.4: Level scheme of the low-lying states in ^{17}Ne, ^{16}F and ^{15}O. From the first excited state in ^{17}Ne an open decay channel for a simultaneous 2p-decay exists, which is in competition with the γ-decay back to the ground state in ^{17}Ne. The levels are taken from [Gui98, Ajz91, Til93].

candidate for simultaneous two-proton emission. However, this decay mode has to compete with the γ-ray decay back to the $\frac{1}{2}^-$ ground state of ^{17}Ne. Fig. 1.4 shows the expected decay scheme including the low-lying states of ^{17}Ne, ^{16}F and ^{15}O. The spins and parity assignments are derived from the mirror nucleus ^{17}N and the isobaric mass multiplet equation [Gui95, Gui98]. The mass of ^{16}F (g.s.) plus a proton is about 200 keV above the first excited state in ^{17}Ne, while the widths of the low-lying states in ^{16}F are rather narrow ($\Gamma \simeq 40$ keV) and should not allow for a sequential decay. Hence, ^{17}Ne is a promising candidate for the observation of a simultaneous two-proton emission. However, the Q-value for the simultaneous 2p-decay is with 344 keV rather small and strongly dependent on the mass of ^{17}Ne. Therefore the mass of ^{17}Ne will be discussed briefly in the following section.

1.2.5 The Mass of ^{17}Ne

Any calculation for the simultaneous 2p-decay is very sensitive to the respective Q-value. The presently available mass measurements give 0.344±0.050 MeV, where the error is derived from an old ^{20}Ne(^{3}He,^{6}He)^{17}Ne transfer experiment [Men70, Aud97]. Alternatively we can use the isobaric multiplet mass equation IMME [Ben79] to extrapolate the binding energies of the states in ^{17}Ne based upon the energies of their analog states in ^{17}N, ^{17}O and ^{17}F [Til93, ToI96]. The mass excess of ^{17}N, ^{17}O and ^{17}F is fitted by a quadratic function as a function of the third projection of the isospin and the resulting fit parameter are used to predict the mass excess of ^{17}Ne. No cubic term is used (d=0). Table 1.1 summarizes the input values for the IMME calculation and the output. The IMME calculations reproduce the mass excess for ^{17}Ne of $\Delta_{^{17}\mathrm{Ne}} = 16490(50)$ keV [ToI96] and the obtained energies for the excited states are in good agreement with each other.

State	$\Delta(^{17}\mathrm{N})$ [keV]	$\Delta(^{17}\mathrm{O})$ [keV]	$\Delta(^{17}\mathrm{F})$ [keV]	$\Delta(^{17}\mathrm{Ne})$ [keV]	E_{Exc} [keV]
$\frac{1}{2}^-$	7871.0(±15.0)	10269.7±0.9	13144.6±3.4	16496±21	0
$\frac{3}{2}^-$	9244.9(±15.0)	11657.0±1.0	14501.8±2.7	17779±20	1284
$\frac{5}{2}^-$	9720.6(±15.0)	12135.0±5.0	15012.7±4.7	18248±22	1753
$\frac{1}{2}^+$	9777.8(±15.0)	12189.2±1.0	15031.7±4.7	18411±27	1915

Table 1.1: Input and output (mass excess Δ) of the IMME calculations aiming at the mass of ^{17}Ne.

1.3 Lifetime Calculations for the 2p-Decay

In the following section the main models for 2p-decays will be discussed.

1.3.1 The Diproton Model

The 2p-decay width is given in general by the product of the widths obtained from the barrier penetration calculations and the spectroscopic factor. The latter can be be seen as a measure of the probability of the nucleus being in a certain configuration from which a certain decay can proceed. The model of the diproton emission can be used for a lifetime calculation of the 2p-decay. In a simple approximation the decay width for ^{17}Ne can be estimated based upon the penetration of a point-like diproton cluster through a Coulomb barrier for a particle of charge Z=2 and a core with charge Z=8. The width was obtained by calculating the phase shift for the scattering of a diproton from a potential of radius 3.0 fm and diffuseness of 0.6 fm with a well depth constrained to give a resonance peak at 0.344 MeV. The total orbital angular momentum for the $\frac{3}{2}^- \rightarrow \frac{1}{2}^-$ decay must be $L_{\mathrm{total}} = 2$. In the cluster model [Any74, Bro91], the diproton is described as an s-state ($\ell = 0$) and the relative angular momentum between the diproton and the $A = 15$ core is $L = 2$. The calculated decay width is $\Gamma_{L=2} = 1.6 \cdot 10^{-12}$ MeV, translating into a lifetime of $\tau_{2\mathrm{p},L=2,l=0} = 411$ ps. An alternative scenario would comprise a simultaneous 2p-decay with $\ell = 2$ and $L = 0$, resulting in a 2p-decay width of $\Gamma(L = 0) = 4.2 \cdot 10^{-11}$ MeV ($\tau_{2\mathrm{p},L=0,l=2} = 16$ ps). The spectroscopic factors associated with the simultaneous 2p-decay of the first excited state in ^{17}Ne can be obtained from the p-sd shell-model wave functions [War92]. The two-nucleon decay amplitudes obtained with the WBP and WBT wave functions are dominated by large $(0d_{5/2})^2$ and $0d_{5/2} - 1s_{1/2}$ components (where $0d_{5/2}$ and $1s_{1/2}$ are the shell-model single-particle angular momentums). The way in which these components enter into the decay width will depend on the dynamics of the decay, but the spectroscopic factors to be associated with both $L = 0$ and $L = 2$ decays should be on the order of unity [Bro01].

1.3.2 A Lifetime Limit for the Simultaneous Democratic 2p-Decay

According to [Gol60] a genuine signal of two proton emission would be an "energy correlation between the two protons, during the two-proton decay, which leads to their energies being almost equal." Hence, in order to estimate

the lifetime for an uncorrelated emission of two protons, the Q_{2p} value should be equally distributed between the two protons before tunneling through the barrier. In order to obtain the total decay width the barrier penetrabilities of the two protons have to be multiplied. For the special case of an angular momentum $l = 0$ it can easily be verified that the tunneling probability is equal to that of a diproton with $L = 0$, taking into account that only the Coulomb potential (see Eq. (1.2) and (1.3)) contributes to the tunneling probability (Eq. (1.5)) and reminding that $Z_{\mathrm{diproton}} = 2 \cdot Z_{\mathrm{uncorr.}}$, $E_{^2\mathrm{He}} = 2 \cdot E_{\mathrm{uncorr.}}$ and $m_{^2\mathrm{He}} = 2 \cdot m_{\mathrm{uncorr.}}$. Therefore:

$$W_{\mathrm{tunnel},^2\mathrm{He}} = W_{\mathrm{tunnel,p}} \cdot W_{\mathrm{tunnel,p}}. \tag{1.6}$$

For the case of the 2p-decay of the first excited state of ^{17}Ne a lifetime of ($\tau_{2\mathrm{p},(d^2)} = 1.4\mu$s) and ($\tau_{2\mathrm{p},(sd)} = 1.8$ ns) is obtained, considering the protons being emitted from a d^2 configuration or a (sd) configuration, respectively.

1.3.3 The Three-Body Breakup Model

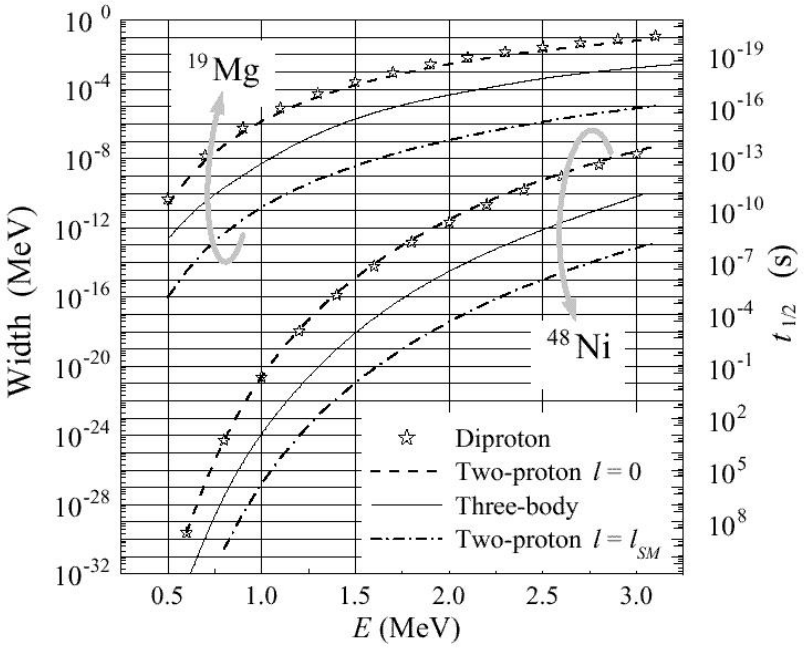

Figure 1.5: Prediction of the three-body breakup bodel for ^{19}Mg and ^{48}Ni. Plotted is the decay width versus the Q-value. Taken from [Gri00].

Recently, Grigorenko et al. [Gri00] developed a first three-body breakup model for the case of 2p-radioactivity. Fig. 1.5 shows the decay width Γ as a function

of the Q-value for the alternative candidates for a simultaneous 2p-decay ^{19}Mg and ^{48}Ni, which will be discussed in the sections 7.2.2 and 7.2.3, respectively. For each of the nuclei four different curves are shown: The stars represent the calculation for a diproton decay with $L = 0$, the solid curve the three-body breakup model. The other two curves correspond to the uncorrelated emission with $l = 0$ (dashed) and $l = l_{\mathrm{sm}}$ (dashed-dotted), where l_{sm} is the angular momentum of the dominant shell configuration occupied by the valence protons. The results for the diproton decay with $L = 0$ and the uncorrelated emission with $l = 0$ are almost equal, as discussed in section 1.3.2. The graph suggests that the three-body breakup model leads to results which are somehow in between the extreme cases of zero angular momentum and $l = l_{\mathrm{sm}}$. For the simultaneous 2p-decay from the $\frac{3}{2}^-$ state in ^{17}Ne with a decay energy of 344 keV [Gri00] quotes a width of $1.4(3)\times\ 10^{-15}$ MeV corresponding to a lifetime of 470(100) ns.

To be able to compare the decay width given by [Gri00] for the three-body breakup with the values obtained with the other two models (see sections 1.3.2 and 1.3.1) the simple barrier penetration code was used to reproduce the decay widths given for ^{48}Ni in [Gri00] for the diproton decay and the uncorrelated decay with $l = l_{\mathrm{sm}}$. As can be seen in Tab. 1.2 the agreement is good.

Q-value [MeV]	$\Gamma(^2$He,$l = 0)$ [MeV]	Γ(uncorr.,$l = 3$) [MeV]	$\Gamma(^2$He,$l = 0)$ [MeV]	Γ(uncorr.,$l = 3$) [MeV]
1.0	$\simeq 2 \times 10^{-21}$	$\simeq 1 \times 10^{-27}$	1.9×10^{-21}	1.19×10^{-27}
1.5	$\simeq 1 \times 10^{-15}$	$\simeq 1 \times 10^{-21}$	8.7×10^{-16}	1.48×10^{-21}
2.0	$\simeq 2 \times 10^{-12}$	$\simeq 2 \times 10^{-18}$	1.95×10^{-12}	6.93×10^{-18}
	[Gri00]	[Gri00]	this work	this work

Table 1.2: Comparison of the calculated 2p-decay widths for ^{48}Ni by [Gri00] with the results from the code used in this work. This table basicly served as a consistency check and to ensure that the 2p-lifetime for ^{17}Ne given by the three-body breakup model can be compared with the other models described in sections 1.3.2 and 1.3.1.

Chapter 2

First Experiments on the 2p-Decay of ^{17}Ne

In the following sections, the first experimental attempts to study the excitation and deexcitation of ^{17}Ne will be described. A more detailed description of those experiments can be found in [Chr97, Chr98a].

2.1 The Competing γ-Decay

In a first experiment the competing γ-decay of the $\frac{3}{2}^-$ state in ^{17}Ne was studied via intermediate energy Coulomb excitation. The radioactive ^{17}Ne beam with 60 MeV/A was impinched on a 532.7 mg/cm^2 ^{197}Au-target and the emitted γ-rays were detected in a position-sensitive, highly efficient NaI array. Fig. 2.1 (top) shows the measured γ-spectrum in the target rest frame where one can see a peak around 547.5 keV correlated to the $\frac{7}{2}^+ \rightarrow \frac{3}{2}^+$ transition in the ^{197}Au target. In the region around 1.3 MeV, where the decay of the first excited state of the ^{17}Ne projectile is expected, only a broad enhancement is visible. The same spectrum appears in Fig. 2.1 (bottom) after the Doppler-shift correction into the projectile rest frame (β =0.317). While the transition from the ^{197}Au target broadens, a peak at (1275 $\pm$ 22 keV) appears. This energy is consistent with the $\frac{3}{2}^-$ state observed in the ^{20}Ne(^{3}He,^{6}He)^{17}Ne reaction [Gui95]. The measured yield from the γ-decay accounts only for 43^{+19}_{-14}% of the predicted yield of an excitation cross section of 28$\pm$6 mbarn, which was calculated using the virtual photon method in the approach for intermediate energies as described in [Ber88]. The photo absorption cross section is given by

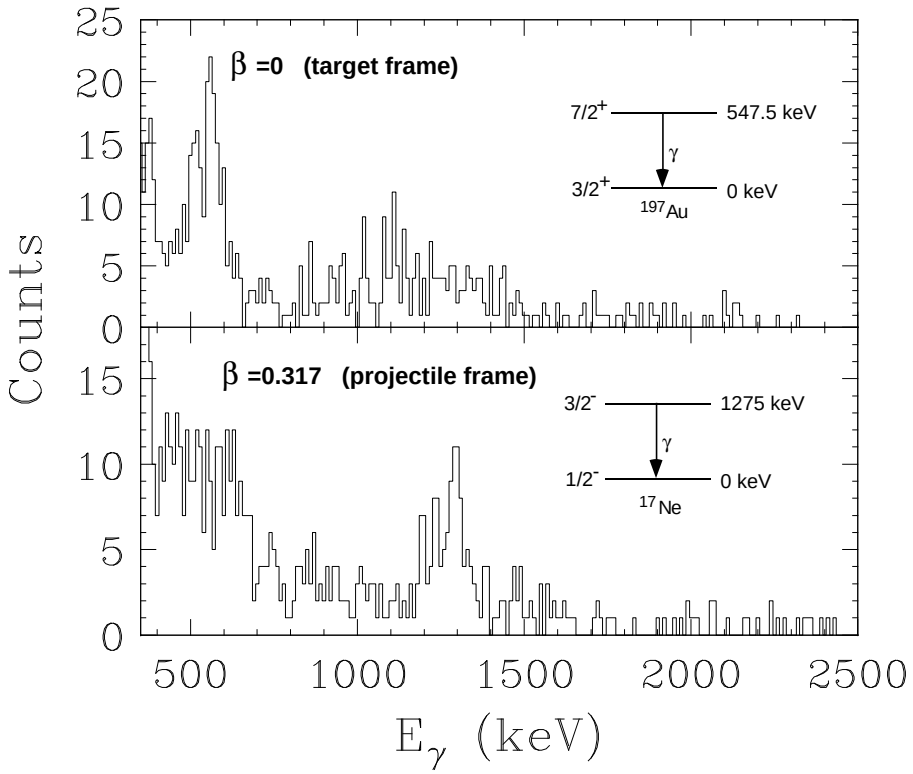

Figure 2.1: γ-ray spectra following the reaction ^{17}Ne + ^{197}Au in the target rest frame (top) and the projectile rest frame (bottom). In the target rest frame the $\frac{7}{2}^+ \rightarrow \frac{3}{2}^+$ transition in the ^{197}Au target can be identified, in the projectile rest frame the $\frac{3}{3}^- \rightarrow \frac{1}{2}^-$ transition in the ^{17}Ne projectile becomes visible.

$$\sigma_{ex} = n_{\mathrm{E2}} \cdot \sigma_\gamma^{\mathrm{E2}} + n_{\mathrm{M1}} \cdot \sigma_\gamma^{\mathrm{M1}} \tag{2.1}$$

where n_{E2} and n_{M1} are the number of virtual photons and $\sigma_\gamma^{\mathrm{E2}}$ and $\sigma_\gamma^{\mathrm{M1}}$ the photon absorption cross sections for the E2 and the M1 excitation, respectively. The photo absorption cross sections $\sigma_\gamma^{\mathrm{E2}}$ and $\sigma_\gamma^{\mathrm{M1}}$ are directly proportional to the B(E2) and the B(M1) values, which were calculated in the shell model approach as described in [Chr97]. One should notice that for the excitation process E2 is dominating. Thus, the missing branch could be interpreted either as an evidence for a strong 2p-branch from the $\frac{3}{2}^-$ state in ^{17}Ne with a lifetime similar to the one of the γ-decay or - more likely - as an over-prediction of the B(E2) value by the shell model calculations.

2.1.1 Lifetime of the Competing γ-Decay

One way to obtain a value for the lifetime from the direct searches for the simultaneous 2p-decay of the first excited state of ^{17}Ne is to compare the measured yields for the γ-decay and the for 2p-decay, provided the same excitation mechanism is used. The γ-decay from the $\frac{3}{2}^-$ to the $\frac{1}{2}^-$ state of ^{17}Ne can proceed via M1 and E2, but the M1-deexcitation from the $\frac{3}{2}^-$ state of ^{17}Ne is dominating the γ-branch as it can be estimated from measurements of the mirror nucleus ^{17}N. From the reduced transition probabilities $B(\mathrm{M1},^{17}\mathrm{N},\frac{3}{2}^- \rightarrow \frac{1}{2}^-) = 0.23\ \mu^2$ [Til93] and $B(\mathrm{E2},^{17}\mathrm{N},\frac{3}{2}^- \rightarrow \frac{1}{2}^-) \leq 3\ \mathrm{e}^2\mathrm{fm}^4$ [Gui67] one extracts lifetime of τ_{M1}=95 fs and $\tau_{\mathrm{E2}} \geq 56$ ps, respectively. Since no experimental value of the M1 - lifetime of ^{17}Ne was available, it was calculated by Alex Brown within the shell model using the WBP and the WBT Hamiltonian by Warburton and Brown [War92]. Both are based on the same model space and are derived from different interactions. Comparisons between the predictions made with WBP and WBT will give an indication of the theoretical error in these type of calculations. [Mad01]. In addition the calculations were repeated using empirically derived effective operators to reproduce the experimental data on M1 transitions in sd-shell nuclei [Bro87]. As can be seen in Tab. 2.1 the use of the WBT interaction by Warburton and Brown [War92] and free or effective operators leads to results differing almost by a factor of two. However, this difference is rather small, when lifetimes for the simultaneous 2p-decay of ^{17}Ne in a range between picoseconds and hundreds of nanoseconds are discussed. Using the average value of the two results for the effective operators one obtains a lifetime of the $\frac{3}{2}^- \rightarrow \frac{1}{2}^-$ M1 transition in ^{17}Ne of 0.20$\pm$0.05 ps, where the error is estimated by comparison of the experimental values for ^{17}N (0.12(5) ps) [Til93] with the average of the calculated value one for ^{17}N, using the same operator.

Operator	B(M1,^{17}Ne,$\frac{1}{2}^- \rightarrow \frac{3}{2}^-$) [$\mu^2$]	τ_{M1} [ps]	B(M1,^{17}N,$\frac{1}{2}^- \rightarrow \frac{3}{2}^-$) [$\mu^2$]	τ_{M1} [ps]
WBP free	0.441	0.12	0.607	0.09
WBP eff	0.286	0.19	0.372	0.14
WBT free	0.381	0.14	0.508	0.11
WBT eff	0.256	0.21	0.312	0.17
experiment			0.46(18)	0.12(5)

Table 2.1: Comparison of the calculated B(M1) values and lifetimes for the $\frac{3}{2}^- \rightarrow \frac{1}{2}^-$ transition in ^{17}Ne and ^{17}N. The WBP and the WBT interactions are described in [War92] and the effective operators in [Bro87]. The experimental value for ^{17}N is taken from [Til93].

2.2 First Search for the Simultaneous 2p-Decay of ^{17}Ne

The missing strength of the γ-branch reported in [Chr97] motivated a direct search for the simultaneous 2p-decay of the first excited state of ^{17}Ne. This experiment was performed in 1996 at the National Superconducting Cyclotron Laboratory in East Lansing, Michigan, and the analysis is described in details in [Chr98a]. This first search for the simultaneous 2p-decay motivated the follow-up experiment which is the main part of this thesis work and will be described in this chapter in a more detailed way in order to compare the experimental techniques, the analysis steps and the results later on.

2.2.1 Setup of the First Experiment

The first search for the simultaneous 2p-decay of ^{17}Ne was performed at the National Superconducting Cyclotron Laboratory (NSCL) at Michigan State University. The exotic ^{17}Ne beam with 60 MeV/A was produced with projectile fragmentation of a 100 MeV/A ^{20}Ne beam and purified with the A1200 fragment separator in and the Wien Filter of the Reaction Product Mass Separator (RPMS) to $\simeq$ 90%. A more detailed description of the production mechanism will be given in section 3.1. As a result, an average of 5000 ^{17}Ne particles per second were scattered off a 184 mg/cm^2 ^{197}Au target with an energy of 60 MeV/u.
A compact detector stack was positioned inside a beam tube with a diameter of 15 cm as shown in Fig. 2.2 (a) and in detail in Fig. 2.2 (b). A 300 μm thick double-sided silicon strip detector (DSSD) of 40x40 strips of 1 mm width, a PIN diode (300 μm), a 5 mm thick Si(Li) detector, a 300 μm double-sided silicon strip detector of 16x16 strips of 3.25 mm width, and a CsI-array consisting of 4x4 crystals (1.7 cm $\times$ 1.7 cm $\times$ 5 cm, read out by photo diodes) were positioned in a close geometry at a distance of 16.3 cm behind the target. Thus 80% of the proton angular distribution could be observed from 0^o to 7^o (as obtained from Monte Carlo simulations of the two-proton decay) with an angular resolution of 0.35^o per strip in the first detector. The 40x40 strip detector served to reconstruct the trajectories of the reaction products, while the subsequent PIN diode (thickness 500 μm, active area 5x5 cm^2) provided the start signal for the trigger system. From both detectors an energy loss signal was derived and used for particle identification. The thickness of 5 mm of the following Si(Li) detector (diameter 5 cm) was chosen to stop the heavy ^{15}O fragments completely, while protons would loose only about 20% of their

initial energy. The 16x16 strip detector placed behind the Si(Li) allowed to reconstruct the trajectories of the protons which then were stopped in the CsI-array. Data were collected during 56 hours of beamtime at typical counting rates of $\simeq$ 25 fragment/proton coincidences per second.

2.2.2 Data Analysis of the First Experiment

The incoming ^{17}Ne particles had to be identified and separated from the 10% of contamination which primarily consisted of ^{15}O. That was done with a time-of-flight (ToF) measurement between a plastic scintillator (40 m upstream) and the Si-PIN detector of the multiple stage particle telescope.
The identification of the ^{15}O fragments from the (^{17}Ne,^{15}O+p+p) reaction was done via the ΔE-E measurement using the PIN-diode and the 5 mm thick Silicon detector which stopped the heavy reaction products. Fig. 2.3 displays the resulting ΔE-E distribution a) without application of further conditions and b) under the requirement of identified incoming ^{17}Ne projectiles. While the first plot is dominated by non-reacting projectiles (^{17}Ne and the secondary beam contamination from ^{15}O), the component from ^{15}O reaction products is clearly visible after gating on ^{17}Ne projectiles in the entrance channel (Fig. 2.3 (b)).

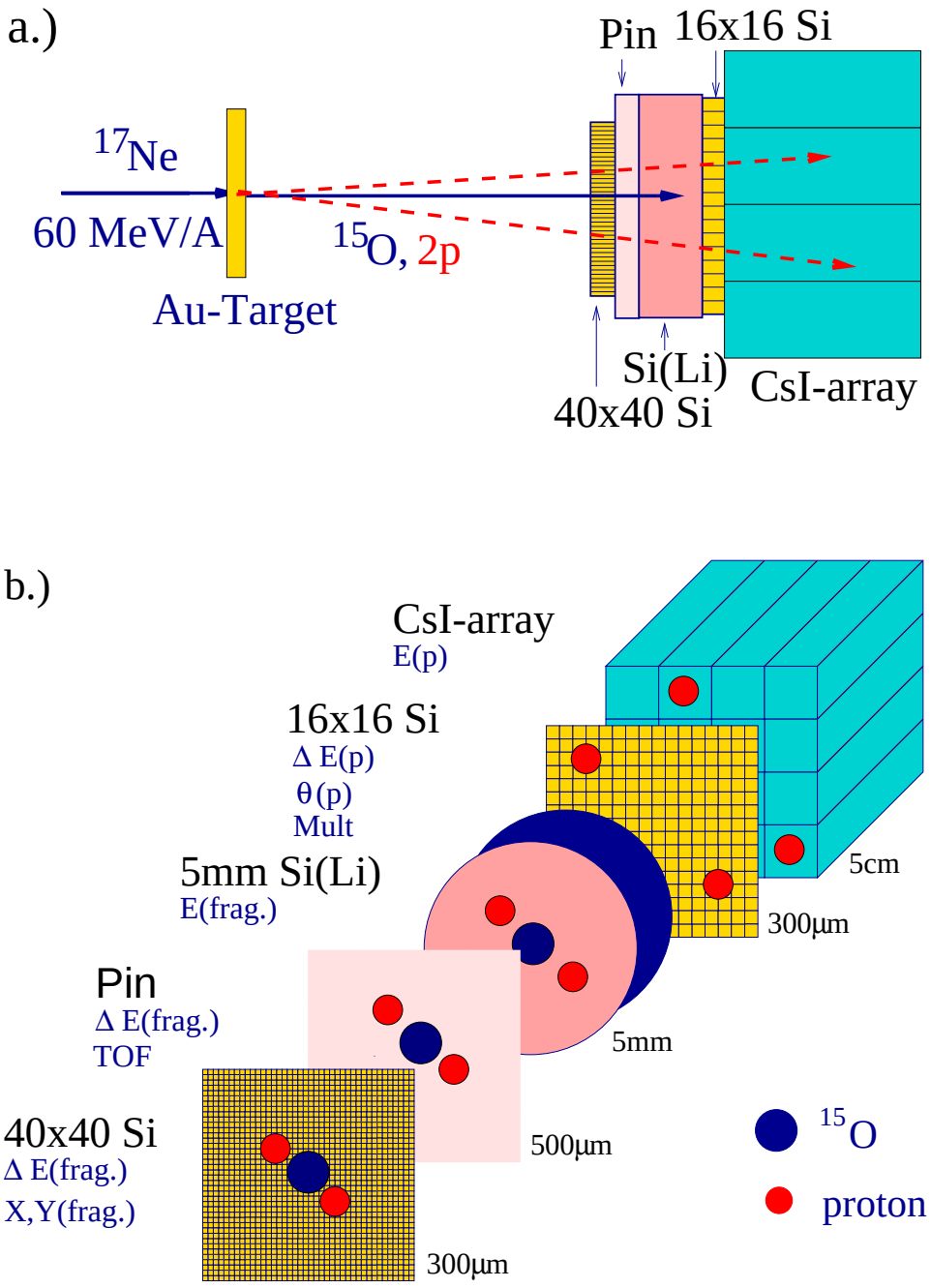

Figure 2.2: Overview of the setup for the first search for the simultaneous 2p-decay of the first excited state in ^{17}Ne. Behind the 184 mg/cm^2 thick ^{197}Au-target the stacked particle telescope for the reaction products was placed, shielded by a Heavymet-collimator. The Parallel Plate Avalanche Counters (PPAC's) placed $\simeq$ 1 m and 2 m in front of the target are not shown. Part (b) shows a schematic drawing of the stacked particle telescope at 0° for the detection of the 2p-decay. Here the ideal case is shown, where three particles are penetrating the detectors. With the first three detectors the heavy fragment is detected, with the last two the protons.

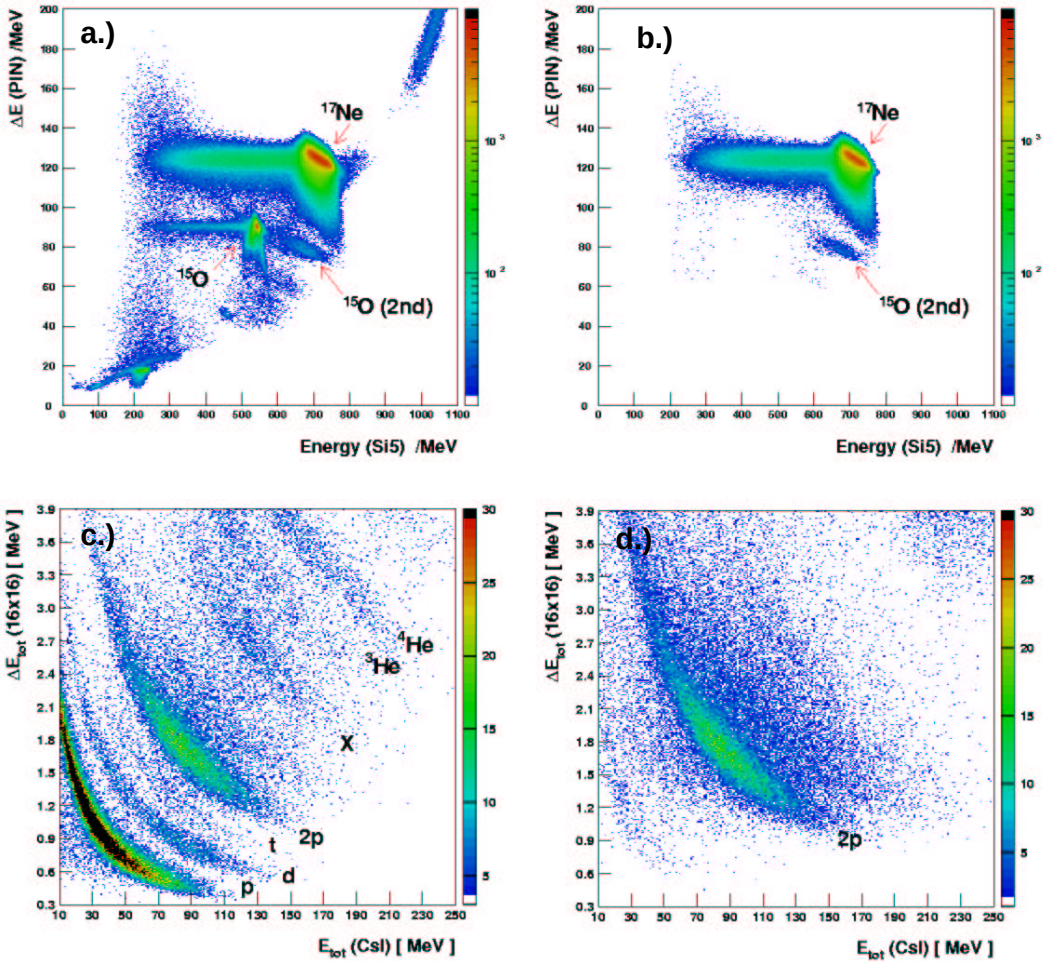

Figure 2.3: Particle identification of the heavy reaction products: The fragments were identified via a ΔE-E measurement using the PIN-diode and the thick (5 mm) Si(Li) detector. The distribution shown above was analyzed (a) with no further conditions, (b) under the condition of identified incoming ^{17}Ne projectiles. In (b) one can clearly identify the outgoing ^{15}O. Panel (c) and (d) demonstrate the particle identification of the light reaction products: The summed energy loss signal in the second silicon strip detector is plotted against the energy sum in the CsI detector array, gated on incoming ^{17}Ne. Panel (c) shows the distribution without further conditions, while panel (d) selects two-particle hits in the strip detector. Only the 2p-band associated with hits of two protons remains.

After identifying the heavy reaction product ^{15}O, events with two protons in the exit channel had to be selected. In Fig. 2.3 (c,d) the sum of the energy loss ΔE_{tot} in all of the strips of the 16x16 strip detector is plotted against the sum of the deposited energy (E_{tot}) in all CsI detectors. In a spectrum gated on incoming ^{17}Ne, the proton-, deuteron- and, barely, the triton-band are visible (left panel). An intensive band, consisting of events with twice the ΔE_{tot} and E_{tot} values of the proton band can be identified with two-proton events. At even larger energy losses the ^{3}He- and ^{4}He-bands (the band labeled with 'X' corresponds to events with 3 and more particle hits) can be seen. An additional condition requiring only double-hit events in the strip detector verifies the identification of the two-proton band (right panel).
Using the geometric correlation between events in the 16×16 strip detector and the CsI-array, it is then possible to extract the energies and directions for each proton. Together with the information on the energies of the reaction products and their trajectories, the transformation into the center-of-mass system can be performed in order to obtain the invariant mass spectrum. From the measurement of the target interaction point and the trajectory of the projectile, a gate on small deflection angles was applied to ensure Coulomb excitation as the dominant excitation process. The final decay energy spectrum is shown in Fig. 2.4.

At the time of this experiment the results were interpreted in the way as described in this section and in more detail in [Chr98b, Chr99]. The Monte Carlo simulation code PBREAK [Chr00] was extended and improved in order to simulate the full response of the detectors. Evidence for three peaks could be found in the decay energy spectrum shown in Fig. 2.4. The two peaks labelled (2) and (3) were interpreted as decays from the higher-lying states in ^{17}Ne. The measured decay energies of $920\pm40^{\mathrm{stat}}\pm50^{\mathrm{syst}}$ keV and $1620\pm80^{\mathrm{stat}}\pm80^{\mathrm{syst}}$ keV would lead to excitation energies of $1864\pm40^{\mathrm{stat}}\pm50^{\mathrm{syst}}$ keV and $2564\pm80^{\mathrm{stat}}\pm80^{\mathrm{syst}}$ keV which are in reasonable agreement with the energy of the $\frac{5}{2}^{-}$, $\frac{1}{2}^{+}$ doublet at 1764±12 keV/1908±15 keV and of the $\frac{5}{2}^{+}$ state at 2651±12 keV, respectively [Gui98]. The arrows at higher decay energies indicate that transitions in this region could be observed as well, but could not be resolved with sufficient statistics and resolution.
The peak at a decay energy of $340\pm40^{\mathrm{stat}}\pm50^{\mathrm{syst}}$ keV (1) was interpreted as first evidence for the observation of a simultaneous 2p-decay from the first excited state in ^{17}Ne to the ground state in ^{15}O with an excitation energy measured at $1284\pm40^{\mathrm{stat}}\pm50^{\mathrm{syst}}$ keV. This would agree within the uncertainties with the previously measured value for the energy of the first excited state in ^{17}Ne (1275±22 keV [Chr97] and 1288±8 keV [Gui98]).

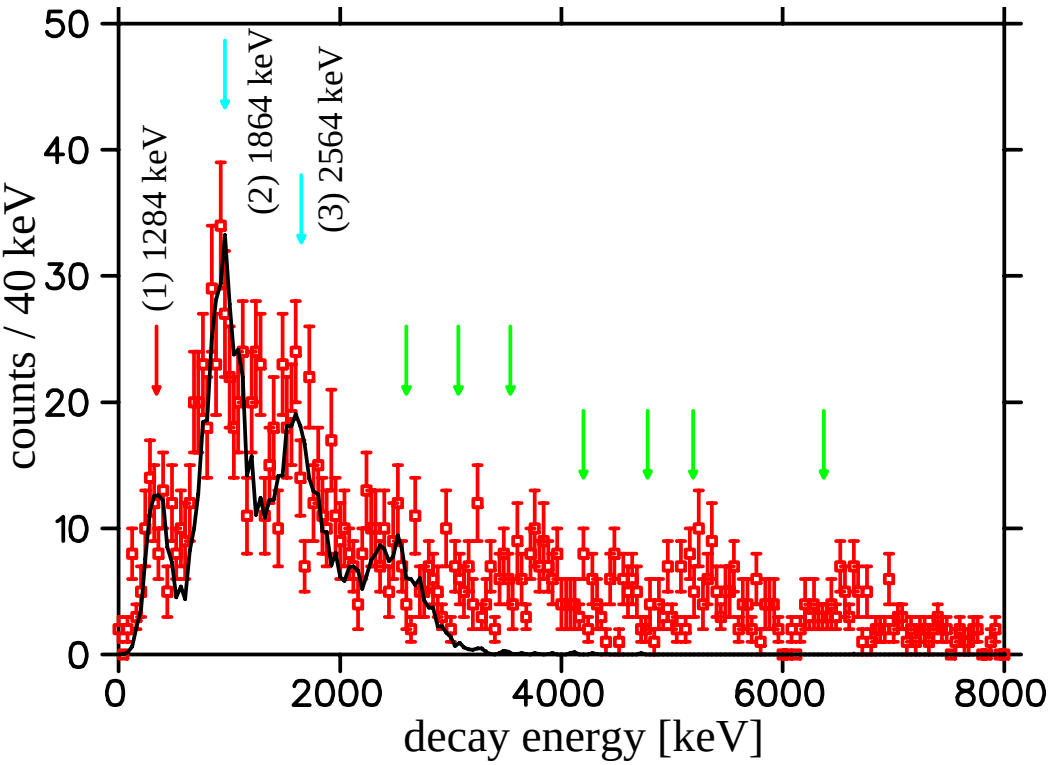

Figure 2.4: Reconstructed decay energy spectrum relative to the mass of ^{15}O and two protons. The data points represent the measured decay energy spectrum, while the solid line refers to the the simulated spectrum. The arrows indicate energy positions, where 2p transitions from known states in ^{17}Ne would be expected.

Hence, Monte Carlo simulations using the PBREAK code were performed in order to further investigate this experimental evidence. The simulation is represented by the solid line in Fig. 2.4. The simulation includes the transitions from states at 1288 keV, 1764 keV and 2651 keV [Gui98] and contains the the geometry of the setup, the experimental determined energy and position resolutions and the conditions applied in the analysis . Taking into account the conservation of energy and momentum, the decay energy is distributed to the decay products for a 3-body breakup or sequential decays of the first excited state and higher-lying states, respectively. The simulation agrees well with the measured peak positions, and the width of the peaks is reproduced. At an energy of $\simeq$ 340 keV no contribution from higher-lying states can be found.

2.2.3 Conclusions from the First Experiment

From the number of counts observed in the peak around 344 keV together with the simulated efficiencies of the setup the cross section for the 2p-decay was extracted to be $\sigma_{2p} = 0.82 \pm 0.13$ mbarn. This cross section could directly be compared to the observed cross section for the γ-decay of the first excited state in ^{17}Ne, obtained in a previous experiment using the same excitation mechanism [Chr97]. Using the value obtained here of $\sigma_\gamma = 12.0^{+5.3}_{-3.9}$ mbarn, a branching ratio of $\Gamma_{2p}/\Gamma_\gamma = 0.068^{+0.025}_{-0.032}$ was extracted. Thus the 2p-decay would proceed by a factor of $14.7^{+6.9}_{-5.4}$ slower than the γ-decay back to the ground state in ^{17}Ne.

However, the statistics obtained was quite limited and the energy resolution still needed to be improved. This experiment also left a rather unclear picture of the excitation processes. The main state expected to be populated were the $\frac{3}{2}^-$ and the $\frac{5}{2}^-$ levels via E2 excitation as shown in [Chr97]. In view of that, the measured decay energy of $920 \pm 40^{\mathrm{stat}} \pm 50^{\mathrm{syst}}$ keV for the dominating structure in the decay energy spectrum lies above the expected value. However, the most puzzling question remaining from this first experiment refers to the lifetime of the simultaneous 2p-decay, as it will be discussed in the following section.

2.2.4 Extracted Lifetimes from the Experiment

From the missing intensity of the γ branch described in section 2.1 it could be concluded that the simultaneous 2p-decay potentially proceeds as fast as the γ-decay with a lifetime in the order of of $\tau_\gamma \simeq 0.2$ ps. However, this conclusion discussed in [Chr97] was mainly dependent on the shell model prediction for the B(E2) value. The lifetime extracted in the first search for the simultaneous 2p-decay (see section 2.2.3), already indicated that the measured 2p-decay yield would not account for the missing excitation cross section. Although secondary excitations to higher-lying excited states could account for a fraction of the missing strength, it seemed most likely that the B(E2) value was over-predicted by the shell model calculations. Using the virtual photon formalism as in section 2.1 a value of B(E2)=71.5^{+30}_{-22} e^{2}fm^4 could be deduced from the observed cross section of $\sigma_{\mathrm{exc}} = \sigma_\gamma + \sigma_{2p} = 12.8^{+5.3}_{-3.9}$ mbarn.

Concluding from the results of the first search for the simultaneous 2p-decay of ^{17}Ne that the simultaneous 2p-decay of the first excited state would proceed by a factor of $14.7^{+6.9}_{-5.4}$ slower than the γ-decay back to the ground state in ^{17}Ne and predicting a lifetime of the order of 0.2 ps for the γ-decay back to

the ground state, as shown in section 2.1.1, a lifetime for the simultaneous 2p-decay of $2.9^{+1.6}_{-1.3}$ ps could be extracted.

2.3 Comparison of the Lifetime Models with the First Experiment

The 2p-lifetime of $2.9^{+1.6}_{-1.3}$ ps obtained in section 2.2.4 is hard to explain using any of the theoretical models, as can be seen from Tab. 2.2. Only the assumption of a relative angular momentum between the diproton and the ^{15}O of $L = 0$ and relative angular momentum of the protons of $(l = 2)$ would give the right order of magnitude for the lifetime.

Method	Lifetime	Section
Experiment	$2.9^{+1.6}_{-1.3}$ ps	2.2.4
Three Body Breakup	470(100) ns	1.3.3
Diproton $L = 2, l = 0$	411 ps	1.3.1
Diproton $L = 0, l = 2$	16 ps	1.3.1
Uncorrelated d^2	1.4 μs	1.3.2
Uncorrelated (sd)	1.8 ns	1.3.2

Table 2.2: Comparison of the experimental and theoretical lifetimes for the simultaneous 2p-decay of the $\frac{3}{2}^-$ state in ^{17}Ne for various alternative decay scenarios. The spectroscopic factors were set to unity for all models according to section 1.3.1.

Chapter 3

Experimental Setup and Procedure

The only non-questionable conclusion to be drawn from the first search for the simultaneous 2p-decay of ^{17}Ne was that a new experiment had to be performed. This experiment is the main part of this thesis and the experimental techniques, the analysis and the results will be discussed in detail in the following chapters. The goal of the new experiment was the unambiguous confirmation or non-confirmation of the evidence of simultaneous 2p-decay of ^{17}Ne with a lifetime of $2.9^{+1.6}_{-1.3}$ ps. In addition the excitation and deexcitation processes of the low-lying states in ^{17}Ne should be investigated. This chapter describes the production and purification of the exotic ^{17}Ne beam at the radioactive beam facility of the National Superconducting Cyclotron Laboratory at Michigan State University in East Lansing and the experimental setup. The experimental setup was especially optimized for the detection of the potential 2p-decays of the low-lying states in ^{17}Ne. Compared to the setup of the first experiment, the detection efficiency was increased, segmented detectors allowed for higher beam currents and redundant particle tracking capabilities allowed for an improved separation of reactions in the target from breakup reactions in the detectors.

3.1 Production of the ^{17}Ne Beam

There are two main methods for the production of radioactive nuclear beams. One is known as Isotope Separation On-Line (ISOL) and the other one as

projectile fragmentation. In the ISOL approach typically a high-energy proton beam is stopped in a production target (e.g. UC_x, ThC_x). There the fragmentation occurs and the resulting fragments diffuse out of the target, are transported to an ion source and then post-accelerated. The production mechanism has to be developed individually for each element and involves detailed knowledge about the chemical properties of the elements to be extracted in order to optimize the diffusion and ionisation processes. However, the limiting factor in this production method is the lifetime of the exotic nuclei. Nuclei with lifetimes shorter than the time needed for their extraction are not accessible. On the other hand, this production method offers the unique opportunity to accumulate the ions in a trap, convert them into highly charged ions e.g. in a EBIS ion source and then accelerate a high quality ion beam with a very low emittance after applying cooling techniques. This specific technique will be used at the **R**adioactive Beam **EX**periment at ISOLDE/CERN (REX-ISOLDE) [Hab97], which will become operational in 2001.

The other method, the projectile fragmentation, employed at MSU/USA, RIKEN in Japan, GANIL in France and GSI in Germany makes use of fast stable ion beams which are then impinched on a low-Z target in order to fragment the projectile. At the National Superconducting Cyclotron Laboratory at MSU the projectile is accelerated in the K1200 cyclotron to energies of typically 50-100 MeV/A (in our case the projectile was ^{20}Ne with 100MeV/A and $\beta = 0.4295$). Due to the high velocity of the projectile and the relatively small energy loss in the target (in our case we used a ^{9}Be target, 790 mg/cm^2 thick), the fragments still carry relativistic energies and are strongly forward focussed. In such a fragmentation reaction a whole variety of nuclei is produced. Thus, it is important not only to separate the fragments from the primary beam but also to isolate the isotope of interest. This is achieved by using the magnetic A1200 fragment separator.

3.1.1 The A1200 Fragment Separator

The A1200 fragment separator [She92] at the NSCL is depicted in Fig. 3.1. The A1200 has an achromatic ion-optical design with two dispersive images in between the two pairs of dipoles that bend the beam. Via the magnetic field of the dipoles the desired ratio of momentum to charge can be selected, as it is shown in Eq. (3.1).

$$B\rho = \frac{p}{Q}, \tag{3.1}$$

with the magnetic field B, the radius of the dipole ρ, the momentum of the fragment p and the charge state Q. Additionally Fig. 3.1 shows the quadrupole

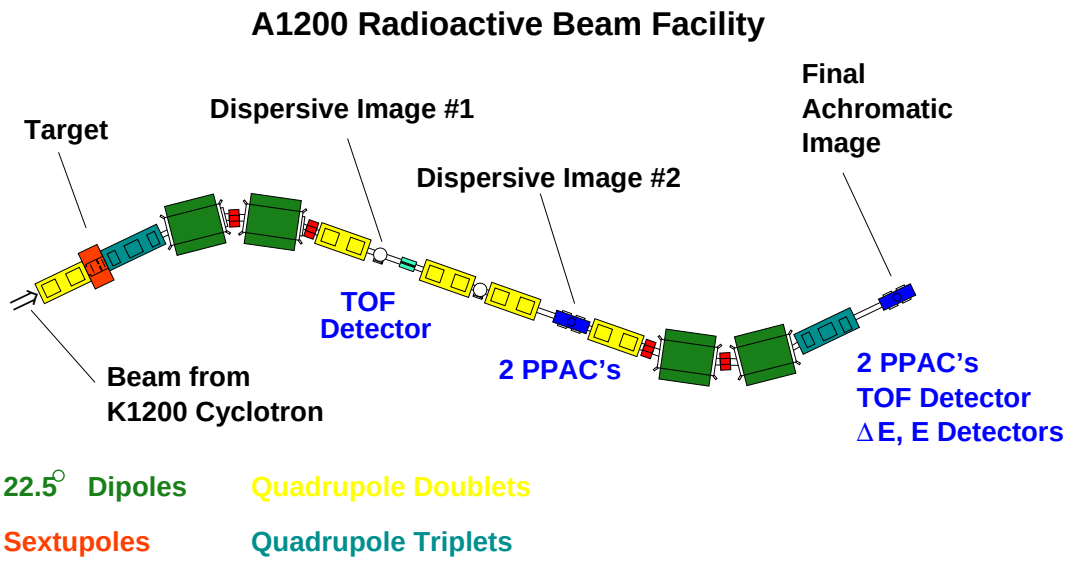

Figure 3.1: Schematical view of the A1200 fragment separator at the NSCL. The ion optical elements are displayed together with the detector equipment available to analyze the produced secondary beam.

magnets which serve to focus the beam. For further purification it is possible to implement a wedge shaped degrader at the second dispersive image. Nuclei with an equal initial rigidity experience an energy loss which proportional to the square of their charge, resulting in a different magnetic rigidity after the degrader. Finally the value of the Bρ for the second pair of dipoles has to be optimized for the optimum yield of the desired fragment.

At the focal plane of the A1200 two position sensitive parallel plate avalanche detectors (PPAC's) for position measurements followed by a ΔE-E particle telescope consisting of a PIN diode and a thick plastic scintillator can be used for particle identification. In addition to that, the signal of the PIN diode can be used for time of flight measurements with respect to a thin scintillator 20 m further upstream. In order to identify the desired fragments and to check the position of the secondary beam these detectors can be moved into the beam axis. According to the position measurement slits at the focal plane can be adjusted in order to realize an optimum of beam purity and beam current. After proper particle identification and beam alignment the detectors are retracted and the beam is sent to the experimental vault.

The production of the radioactive ^{17}Ne beam as it was used for this experiment is described in detail in [Chr98a], where also examples for the measured spectra in the A1200 detectors are given. For the present experiment the same settings were used: As can be seen in Tab. 3.1 the initial purity of the ^{17}Ne beam

Setting	Value
Primary beam	^{20}Ne at 100 MeV/A
Target	790 mg/cm^2 ^{9}Be
$B\rho$ of 1^{st} pair of dipoles	2.0853 Tm
Degrader	233 mg/cm^2 Al
$B\rho$ of 2^{nd} pair of dipoles	1.9095 Tm
Momentum acceptance	$\pm$1.5%
Extracted secondary beam	^{17}Ne at 58.92 MeV/A
Purity of the ^{17}Ne beam	$\simeq$ 7.5%
Strongest contaminant (^{15}O)	$\simeq$ 85%

Table 3.1: Settings of the A1200 fragment separator for the production of the ^{17}Ne beam.

was rather poor with ^{15}O as the dominant contamination. With ^{15}O at the same time being the reaction product of a potential 2p-decay of ^{17}Ne, further precautions had to be taken in order to purify the secondary beam. Thus, we used the Wien Filter of the **R**eaction **P**roduct **M**ass **S**eparator (RPMS) at the NSCL located in between the A1200 and the experimental setup.

3.1.2 The Reaction Product Mass Separator

The RPMS, initially designed as a stand-alone-tool for the direct separation of nuclei produced in projectile fragmentation [Har81], can be used in combination with the A1200 to further separate secondary ion beams. The RPMS has a solid angle of 1 msr and is useful over a broad dynamic range of ion energies (in principle up to 125 MeV per nucleon for m/q of 2, with a mass dispersion decreasing with the ion velocity).

There are two types of dispersive elements used in the RPMS: (1) a Wien filter (crossed $\vec{E}$ and $\vec{B}$ fields) acting as a velocity filter and (2) a magnetic dipole that introduces a momentum dispersion. Fig. 3.2 shows a schematic sketch of the RPMS. The beam first passes through a quadrupole doublet, before entering the Wien filter which is followed by a dipole and another quadrupole doublet. The vertical deflection angle of the dipole varies with the magnetic rigidity of the respective secondary ion species. Hence, the beam line behind the dipole is designed to be mechanically movable in the vertical direction.

Particles with velocities differing from the species of interest will be bent away

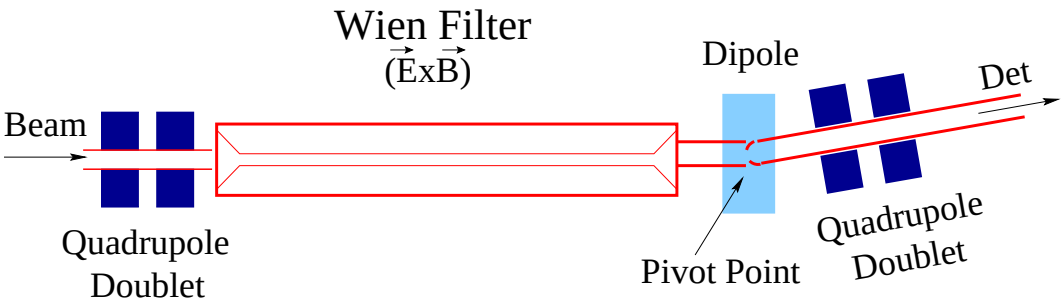

Figure 3.2: Schematic sketch of the **R**eaction **P**roducts **M**ass **S**eparator which was used to further purify the beam. The two dispersive elements are the Wien filter and a magnetic dipole.

and will hit the walls of the Wien filter. Still surviving beam contaminants will be transported through the RPMS with a spatial offset with respect to the desired fragments. These remaining contaminants can be eliminated using the dipole magnet behind the Wien filter. Nuclei with the same velocity now entering the dipole magnet at different positions will be further separated. The deflection angle is chosen to optimize the contaminant separation achieved by an adjustable slit, while at the same time achieving a beam focus at the secondary target. Finally the tail of the RPMS, including the whole detector setup, is lifted by the amount of the deflection angle in order to send the desired particles centered onto the target. In our case the tail of the RPMS had to be lifted by an angle of 3.05° degrees.

3.2 Experimental Setup

In order to identify the 2p-emission from the excited states in ^{17}Ne a complete kinematical reconstruction of the reaction process on an event-by-event basis has to be performed. The setup was optimized in order to look for 2p-decays from the $\frac{3}{2}^-$ state in ^{17}Ne. Due to the small decay energy available (only 344 keV), the protons were emitted under very small relative opening angles in the laboratory frame, as discussed in [Chr98a]. A stacked particle telescope was chosen as the optimum detector setup, allowing to be penetrated simultaneously by all reaction products while still being able to detect all of them individually.

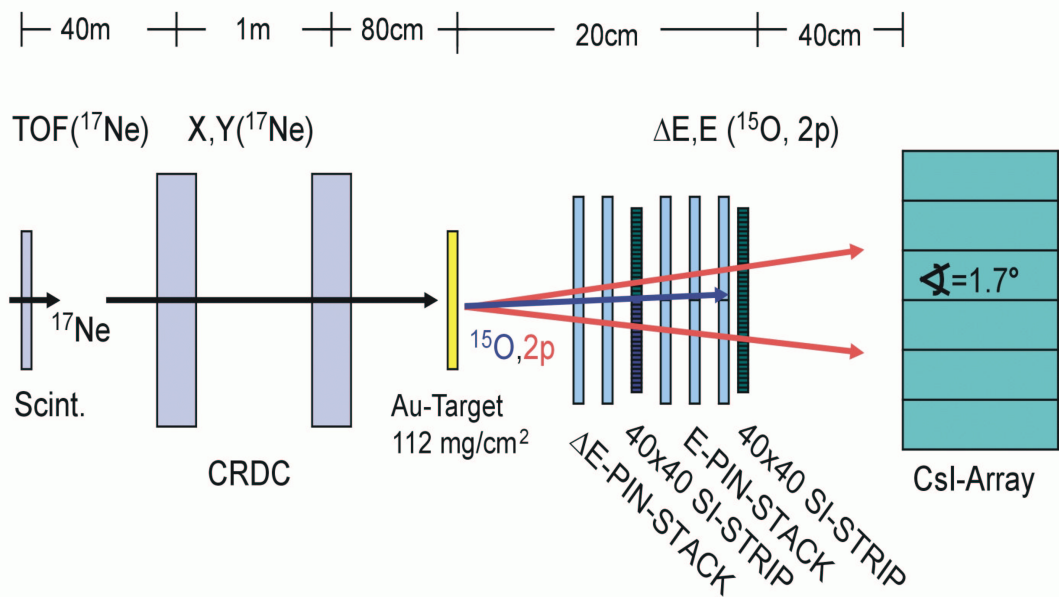

Figure 3.3: Sketch of the setup for the main experiment designed for the detection of a potential 2p-decay in ^{17}Ne. The ^{17}Ne is identified via time-of-flight measurements and tracked in the CRDC's (Cathode Readout Drift Chambers). The reaction products following the 2p-decay were detected in a multiple stage particle telescope.

3.2.1 Projectile Identification

For the identification of the ^{17}Ne projectiles via time-of-flight measurements a thin plastic scintillator was used for the start signal. The scintillator was placed $\simeq$ 40 m upstream relative to the target, while the stop signal was derived from the first detector of the particle telescope. Additionally the Cyclotron RF was used as a redundant start signal for the time-of-flight measurement.

3.2.2 Projectile Tracking: the CRDC's

The tracking of the incoming particles was essential in order to be able to determine the Coulomb deflection angle and the interaction point on the target. The accuracy of the latter has large impact on the resolution of the center-of-mass 2p-decay energy spectrum. With the beam intensities expected, the use of parallel plate avalanche counters (PPAC's, [Swa94]) as applied in the first experiment (see Fig. 2.2 (a)) would not have given sufficient position resolution, as can be seen in [Chr98a]. As already discussed before, the ^{17}Ne

beam and the ^{15}O contaminant were spatially separated at the exit of the RPMS, where ^{15}O was eliminated by an adjustable slit between the positions for the two tracking detectors. Therefore the first tracking detector registered a twelve times higher counting rate compared to the other one. Thus, it was necessary to use tracking detectors able to stand higher counting rates, while at the same time aiming at a better position resolution than PPAC's. In order to achieve this, **C**athode **R**eadout **D**rift **C**ounters (CRDC's) were used. These detectors were built as prototypes for the focal plane detectors of the S800 high resolution magnet spectrometer at the NSCL [Yur99].
The CRDC's have an active area of 10.16 cm × 15.24 cm and an overall size of 16.51 cm × 26.04 cm. The principle of these counters is a single wire drift detector, except that the position along the wire is obtained by pad readout of the induced charge on the cathode. In the CRDC the pads have a pitch width of 2.54 mm. The wire runs parallel with the longer side of the detector and thus a drifttime measurement is equivalent to a position measurement along the short side.
The position resolution of the CRDC's is expected to be in the sub-millimeter range. The CRDC's were filled with 13 torr Isobutane. Their orientation in the beamline allowed to determine the horizontal position with the drifttime, while the cathode pads allowed to measure the vertical position.

3.2.3 The Multi Stage Particle Telescope

In order to detect the reaction products, ^{15}O plus the two protons, all emitted under small forward angles in the laboratory frame, a multi stage particle telescope was built. Fig. 3.4 shows a sketch of the detector stack including the observables measured in the different detectors. The particles first hit two adjacent quadrant PIN diodes (5 cm × 5 cm surface area, PIN1: 480 μm and PIN2: 476 μm thick), which served as energy loss detectors. Behind them a 40 × 40 double sided strip detector (DSSD) was placed, with a total surface area of 4 cm × 4 cm, a strip width of 1 mm and a thickness of 973 μm. The task of this detector was to determine the trajectory of the emitted ^{15}O. It was followed by another stack of quadrant PIN diodes (PIN3-5: 5 cm × 5 cm surface area, 484 μm, 478 μm and 1009 μm thickness). The total thickness of those detectors was large enough to stop the ^{15}O fragments produced in the reaction of the ^{17}Ne beam with 58.9 MeV/A ($\Delta p/p = 3\%$) in the 112 mg/cm^2 thick ^{197}Au target. The protons originating from the same reaction penetrate those detectors and then hit a second 40 × 40 DSSD with a thickness of 985 μm. In this detector the position of the two protons and an energy loss signal were detected. Finally, the protons were stopped in a CsI-array consisting of 6x6 CsI

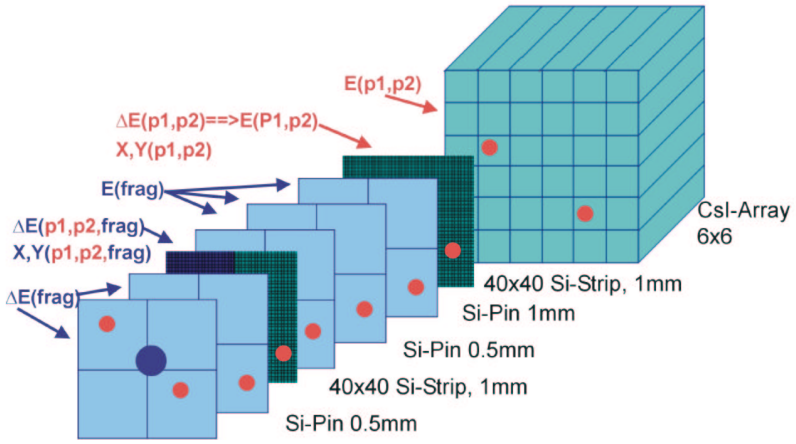

Figure 3.4: Sketch of the multi stage particle telescope; shown is the case, where the ^{17}Ne breaks up in the target and the fragments are detected in the telescope. The protons penetrate the segmented PIN diodes and are measured in the two DSSD's and in the CsI-array, while the ^{15}O fragments are stopped in the last PIN diode.

crystals, each read out by a photodiode (Type: Hamamatsu S3590-01). The crystal size was 1.7 cm $\times$ 1.7 cm $\times$ 5 cm. The crystals were wrapped with a reflective paper (blotting material HATF10710 from Millipore Inc.) and the photodiodes were glued to the crystals with an optical glue (EPO-TEK 301-2). The first DSSD, mainly dedicated to detect the ^{15}O fragments, was instrumented to deliver additional energy loss signals for the protons. For that purpose the energy signal after the preamplifier was split and processed with two different gain settings, a low gain for the ^{15}O fragments and a high gain for the protons. Table 3.2 shows the positions of the detectors along the beam axis (target at 0), their total angular coverage and their angular granularity in the laboratory frame. The position of the protons can be measured at three positions: in the two DSSD's and with a somewhat reduced precision in the CsI-array. Thus, this setup opens up the possibility for an alternative method to determine the interaction point in the target, not only by measuring the projectile trajectory with the CRDC-detectors, but also via "backtracking" with the protons making use of their position information obtained from two of the detectors (DSSD1, DSSD2 and CsI) and track its way back to the target. Applying this method to each of the protons further increases the precision of the position measurement. In addition to that, the setup was designed to offer two more features: Rutherford scattering of the protons in the target and in the detectors is a limiting effect on the angular resolution. For 55 MeV protons passing the three PIN diodes used for the energy measurement of the ^{15}O fragment (PIN3-5) the average straggling angle is $\simeq 1°$. Hence, it can happen that due to the angular scattering in the detectors a proton gets deflected into

different pixels of the DSSD's or different crystals of the CsI-array. With the measurement of the interaction point on the target and the proton trajectory at three different positions, this setup allows to identify events where one or two of the protons were scattered under large angles in the Silicon detectors, because their positions measured in the subsequent detectors would not fall anymore onto a straight line. As a second new feature it was possible with this setup to determine the position of the breakup of the ^{17}Ne projectiles along the beam axis by calculating the crossing point of the two proton trajectories. That way it was possible to distinguish reactions occurring in the target from breakup reactions in the detector material.

Detector	Z-Position [m]	Total angular coverage	Angular resolution of a single pixel/segment
PIN1	0.090	15.5°	-
PIN2	0.096	14.6°	-
DSSD1	0.125	9.1°	0.46°
PIN3	0.147	9.7°	-
PIN4	0.151	9.4°	-
PIN5	0.164	8.7°	-
DSSD2	0.188	6.1°	0.30°
CsI-array	0.534	5.7°	1.8°

Table 3.2: Detector position along the beam axis with respect to the target for the detectors of the multi-stage particle telescope and their total angular coverage. For the DSSD's and the CsI-array also the angular resolution for individual pixels/segments is given.

3.3 Electronics

The experiment required a significant electronic setup. The use of two DSSD's with 80 channels each, with one of them operated in a split mode with two gain settings, required alone 240 electronic channels which had to be equipped with amplifiers and ADC's. On the other hand, the most important trigger condition was rather simple, i.e. a coincidence of a heavy fragment detected in PIN1 and a light particle in the CsI-array. Due to the low coincidence rate it was feasible to read out every channel for every coincidence event without risking large losses in the data acquisition system due to computer dead time. Fig. 3.5 shows a schematic sketch of the electronics setup, which is described in detail below. The "master trigger" (MG) was defined as a coincidence

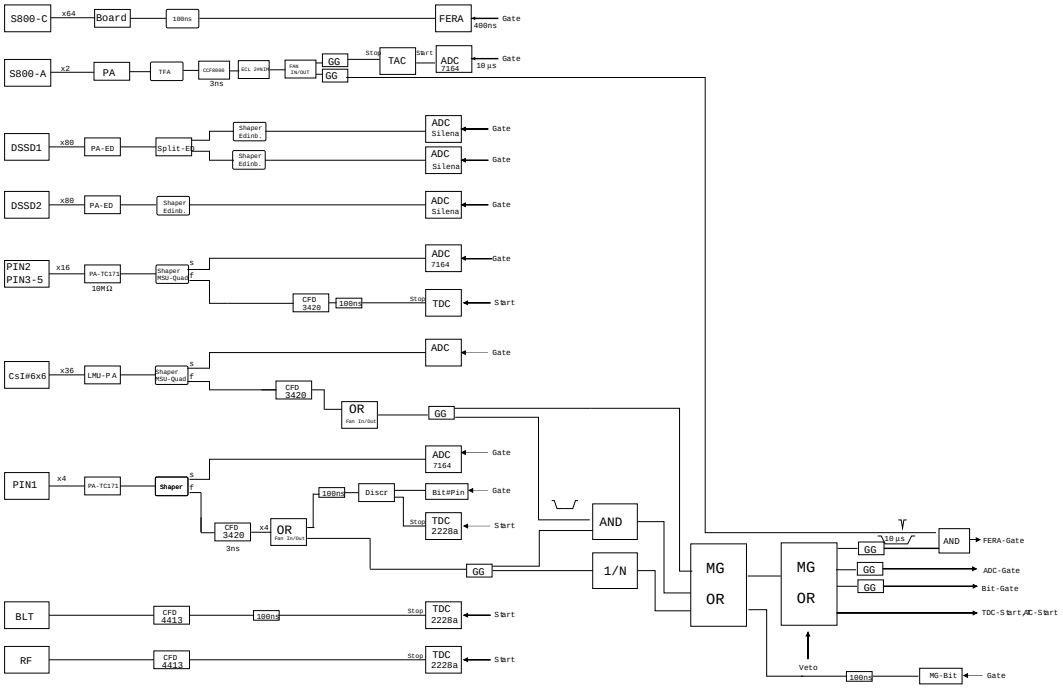

Figure 3.5: Schematic of the electronics setup. PA=preamplifier, Shaper=main amplifier, GG= gate generator, MG=master gate, BLT=timing scintillator, RF=radio frequency of the cyclotron, 1/N=downscaler, CFD=constant fraction discriminator.

between a heavy fragment registered in one of the quadrants of the first PIN diode and at least one light particle detected in a CsI crystal. Additionally single events of the mainly non-reacting ^{17}Ne particles registered in the first PIN diode (PIN1) were recorded with a downscale factor of 300, allowing the determination of the total number of incident beam particles. These events furthermore served as a continuous monitor signal to check the stability of the gain settings and to monitor changes in the tune of the beam.

The 20 channels of the five segmented PIN diodes and the 36 channels of the CsI-array were instrumented in a similar way. The detector signals were sent to preamplifiers built at the MSU and in Munich, respectively, and placed outside the vacuum chamber. The signals were then shaped and amplified in the MSU Quad Shaper modules, which provide a slow and a fast output signal. The signal of the slow output was converted by Phillips ADC's and read out via a VME based data acquisition system. The fast signal was discriminated and then further used for timing and logic purposes.

The master trigger was generated either by a coincidence between an OR of the four segments of the first PIN diode (PIN1) and an OR of all the 36 CsI crystals or by a down-scaled event in PIN1. For the calibration of the detectors for the heavy fragment and the protons the master trigger was derived from a single event in PIN1 or the CsI-array, respectively. From the master trigger all necessary gates were derived as well as the start signals for the TDC's and the TAC's.

The 240 channels from the DSSD's were fully instrumented by the Edinburgh group with home-built electronics. The signal of the first strip detector was split behind the preamplifier (Edinburgh/RAL Preamplifier RAL108) and then amplified in two gain settings (400 MeV, 20 MeV) with the Edinburgh/RAL Shaping Amplifier (RAL 109). The second DSSD was amplified only in the 20 MeV gain setting. The signals were all digitized by Silena 4418/V ADC's.

The signals of the timing scintillator (BLT) and the radio frequency (RF) were discriminated an then fed as stop signals into the (Le Croy-) TDC's which received their start signal from the "master live" trigger. In addition timing signals from the PIN-OR and the individual signals of the segments of the first PIN diode (PIN1) were recorded in a TDC.

The electronics for the CRDC's was somewhat more complicated. The anode signals were preamplified and then passed through a timing filter amplifier (TFA) before the discrimination by a sufficiently high threshold. This signal was then used as stop for a TAC feeding into a Phillips ADC. The start for

the TAC was provided by a "master live" signal. From each cathode pad a signal was read out individually. Since the detector resembles to a slice of a time projection chamber, electronics already developed for TPC's was used. Mounted inside the vacuum chamber preamplifiers and shapers of front end electronics (FEE) cards were used, which were developed for the STAR collaboration [Sta92]. The signals were then digitized by FERA QDC's that obtained their gate, from a coincidence of the "master live" signal and the anode signal of the specific CRDC.

Several bit gates were generated to identify the individual trigger types and fed into a bit register. Scaler modules were used for an online monitoring of all relevant counting rates.

3.4 Comparison of the Setups

Before elaborating on the details of the present experiment a concluding comparison with the experimental setup used in the first experiment (see section 2.2) is intended to emphasize the optimization process. The setup for the present experiment was optimized by performing similar Monte Carlo simulations as described later in the analysis procedure. The two initial goals were to collect more statistics for the decays from the $\frac{3}{2}^-$ and the $\frac{5}{2}^-$ state in ^{17}Ne and to improve the energy resolution.

- **Use of the full available beam current** (up to 20.000 ^{17}Ne/s): The rate limitation to about 5×10^3 pps during the first experiment was overcome in the new setup by using four-fold segmented PIN diodes, allowing to process the full available secondary beam intensity of about 2×10^4 ^{17}Ne/s.

- **Avoiding double proton hits in one detector segment:** In the previous experiment the largest efficiency losses were due to insufficient detector granularity, i.e. whenever two protons hit the same detector segment, it was impossible to assign the individual energies and trajectories. The use of a 40×40 DSSD instead of a 16×16 DSSD and the upgrade of the CsI-array helped to minimize those effects.

- **Higher resolution in the decay energy spectrum:** The accuracy of the particle tracking dominates the resolution of the decay energy spectrum. The use of the CRDC's, the higher granularity of the proton

tracking detectors and the use of a thinner target helped to improve the decay energy resolution significantly.

- **Redundancy:** As mentioned in section 3.2.3 the use of the two DSSD's offers a number of possibilities for backward tracking. This redundancy increases not only the reliability of the tracking measurements but also its accuracy.

3.5 Experimental Procedure

This section describes the different steps required to run the experiment.

3.5.1 Alignment of the Setup

The alignment of the tail of the RPMS which had to be raised during runtime to an angle of $\simeq 3^\circ$ had to be performed when the tail was still in the horizontal position. The relative positions of the detectors with respect to each other can only be measured before raising the tail. The tail consists of 7 m long I-beams, which are carrying at their end the weight of the vacuum chamber (32 inch diameter, $\geq$ 200 kg). A small counterweight at the RPMS should prevent the I-beam from bending, however, it is mounted only 1 m behind the pivot point. Consequently the overall precision of the alignment was limited due to the bending effects once the detector setup was lifted. However, the relative distances of the multi-stage particle telescope including the target were fixed and unaffected by the lifting procedure, while a central alignment with respect to the CRDC's at runtime could not be guaranteed.

3.5.2 Beam Tuning

First the target had to be replaced by a viewing scintillator for beam tuning purposes. The ^{20}Ne primary beam was degraded to the same magnetic rigidity as the secondary ^{17}Ne beam, in order to assure similar ion optical properties. The ^{20}Ne beam was tuned so that the focus was on the target position. Steps in the development of the secondary ^{17}Ne beam are described in detail in [Chr98a] and the settings of the A1200 are given in Tab. 3.1. The ^{17}Ne beam was identified at the experimental setup with an additional PIN diode (300 μm), placed on a movable mount in front of the first CRDC. Finally the tail of the

RPMS was lifted to an angle of 3.05° and the adjustable slits in between the two CRDC's were optimized for the elimination of the ^{15}O beam contamination.

3.5.3 Calibration Procedure

- **Calibration of the CRDC's:** The individual response of the FEE cards and the attached QDC's were gain matched by applying a tail-pulse to the anode wire of the CRDC. The capacitive coupling of the anode wire to each pad induced a fixed charge. This was done for two pulser settings and a linear correction was applied to each pad before the signal processing. This method not only corrected for different amplifier gains, but also compensated for any non-uniformity in the cathode pad size.
  The position calibration was then performed by placing a calibration mask in front of the CRDC's. For this purpose, the slits between the CRDC's had to be opened wide and the last quadrupole doublet had to be detuned. A beam sweep was initiated to steer the beam in horizontal and vertical direction in order to achieve position calibration for the whole detector acceptance.

- **Calibration of multi stage particle telescope:** The multi stage particle telescope was calibrated as a whole including the target in front of the detectors using ^{15}O beams at several energies produced by the identical reaction used for the production of the ^{17}Ne beam. The degrader between the dipoles of the A1200 was removed providing a variety of isotopes for calibration purposes. The protons for the calibration of the proton detectors were produced in the same way, just with different magnet settings for the A1200.

- **Time Calibration:** The TDC's for the time-of-flight calibration were calibrated with a standard time calibrator and two different settings, although only relative time measurements were used for the particle identification.

- **Data acquisition:** The standard NSCL data acquisition system [Fox89], based on a VME double processor system was used. The data were stored on 8 mm Exabyte tapes. For the online analysis as well as for the first steps in the offline analysis, the program SMAUG was used [SMAUG].

3.5.4 Beam Current and Trigger Rates

The maximum beam current for ^{20}Ne at 100 MeV/A available from the cyclotron was 60 pnA, which resulted in a maximum ^{17}Ne beam intensity of 20000 part/s, which could be processed by the experimental setup. Data were collected for about 85 hours and a total of $\simeq 3.25 \times 10^7$ events were recorded. Tab. 3.3 shows the different count rates. The trigger rate was low enough preventing losses due to dead time in the data acquisition system.

Detector or bit	Average rate [1/s]
PIN1 Segment1	3620
PIN1 Segment2	3860
PIN1 Segment3	4040
PIN1 Segment4	2780
PIN2 Segment1	3130
PIN2 Segment2	2360
PIN2 Segment3	2810
PIN2 Segment4	3400
CRDC1	149000
CRDC2	12800
PIN1 OR	12200
PIN2 OR	11700
CsI OR	124
PIN1 AND CsI	91
PIN1 $\times$ 1/N	40
MASTER	131
MASTER Live	106

Table 3.3: Count and trigger rates, averaged over the whole beamtime. The "master trigger" (MASTER) rate consists of down-scaled singles in the first PIN diode (PIN1 $\times$ 1/N) and the coincidences of the first PIN diode and the CsI-array (PIN1 AND CsI) The difference between the MASTER and the "master live trigger" (MASTER Live) gives an estimation of the dead time of the data acquisition.

Chapter 4

Data Analysis

This chapter describes the analysis of the data and covers the results of the calibration, the particle identification and the tracking methods as well as the analysis conditions applied in order to generate the 2p-decay energy spectrum of ^{17}Ne.

4.1 Calibration

For the detectors of the multi-stage particle telescope the calibration was performed analogue to the first experiment [Chr98a] and according to the different steps already outlined in section 3.5.3. The complexity of the readout of the CRDC detectors required a special calibration procedure as will be described in the following paragraph.

4.1.1 Calibration of the CRDC's

The calibration of the CRDC's was performed in two steps. In the first step the signals from the CRDC's were converted into a position information within the coordinate system of the detector defining a software correction function to align the CRDC's to the central particle telescope as will be described in section 4.3.1.
This procedure corrected for misalignments introduced by the lifting of the RPMS tail as described earlier. For the position calibration of the cathode pad the signal height in each of the 32 channels was analyzed on an event by

event basis as illustrated by a typical example in Fig. 4.1 (a). The position was determined by fitting the resulting distribution with a Gaussian line shape. Taking into account the distance of 0.254 cm between the pads, the centroid of the Gaussian distribution translated into the cathode position.

For a significant percentage of the events ($\simeq$ 30% for each detector) one

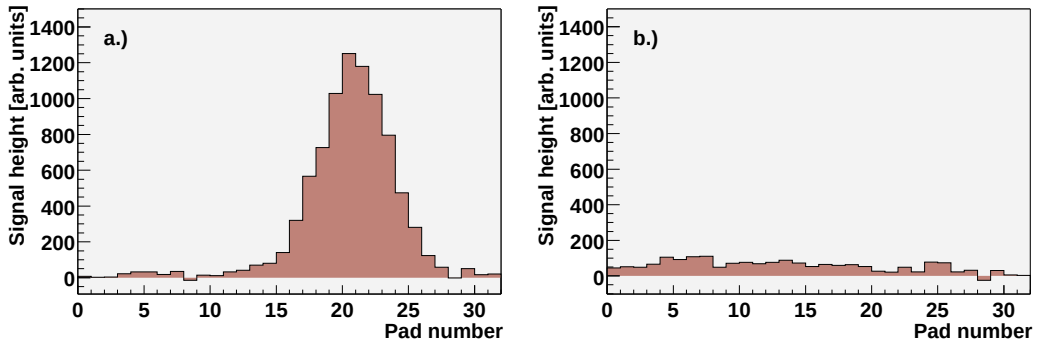

Figure 4.1: Snapshots from the Pad-Signals of the CRDC's. For a single event the height of the signal is plotted for each of the 32 pads. Each column presents one pad. Part (a) shows a good event, where it is possible to determine the centroid with a Gaussian fit, part (b) shows an event, where probably the gate for the FERA ADC's or the amplifier board was not opened in time. For such an event the position information of one coordinate in that detector is lost.

of the two CRDC's showed a pad distribution as displayed in Fig. 4.1 (b). Efficiency losses due to the lack of extractable position information for those events may be explained by the high counting rates (especially for the first CRDC) including temporary failures of the delicate CRDC electronics boards or by misalignments of the ADC gates. Some of the losses appeared for events with large drifttimes in the anode which was measuring the horizontal coordinate. Since the CRDC's were turned by 180 degree with respect to each other, a large drifttime in one CRDC corresponds to a short drifttime in the other detector. Thus at least one signal from the cathode pads was recorded which allowed to apply the drift ellipsoid method used for the particle tracking as described in section 4.3.1.

For the calibration of the anode signals a calibration mask was used. The two TAC signals which measured the anode drifttime were plotted against each other as illustrated in Fig. 4.2 (a). For the case shown here the mask was placed in front of CRDC2. However, in the other CRDC the structure of the mask still could be seen. The projection of Fig. 4.2 (a). on CRDC2 is displayed in Fig. 4.2 (b). The 2.5 mm grid structure of the calibration mask can be identified in the peaks of the TAC signal. Fig. 4.3 shows the centroids of the TAC-peaks plotted against the position of the mask holes, resulting in a linear correlation.

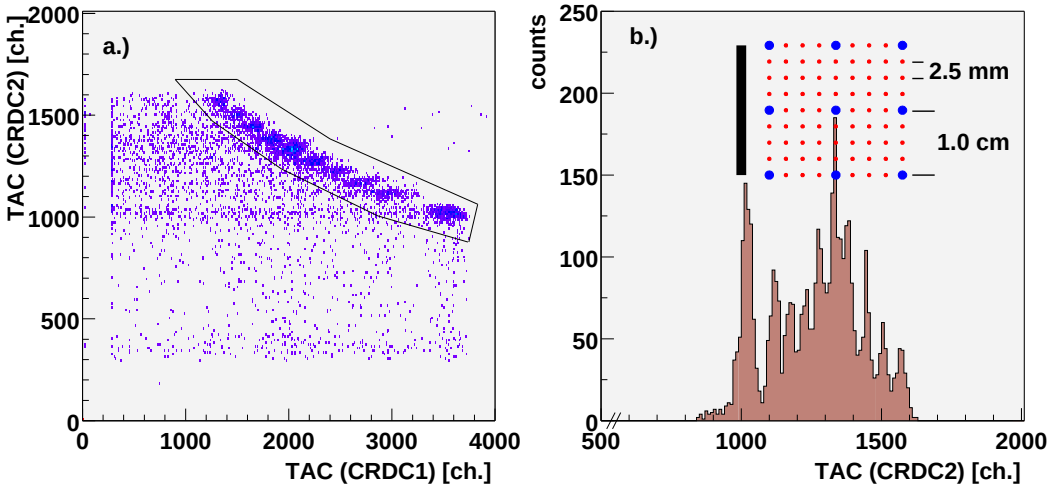

Figure 4.2: The calibration of the TAC signals. Plotted are the two TAC signals of the two CRDC's with respect to each other with a mask in front of the second CRDC (part (a)). Part (b) shows the projection onto the time signal of the second CRDC under the additional condition of the gate indicated in part (a). The hole structure of the mask is inserted to illustrate the peak structure of the time signals. The black bar next to the hole structure is part of a L-shaped structure cut out for orientation purposes.

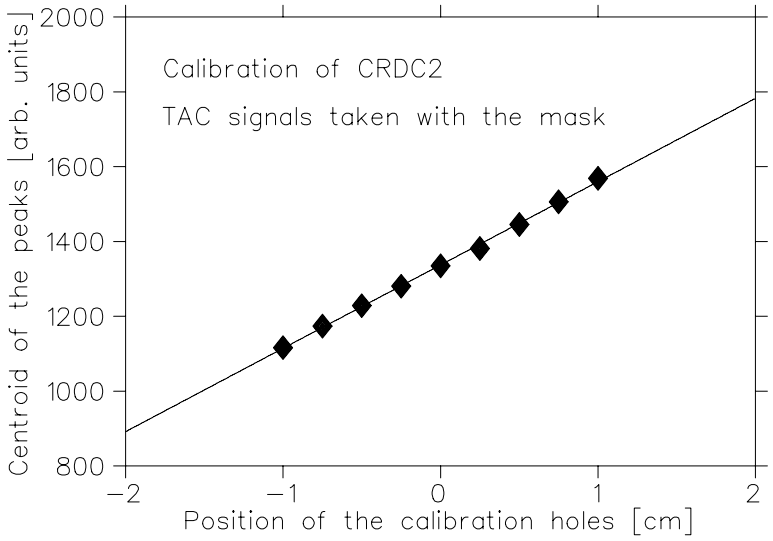

Figure 4.3: Correlation between the CRDC anode signal (here for the TAC signal of CRDC2) and the absolute position defined by a calibration mask. The centroids of the peaks in Fig. 4.2 were plotted versus their relative positions on the mask and then fitted by a linear function.

4.1.2 Energy Calibration of the Fragment Detectors

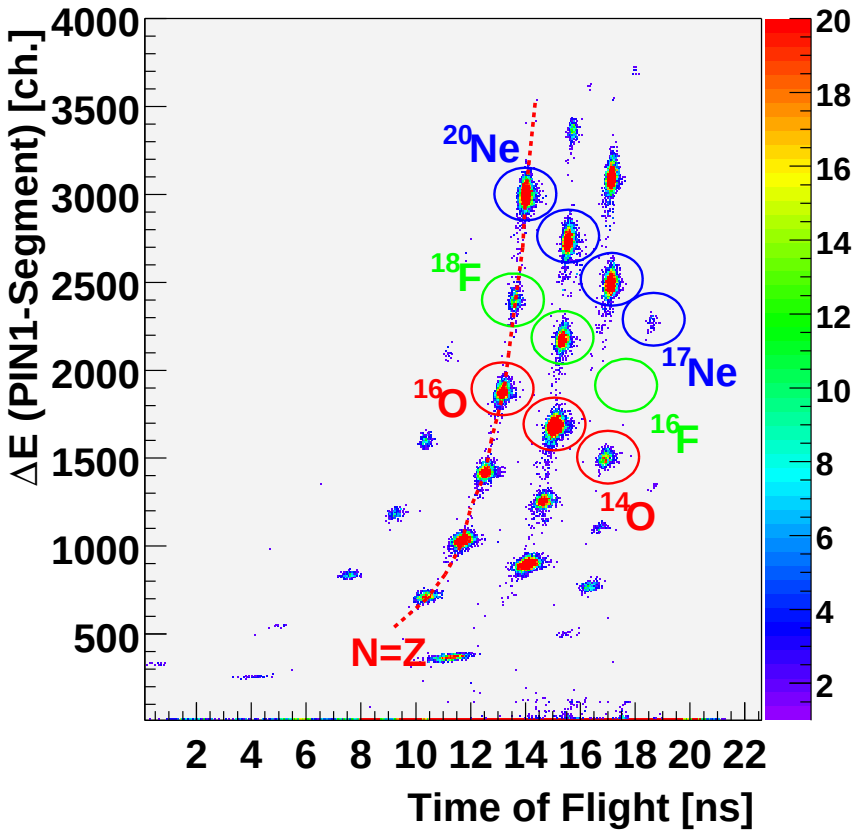

Figure 4.4: Particle identification for the calibration data. Plotted is the energy loss in one segment of the first PIN (PIN1) versus the time-of-flight. Without the degrader a wide variety of isotopes from the fragmentation of the ^{20}Ne primary beam reaches the detectors. The particle identification is guided by the $N = Z$ line (red dotted line), the missing unstable ^{16}F and the dominant intensity for the primary ^{20}Ne beam.

Fig. 4.4 illustrates the particle identification for the calibration runs. Plotted here is the energy loss in one specific PIN segment versus the time-of-flight measurement for a $B\rho$ setting of 2.15 Tm. With the degrader retracted for the calibration runs, the identification of the isotopes was guided first by the dominant intensity of the primary beam ^{20}Ne, second by the missing isotope ^{16}F, which is particle unstable and third by the $N = Z$ chain of isotopes ranging from ^{20}Ne down to ^{10}B. For the calibration of the fragment detectors ^{20}Ne and ^{14,15,16}O were used. Fig. 4.5 shows an example for the energy calibration of the fragment detectors for a typical PIN segment proving the linear characteristics of the calibration curve. Fig. 4.4 also gives an impression on the intensity ratio

between the fragmentation products, motivating the necessity to use a degrader wedge and the Wien filter to produce a ^{17}Ne beam with a reasonable purity. In order to determine the total energy of the ^{15}O fragments the individual

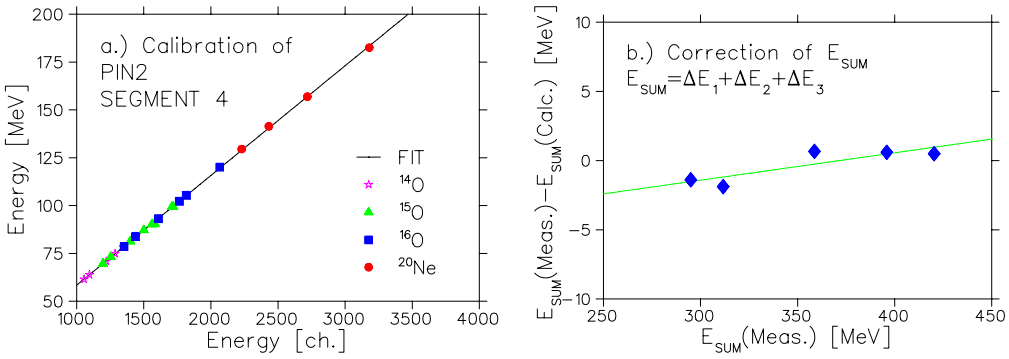

Figure 4.5: The left graph (a) shows an example of the energy calibration characteristics of a typical PIN segment. Plotted is the deposited energy versus the ADC-channel number for segment 4 of PIN2. Four different isotopes (^{14}O,^{15}O,^{16}O and ^{20}Ne) were used for the calibration. The right graph (b) demonstrates the sum energy correction. Plotted is the difference between the summed energy loss of the first three detectors and the expected energy loss versus the measured value obtained from the energy calibration as described in the main text. The agreement is fairly good and the deviation is less than 0.5% in the range of $\simeq$ 300 MeV.

energy signals of the fragments detectors had to be summed up. By doing this, potential systematic uncertainties in the individual energy calibration of the fragment detectors would sum up. While uncritical to the precision needed for the fragment energies themselves, even relatively small systematic uncertainties could disturb the precision of the decay energy derived from the kinematical reconstruction of the reaction. Therefore in a second step a correction function for the ^{15}O fragment sum energies was derived from a comparison of the calculated and the measured sum energies as displayed in 4.5 (b). Deviations were found to be smaller than 0.5% over an energy range of about 300 MeV. The energy resolution of the individual PIN segments ranged from 2% to 4% (FWHM). The resolution of the total fragment energy obtained by summing up the energy losses in the PIN-stack was about $\simeq$ 3.5%.

4.1.3 Energy Calibration of the Proton Detectors

The identification of the protons was facilitated by the fact that for the smaller calibration energies only protons could penetrate the detectors and reach the CsI-array. Fig. 4.6 shows a ΔE - E spectrum taken from an arbitrary strip of

the first (b) and the second (a) DSSD and a CsI-crystal behind those strips. Four of the calibration runs with different Bρ-settings are added together in order to display the proton band. The energy calibration of the DSSD's and of the CsI-array was performed under the condition of a proton identification. Fig. 4.6 also demonstrates that both DSSD systems worked fine in the calibration runs with the high gain setting for the proton detection. This will prove important later when interpreting the data taken with the first DSSD during the main experiment, when heavy fragments and protons simultaneously hit the first DSSD. Fig. 4.7 and Fig. 4.8 show the calibration characteristics for

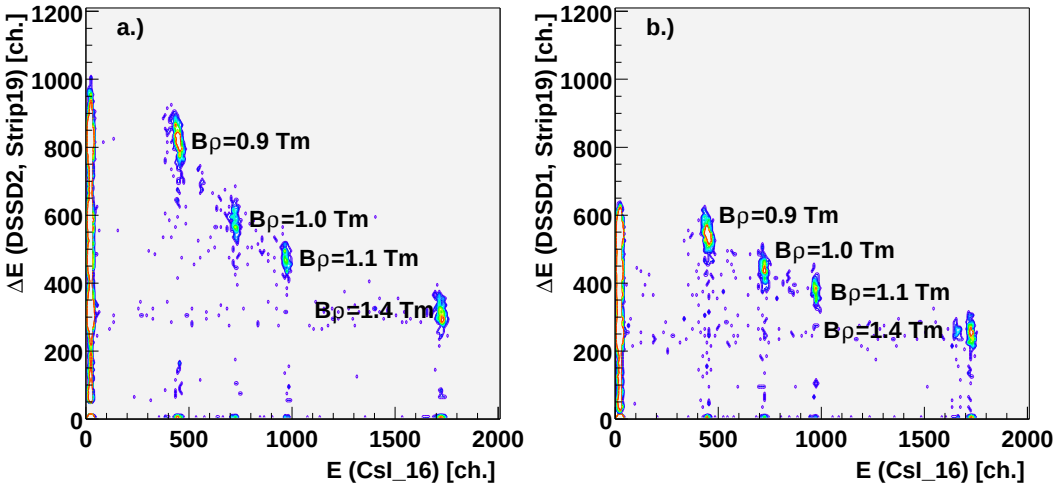

Figure 4.6: Proton identification for the energy calibration. Plotted is the energy loss signal of an arbitrary strip of DSSD1 (b) and DSSD2 (a) versus the energy of a CsI-crystal behind that strip. Four runs with different Bρ settings are added together.

typical detector units. Plotted is the deposited energy (corresponding to the total energy in the CsI crystals and the energy loss in the DSSD's respectively) versus the ADC-channel number. In the interesting energy range the correlation is strictly linear.

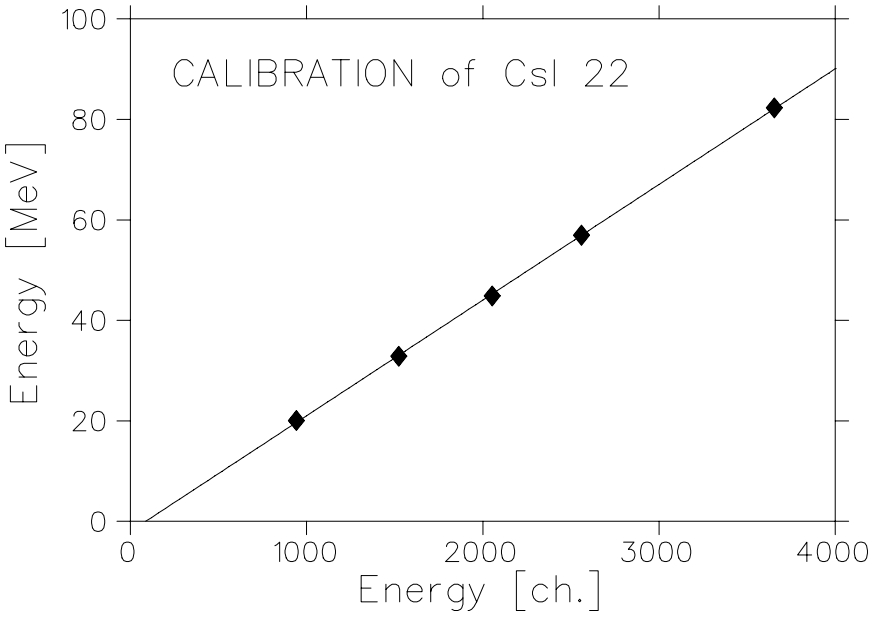

Figure 4.7: Energy calibration characteristics for a typical element of the CsI-array.

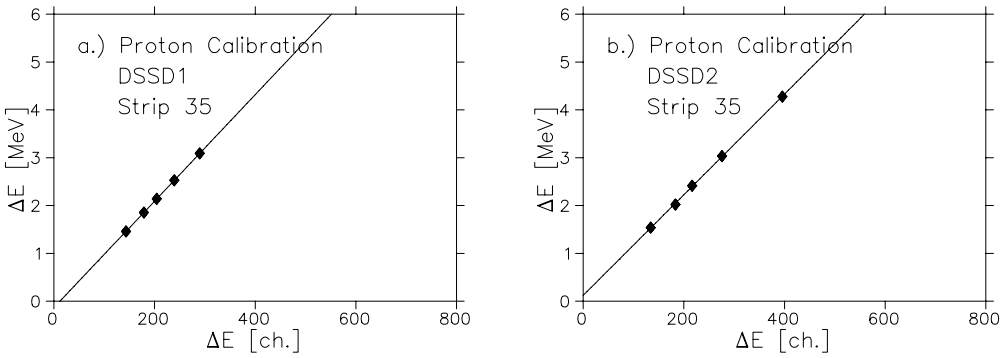

Figure 4.8: Example of calibration characteristics for typical segments of the two DSSD's. Plotted is the deposited energy loss of the protons in an selected strip versus the measured ADC-channel number for the 5 calibration runs.

Tab. 4.1 summarizes the calculated energy losses of the protons in the various calibration runs and detectors.

$B\rho$ [Tm]	Energy behind target [MeV]	ΔE(DSSD1) [MeV]	ΔE(DSSD2) [MeV]	E(CsI) [MeV]
1.4	89.73	1.46	1.54	82.31
1.2	66.49	1.85	2.02	56.94
1.1	56.01	2.14	2.41	44.87
1.0	46.32	2.53	3.03	32.86
0.9	37.40	3.09	4.28	20.06

Table 4.1: Energy losses of protons in the various proton detectors during the calibration. The energy difference between the initial proton energy after the target and the energy sum of DSSD1/2 and the CsI-array was deposited in the PIN diodes and is not listed here.

4.1.4 Determination of the Experimental Efficiency

The precise knowledge of detection and analysis efficiencies is an essential prerequisite for the extraction of numbers (e.g. B(E2) values, lifetimes) from the measured data. Certain efficiency losses such as incomplete charge collection in Si-detectors, pile up of signals destroying valid event signatures, and split charge collection in segmented detectors cannot be extracted from the Monte Carlo simulation that will be used later on in the analysis procedure. Those losses can be estimated with the help of the calibration runs and the downscaled singles events from non-reacting ^{17}Ne particles. Fig. 4.9 demonstrates the procedure to quantify efficiency losses for the fragment detectors. In the panels (a) to (c) the sum of the energy loss deposited in the quadrants of the first PIN diode (PIN1) is plotted versus the maximum signal in one of the segments. For case (b) and (c) a gate was applied on the particle hit multiplicity in PIN1 of $N_{\mathrm{HIT}} = 1$ and $N_{\mathrm{HIT}} = 2$, respectively. Multiplicity $N_{\mathrm{HIT}} = 1$ results in a diagonal for trivial reasons, while for multiplicity $N_{\mathrm{HIT}} = 2$ a different structure appears. It should be noted, that due to their small energy loss in the PIN diode the protons did not affect the hit multiplicity. Apparently there are events with double hits (pile up), where the sum of the energy loss signals is twice the maximum value. These events were rejected in the analysis where a multiplicity $N_{\mathrm{HIT}} = 1$ was required for the first two PIN diodes (PIN1 and PIN2). The resulting losses were determined in the following way: the loss of events due to the multiplicity gate can simply be obtained by subtracting the sum of events in spectra 4.9 (a) and (b). In addition, the incomplete charge

collection for the events with a multiplicity $N_{\mathrm{HIT}} = 1$ in PIN1 has to be taken into account. In Fig. 4.9 (d) the projection of the two-dimensional ΔE_{SUM}-ΔE_{MAX} spectrum for PIN1 onto the ΔE_{MAX}-axis is shown. The losses due to incomplete charge collection were determined by subtracting the left half from the right half of the peak in Fig. 4.9 (d). As a second measure a Gaussian shape was fitted to reproduce the width, height and positions of the peak and the extraneous intensity at the low energy side was taken as the number of events with incomplete charge collection. Both methods give similar results. This procedure was repeated for each of the segmented detectors. The losses in the second PIN diode (PIN2) were determined based on the number of valid events PIN1 and so on. Tab. 4.2 summarizes the detection efficiency for all detectors of the multi-stage particle telescope. For incomplete charge collection the average value of the efficiencies of the PIN diodes and the DSSD1 was taken. For the DSSD and the following segmented PIN diodes only multiplicities ≥ 1 were required. Thus no losses due to the multiplicity had to be considered. No gates were set on the energy loss signal of PIN5. For the proton

Detector	Multiplicity Gate	Incomplete charge collection	Total
PIN1	82.7(±2.0)%	92.6(±2.0)%	76.6 %
PIN2	96.1(±0.5)%	92.6(±2.0)%	89.0 %
DSSD1(low gain)	-	92.6(±2.0)%	92.6 %
PIN3	-	92.6(±2.0)%	92.6 %
PIN4	-	92.6(±2.0)%	92.6 %
Proton Detectors	-	81.1(±3.0)%	81.1 %
Total	79.5 %	55.2 %	43.9(±3.1)%

Table 4.2: Detection efficiency in the detectors after quantifying the losses due to random coincidences, incomplete charge collection, split charge collection and analysis conditions.

detectors the efficiency determination was somewhat more transparent . The CsI-crystals were optically decoupled from each other and cross scattering of protons between two CsI crystals were covered in the simulation. Thus, the effect of split charge collection in the CsI-array had not to be considered. Due to the low counting rate of about 100 coincidences per second between fragments and protons, random coincidences and pile up in the detectors used for proton detection did not affect the efficiency. The high gain (proton) signal of the first DSSD (as will be shown in section 4.2.4) was used to provide redundant tracking information but not to derive any analysis conditions. Thus, there was no need to consider efficiency losses for the first DSSD. Only incomplete charge collection in the second DSSD and in the CsI-array had to be considered. Since

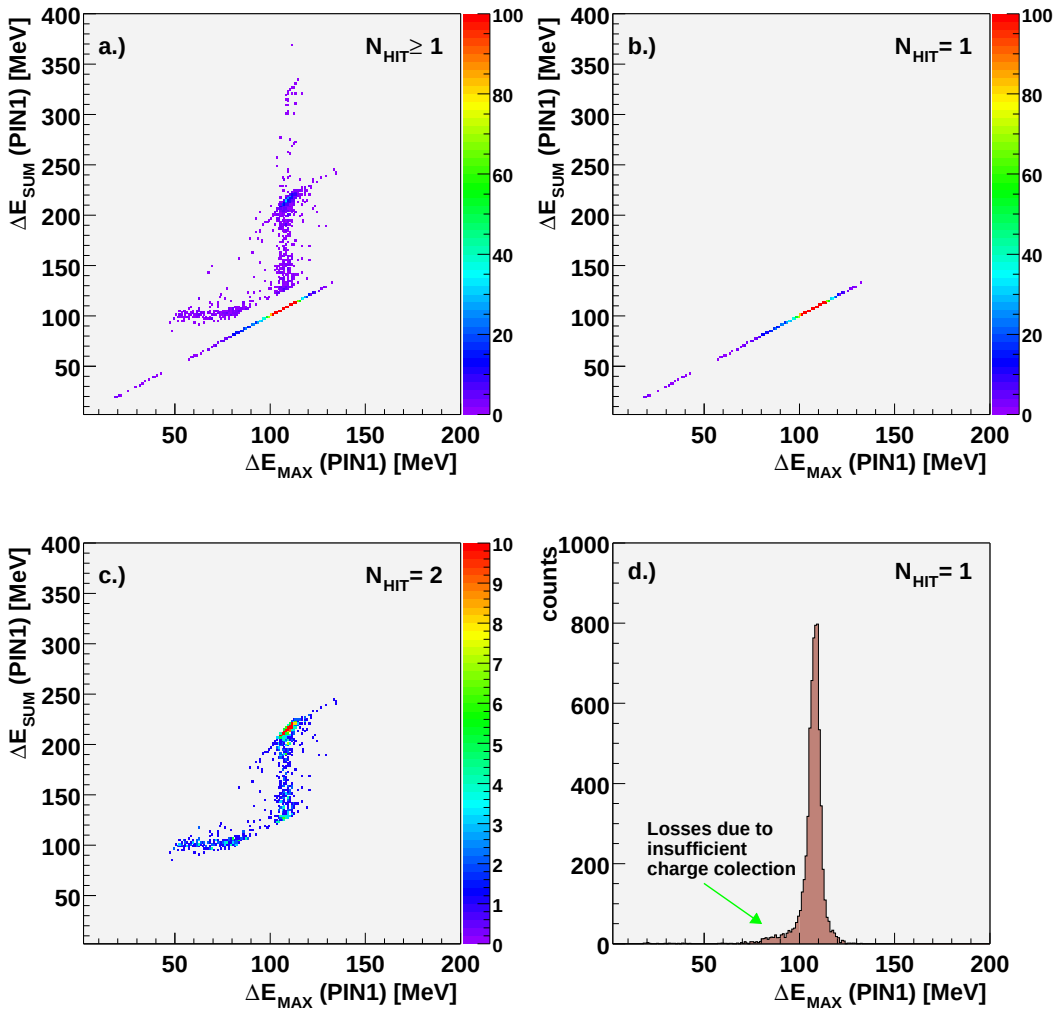

Figure 4.9: Efficiency losses in the particle detectors. In panel (a) to (c) the sum of the energy loss deposited in the quadrants of the first PIN diode is plotted versus the maximum value of the energy loss in one of the segments. In (b) and (c) a multiplicity in PIN1 of $N_{\mathrm{HIT}} = 1$ and $N_{\mathrm{HIT}} = 2$ is required, respectively. Panel (d) shows the projection of (b) onto the axis of ΔE_{MAX}. The losses due incomplete charge collection were estimated from this spectrum with the methods described in the main text.

the beam quality (e.g. emittance) of the calibration runs was rather poor, the beams could not be used to investigate losses in the CsI-array and the second DSSD2 analogue to the PIN diodes. This was done by varying the size of the analysis condition for 2p-events, which will be discussed later in Fig. 4.12 and 4.13. This restricts the analysis to an efficiency of about 80%, as can be seen in Tab. 4.2.

4.2 Identification of the Reaction Channels

In order to observe a 2p-decay and to reconstruct its energy in the center-of-mass system, it was necessary to identify the decay products (^{15}O and two protons) and to measure their 4-momenta in the laboratory frame. Despite the effort invested into the purification of the beam, it still contained impurities, which made it necessary to identify the incoming ^{17}Ne projectiles on an event-by-event basis.

4.2.1 Identification of the ^{17}Ne Projectiles

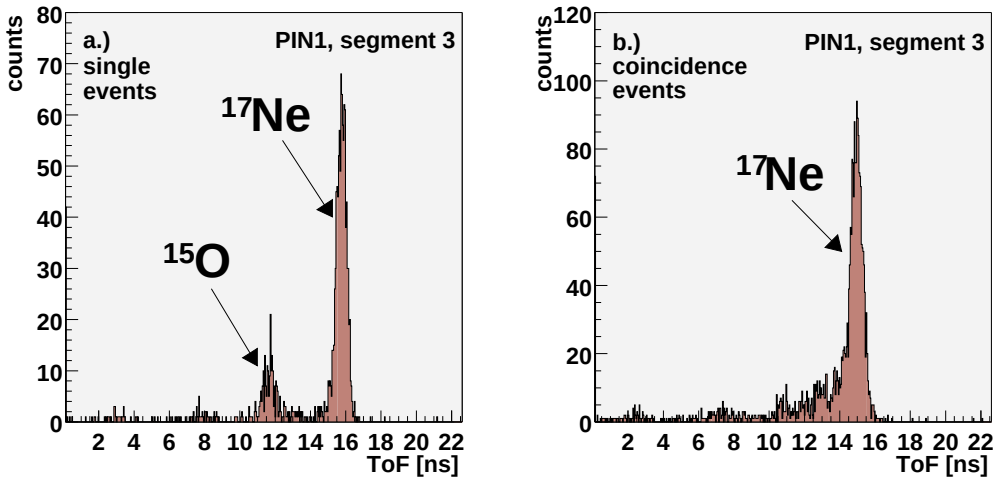

Figure 4.10: Time-of-flight spectra: From each run 2000 events were added together and plotted in these spectra to demonstrate the stability of the time-of-flight measurement. In panel (a) and (b) the time-of-flight spectrum is shown gated on events in PIN1, segment 3. Part (a) shows the spectrum gated on down-scaled single events still containing the remaining contaminant of ^{15}O, while part (b) displays the same spectrum gated on coincidences between fragments and protons. For each trigger type (coincidences, or down-scaled singles) and for each segment of PIN1 the time-of-flight gate on incoming ^{17}Ne projectiles was derived from the corresponding spectra.

The ^{17}Ne projectiles were identified by time-of-flight measurements as described in section 3.2.1. Fig. 4.10 (a) shows the measured time-of-flight spectrum for single events for a typical segment of PIN1, where 2000 events from each run were added together. One can identify the ^{17}Ne projectiles and separate them from the remaining ^{15}O contaminant. Part (b) shows the time-of-flight spectrum for fragment-proton coincidences now missing the ^{15}O contam-

inant. Efficiency losses occur due to the high counting rates rate in the timing scintillator. The number of events with a measured valid time-of-flight signal accounts only for $\simeq 80\%$ of the trigger events.

4.2.2 Identification of the ^{15}O Reaction Products

The ^{15}O reaction products had to be identified without measuring the complete energy deposited in the PIN-diodes due to electronics problems with the last detector (PIN5). Tab 4.3 contains the calculated individual energy losses and energy sums which were expected in each detector for different reaction scenarios, including ^{17}Ne projectiles passing the target and interacting with different parts of the detector stack. The energy losses of the ^{17}Ne projectiles and the ^{15}O reaction products were calculated, assuming that the reaction took place in the center of the target or the detectors while neglecting the small contribution of the energy loss of emitted protons. Tab. 4.4 shows the range of the expected energy losses for those 2p-decay events, which originate from the target (B) or from the first PIN diode (C). The range is basically determined by the momentum spread of the beam of $\frac{\Delta P}{P} = 3\%$ and by the straggling of the energy loss in the target and PIN1, respectively. A comparison of the two tables for scenarios B and C reveals the impossibility to discriminate between these two reaction scenarios by just using the energy measurements. Fig. 4.11 demonstrates the identification of the ^{15}O reaction

Reaction Scenario	PIN1 [MeV]	PIN2 [MeV]	DSSD1 [MeV]	PIN3 [MeV]	PIN4 [MeV]	PIN5 [MeV]	$\sum_{1-3}$ [MeV]	$\sum_{1-4}$ [MeV]	$\sum_{1-5}$ [MeV]	$\sum_{1-6}$ [MeV]
A	108.9	121.7	327.7	355.6	0	0	558.2	913.8	913.8	913.8
B	68.3	73.4	173.2	106.7	134.8	257.4	314.9	421.6	556.3	813.8
C	96.7	75.3	179.3	113.5	151.4	204.4	351.3	464.8	616.3	820.6
D	108.9	98.7	188.9	123.8	188.3	117.4	396.5	520.3	708.6	826.0
E	108.9	121.7	257.1	149.5	213.1	0	487.7	637.2	850.4	850.4

Table 4.3: Calculated energy loss of the projectile and heavy reaction product for different reaction scenarios: non-reacting ^{17}Ne in the target or in the detectors (A), a reaction in the target (B), in PIN1 (C), PIN2 (D) and in the DSSD1 (E), respectively. The last four columns list the resulting sum energies for 3 to 6 detectors. Those values can be compared to the measurement aiming at an identification of the reaction scenario.

products. In this ΔE - E plot ^{15}O fragments can clearly be identified according to the predictions of Tab. 4.3, marked by the circle line. However, this condition alone cannot serve as a clean identification, since breakup reactions in the first PIN diode produce a large background, within the area indicated by the blue rectangle overlapping the ^{15}O region. The effectiveness of the ^{15}O identification will be discussed in section 4.4.1.

Detector	Range of energy loss (B) [MeV]	Range of energy loss (C) [MeV]
PIN1	66.0 - 70.8	66.9 - 112.2
PIN2	70.5 - 76.7	71.7 - 79.5
DSSD1	163.9 - 184.7	167.7 - 195.5
PIN3	96.5 - 119.4	100.5 - 131.6
PIN4	116.9 - 169.6	123.2 - 245.8

Table 4.4: Range of calculated energy losses for the 2p-decay events originating in the target and in PIN1 in order to obtain the energy loss range. The momentum spread of the secondary beam and the spread of the energy loss due to the energy straggling due to the target thickness were taken into account.

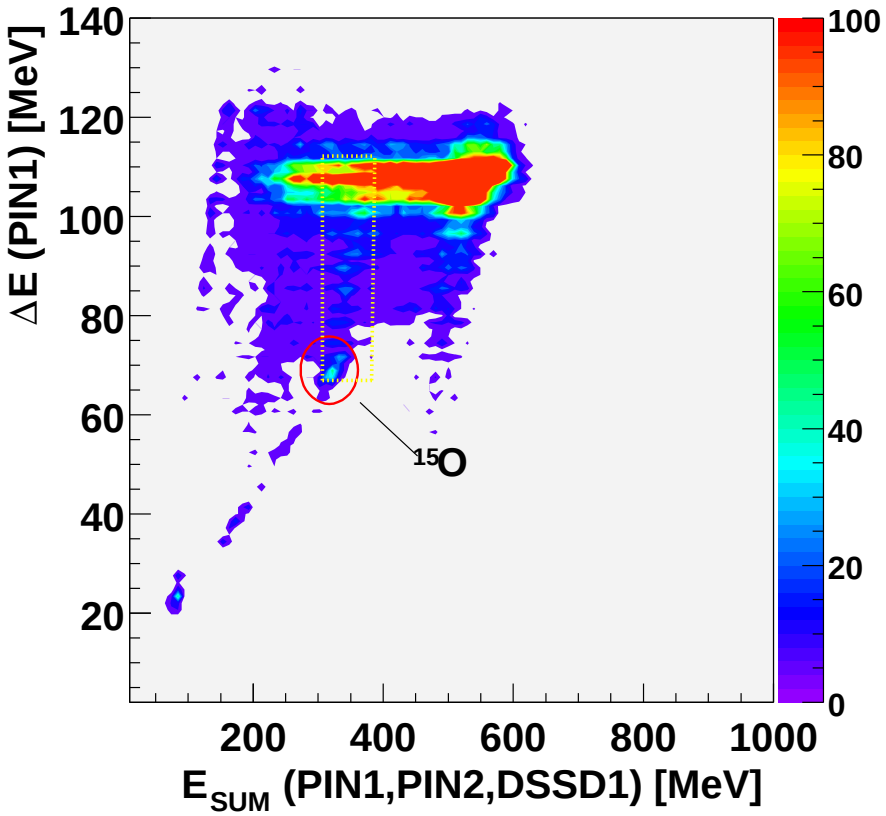

Figure 4.11: Identification of the ^{15}O reaction products. The energy loss in PIN1 is plotted versus the sum of the energy deposited in the first three detectors (PIN1, PIN2, DSSD1). The peak corresponding to the ^{15}O reaction products (marked by the circle) could be identified at the expected energetic position. The rectangle corresponds to events, where the ^{17}Ne breaks up in the first PIN diode as discussed in Tab 4.4.

4.2.3 Identification of the Emitted Protons

In order to identify the emitted protons, the energy loss of the light particles was measured in the second DSSD (DSSD2) and their total energy in the CsI-array. Fig. 4.12 demonstrates the identification of two-protons hits. Plotted is the sum of the energy loss in the second DSSD versus the sum energy deposited in the CsI-array without requiring the identification of the heavy fragment. It is possible to identify an intense band corresponding to proton signals (labelled with p). In this ΔE_{SUM} versus E_{SUM} plot two proton events should appear exactly at twice the energy and twice the energy loss of the p band. Indeed, the

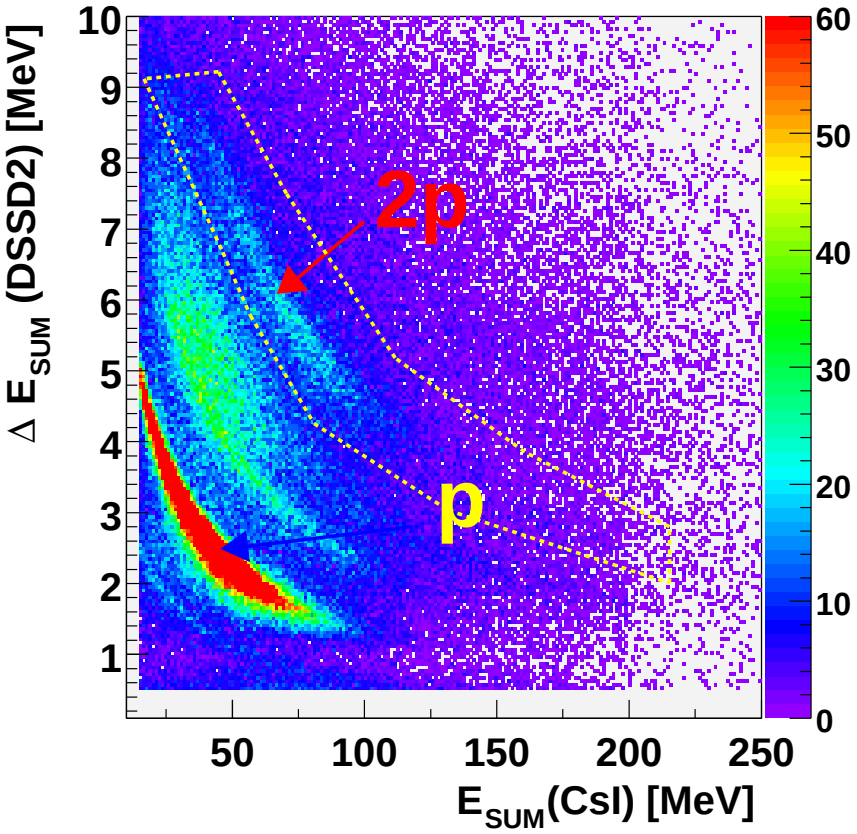

Figure 4.12: Identification of the two proton events . Plotted is the sum of the energy loss in the second DSSD vs. the energy deposited in the CsI-array under the condition of ^{17}Ne in the entrance channel. The brightest band corresponding to single proton events can clearly be identified. At twice the energy loss and twice the energy of single proton events 2p-events should be visible. This area is surrounded by the dashed lines. Some intensity falls into this area, shifted to higher values for ΔE_{SUM} and higher values for E_{SUM} since this plot still contains breakup reactions in the fragment detectors.

area labelled with "2p" surrounded by the box shows evidence for 2p-events shifted to higher energy losses and smaller energies, since this plot still contains breakup reactions in the fragment detectors, which would emit the two protons with smaller kinetic energies in the laboratory frame resulting in higher values for ΔE_{SUM} and smaller ones for E_{SUM}. If additionally the identification of ^{15}O fragments in the reaction channel is required, the 2p-band can be distinguished even better from background events (Fig. 4.13). A third band marked with X can be seen in Fig. 4.13. These counts correspond to events, where both protons were identified in the DSSD, but only one of them was registered in the CsI-array, since the other one was deflected to larger angles compared to the acceptance of the CsI-array. This could happen, because the second DSSD was covering a slightly larger solid angle compared to the CsI-array.

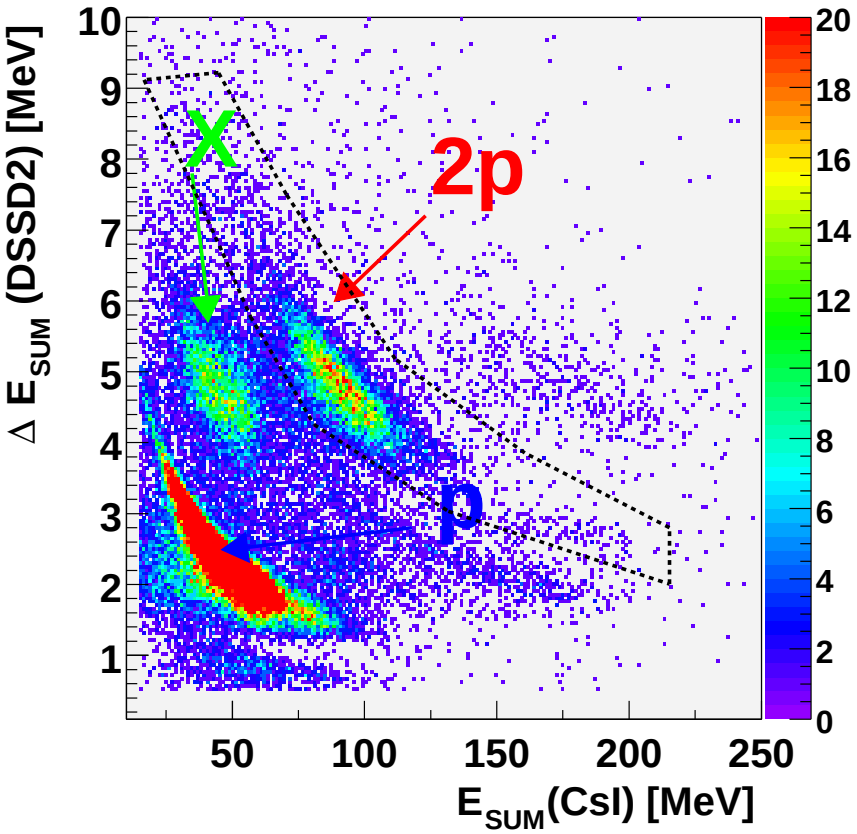

Figure 4.13: Analogue to Fig. 4.12 the ΔE_{SUM} - E_{SUM} distribution measured with the second DSSD and the CsI-array, but here requiring the identification of ^{15}O reaction products. Three bands can be identified. The p- and the 2p-band and a third band, marked with X, which corresponds to events in which two protons were detected in the DSSD, but only one in the CsI-array. The 2p-band is marked again by the dashed line.

After identifying the 2p-events the position measurement in the second DSSD (DSSD2) could be correlated with the position measurement in the CsI-array in order to assign a trajectory and an energy value to each of the protons. In order to achieve this the hit pattern in the second DSSD has to be examined as a first step. If two protons hit the DSSD typically two strips on each side would fire. The intersections of these strips define four positions, i.e. four pixels (out of 1600) that could be interpreted as potential hit positions as demonstrated in Fig. 4.14. Obviously only two of these pixels correspond to the physical hit pattern and the analysis procedure has to distinguish between real and spurious proton hits in the DSSD's. This was done by analyzing the signal amplitude of the front and the back side of the second DSSD. In case of a proton hitting a given pixel, the respective energy loss signal amplitudes produced on the front and the back side of the DSSD should ideally be equal. This condition allowed to identify the pixels associated with protons hits. The accuracy of this method can be demonstrated with Fig. 4.15. In part (a) the signal of the front side of DSSD2 is plotted against the signal registered with the back side, resulting in a distribution that shows only little deviations from the expected main diagonal. This can be quantified by projecting the distribution along the line of a linear fit function applied to reproduce the ΔE_{f}-ΔE_{b} correlation. The resulting difference peak centered at zero is displayed at Fig. 4.15 (b).

The next step related the two measured proton signals in the DSSD with

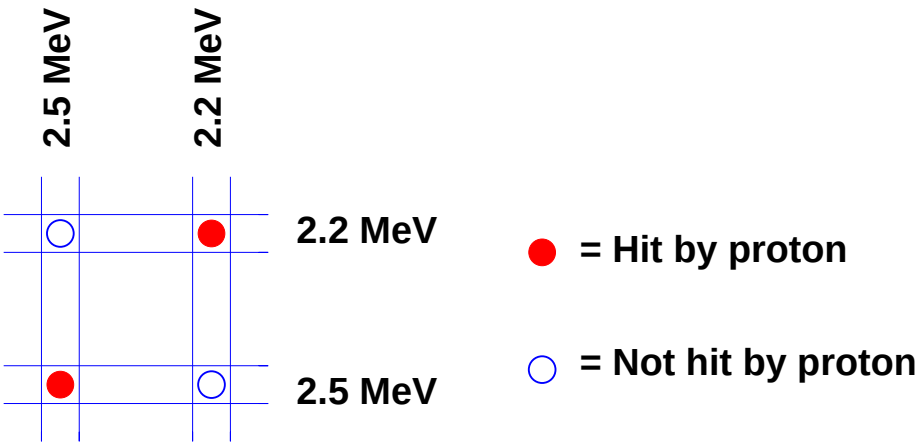

Figure 4.14: Principle of the hit identification in the DSSD's (assuming no double hits in one strip). If two protons hit the DSSD, four pixels could be identified as hits. The correct pair of hits (sitting on a diagonal in this schematics) could then be identified by requiring equal signal amplitudes on both sides of the detector (as indicated by the arbitrary example of two proton hits with 2.2 MeV and 2.5 MeV, respectively).

the two signals measured in the CsI-array. This was done by using the fact that the two protons were emitted from the same place. Therefore it was possible to correlate the signals in the DSSD with those in the CsI-array. Fig. 4.15 (c,d)

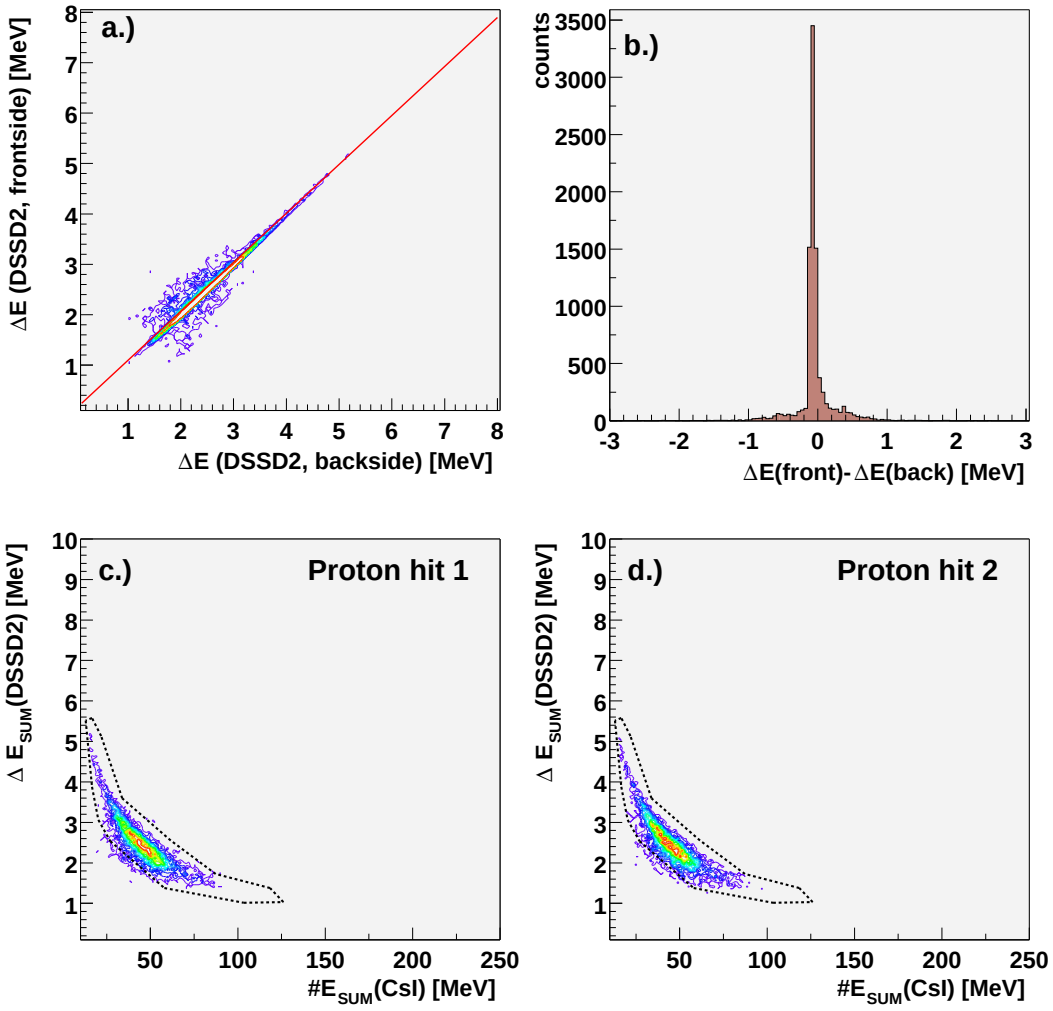

Figure 4.15: For one of the identified protons the energy loss in the front side of DSSD2 is plotted against the energy loss in the back side (a). In most of the cases the deviation between the two signals is very small. The distribution that mostly follows the main diagonal was approximated by a linear fit function, onto which the distribution was projected in order to obtain the difference spectrum of part (b) for a quantitative description of the effect. Panels (c) and (d) show the individual ΔE - E spectra for the two protons detected in one event. The bands are comparable to the proton band in Fig. 4.12 and Fig. 4.13. The area inside the dashed line indicates the analysis conditions for the individual identification of the two protons in a single event.

shows the ΔE - E spectra for each of the individual protons. For the further analysis the condition was defined that each of the two detected protons had to be located within the region characterized by the proton band as defined by the gate in Fig. 4.15 (c,d).

4.2.4 Identification of 2p-Bands in the First DSSD

As already discussed, the first DSSD (DSSD1) was operated in a two-fold way in order to detect both heavy fragments and light particles by different gain settings. The detection of the heavy fragments was already discussed in section 4.2.2, DSSD1 served here as one contributor to determine the total energy of the heavy reaction product. In this section the high-gain setting of the DSSD1-setup will be used for the proton-hit identification. However, the energy loss of heavy fragments and protons in the first DSSD differed by about two orders of magnitude, giving rise to a significant amount of cross-talk between adjacent strips in case of heavy fragment hits. Requiring the clear identification of 2p-events with the CsI-array and the second DSSD (via the two-dimensional gate-condition indicated in Fig. 4.13 around the 2p-distribution) and trying to generate a similar $\Delta E_{\mathrm{SUM}} - E_{\mathrm{SUM}}$ spectrum as in Fig. 4.13 using the ΔE_{SUM} of the first DSSD, a completely different picture appeared in Fig. 4.16 (a). The spectrum shows almost no structure, especially not the p- and 2p-bands as expected. Reminding the clear proton band signature observed in the proton calibration runs, this behaviour appears rather surprising at first thought.

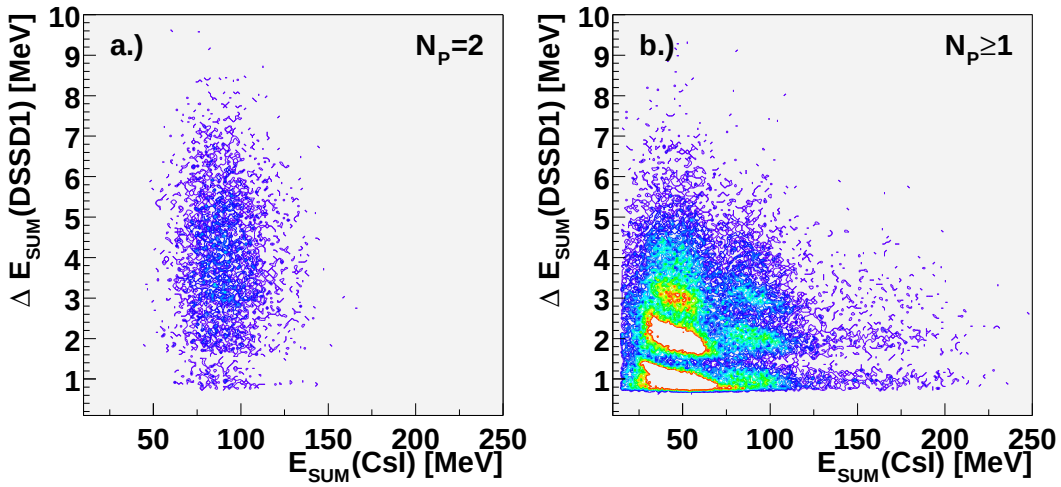

Figure 4.16: Identification of 2p-bands in the first DSSD. Part (a) displays the ΔE_{SUM} - E_{SUM} spectrum with ΔE_{SUM} measured in the first DSSD under the condition of the identification of 2p-events as shown in Fig. 4.13, resulting in a structureless distribution. Part (b) shows the same quantities without the 2p-condition, but additionally neglecting those strips which are suspected to be influenced by the hit of a heavy fragment or by their cross talk. Now a band-like structure shows up.

The explanation takes into account that this DSSD was hit by the heavy fragment (^{15}O) and the protons at the same time. As mentioned, the ^{15}O fragments were depositing a factor of $\simeq$100 more energy in the detector. Therefore, if

just about 1% of the charge created by the heavy fragment is collected by the neighbouring strips or a cross talk signal of a similar amplitude is induced, the signal heights there were of the same order of magnitude as the proton signals. Thus, it is necessary for the analysis of the high gain data of the first DSSD to reject not only the strips which were hit by heavy fragments, but also the two adjacent neighbours. In the analysis procedure these strips were blocked by forcing their signal amplitude to a value of zero. A second effect was related to this: As discussed earlier, a large background contribution from breakup reactions the Si-detectors could be identified. If the ^{17}Ne projectile breaks up in one of the detectors (e.g. in the PIN1 and PIN2 right in front of DSSD1), the reaction takes place close to the first DSSD. In this case a significant amount of the reaction products will hit neighbouring strips in the DSSD with a high probability that a proton and the ^{15}O fragment were detected in the same strip or hit adjacent ones. Again it is necessary to reject the channels responding to the ^{15}O fragments in the analysis of the high gain setting of DSSD1. Fig. 4.16 (b) shows a similar ΔE_{SUM} - E_{SUM} spectrum (without the requirement of the 2p-identification) now including the blocking of the channels affected by the ^{15}O hit. A band-like structure appears which can be understood by looking separately at the front and the back side of the first DSSD. In Fig. 4.17 (b) and (c) the sum of the energy loss in the first

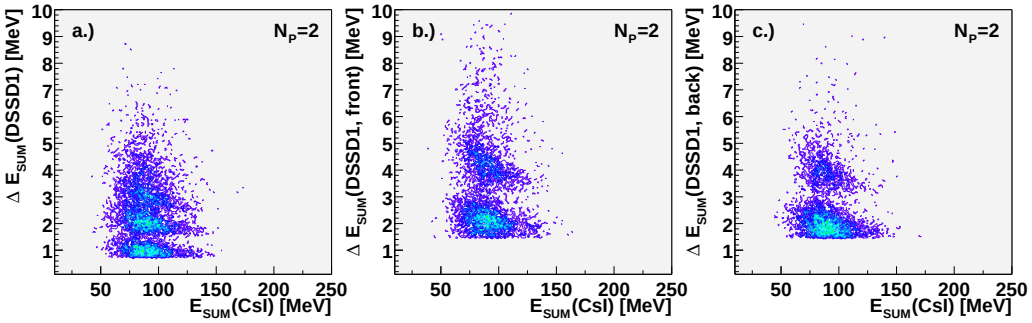

Figure 4.17: Explanation of the band structure of the first DSSD. Part (a) is similar with Fig. 4.16 (b); but additionally two proton hits were required. In part (b) and (c) the deposited energy in the CsI-array is plotted against the energy loss of either the front and or the back side, respectively.

DSSD was plotted individually for the front and the back side (for all three spectra of Fig. 4.17 the clear identification of 2p-events was required). In each of them two bands can be distinguished. The more intense one has an energy loss of around $\simeq$ 2 MeV, the other one twice of that. This means that in most of the events one strip is blocked by the heavy fragment, resulting in half the ΔE_{SUM} compared to a complete 2p-event. Summing up the energy losses of

two sides of DSSD1 and dividing by two results in the structure shown in the left panel of Fig. 4.17. Events with a complete signal on both sides are almost not existing. Gating on those bands in the spectra of Fig. 4.17 (b,c) allowed to identify the hits on each side and to extract from there the position information needed for the particle tracking. If a proton hits a strip blocked by the heavy fragment (which would be either the strip hit by the fragment itself or one of the adjacent channels), the position measurement was derived from the strip position attributed to the fragment hit. Thus, the precision was $\pm$ 1.5 mm, when the proton hit a blocked channel.

4.3 Particle Tracking

As discussed in section 3.5.1, the precision of the alignment of the beamline and the detectors was limited after lifting the detector setup. However, the different tracking methods could be used to compensate for that. Unfortunately, there was no calibration beam available, which could be used to align the setup all at once, any available calibration beam would be either too light to be detected in the CRDC's or too heavy to reach the CsI-array. Therefore it was necessary to apply a two-step procedure. Since the positions of the two DSSD were absolutely fixed with respect to each other and also centered and fixed within the beam pipe, they were used as a reference. With the hit positions measured in the two DSSD's the expected positions in the CsI-array were calculated and compared with the actually detected ones. As a test the target interaction point was calculated with a particle tracking from DSSD1 to DSSD2 and alternatively from DSSD2 to the CsI-array. This was performed using the proton calibration beams. The deviation of the measured position of the center of the beam spot using those two methods was less than 0.3 mm. Subsequently, the complete detector array could be considered to be internally aligned. The events in the 2p-band (see Fig. 4.13) were used to determine the expected beam spot at the positions of the two CRDC tracking detectors via backwards-tracking. This calculated beam spot was then compared with the one measured in the CRDC's. Finally the positions in the CRDC's could be corrected in the software analysis to achieve a consistent alignment.

4.3.1 Tracking with the CRDC's

With two tracking detectors in front of target the interaction point in the target is in general determined by the extrapolation of the two measured interaction points in the detectors to the target. Due to the efficiency losses in the

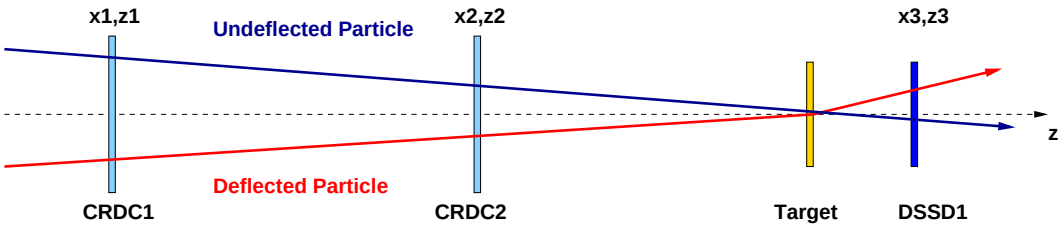

Figure 4.18: This sketch demonstrates the principle of the drift ellipsoid method used to determine the interaction point in the target as described in the main text. In order to determine the properties of the incoming the ^{17}Ne singles events were used, where the projectiles did not react in the target and followed a straight path as indicated by the blue line. The knowledge about the beam properties (i.e. the relation between projectile position and slope) could then be used to reconstruct the target position of the deflected particle with only one position measurement in front of the target.

CRDC's this method was not applicable in the present analysis as discussed earlier. Thus, for the particle tracking with the CRDC's the drift ellipsoid method was used. This method is discussed in detail in [Chr98a], where examples of the effectiveness of that method can be studied. The principle of the drift ellipsoid method is based on a measurement of the beam properties using non-reacting projectiles (in our case the non-reacting ^{17}Ne) and position measurements in front and behind the target. From that measurement a relation between beam position and slope is derived. Plotting the position versus the slope results in the picture of the so called "phase space ellipsoid" [Wil96] and in a relation between a measured detector position and the slope of a projectile. Considering that the distance between the detectors and the target contained no optical elements (called "a drift" in accelerator physics, thus the name "drift ellipsoid method"), the target position can be derived just with one position measurement in front of target using the knowledge of the beam properties. Fig. 4.18 demonstrates the principle for the drift ellipsoid method. Singles events, from non-reacting ^{17}New were used for the determination of the beam properties, represented by the straight blue line in Fig. 4.18. For those events the x- and y-position in the two CRDC's were taken together with the x- and y-positions in the first DSSD. For each coordinate and for each CRDC the slope of the beam, i.e. the position deviation from the central axis between the CRDC and the DSSD defining a divergence angle, called slope, is plotted as a function of the position at the CRDC. A linear function was fitted to the ellipsoid resulting in a fixed relation between the slope and the position of the beam that could be used for the particle tracking. For the inelastic events, where ^{17}Ne reacted in the target and the ejectile was deflected before its detection in DSSD1, the position in the CRDC had to be measured and the slope had to be taken from the fit function derived from the singles events. With the

slope parameter the the extrapolation to the interaction point in the target could be performed. This method allowed the determination of the incoming projectile trajectory even if one of the tracking detectors failed. For each coordinate and for each CRDC an individual drift ellipsoid could be derived and thus an individual extrapolation to the interaction point on the target. Whenever two values for one coordinate were available (i.e. both CRDC's delivered valid position information), the mean value was taken. The error of the mean value was a measure for the uncertainty of the position determination.
The slope parameter of the beam was dependent on the beam transport magnet settings which had to be tuned during the run time. Hence, it was necessary to derive the relation between the position and the slope parameter for each run. Fig. 4.19 (a) illustrates the drift ellipsoid for the y-coordinate of the right-handed coordinate system taken between the first CRDC and the first DSSD together with the result of the fit. A good test for the precision of the drift ellipsoid method is the comparison of the extrapolated position at the first DSSD with the measured one, performed with the undeflected ^{17}Ne particles from the the singles events trigger type. The difference between the extrapolated and measured positions at DSSD1 for both coordinates was derived and illustrated in Fig. 4.19. Fitting the distribution in both coordinates with a Gaussian distribution gives an error of the position of 3.6 mm and 2.6 mm for the x- and the y-coordinate, respectively.

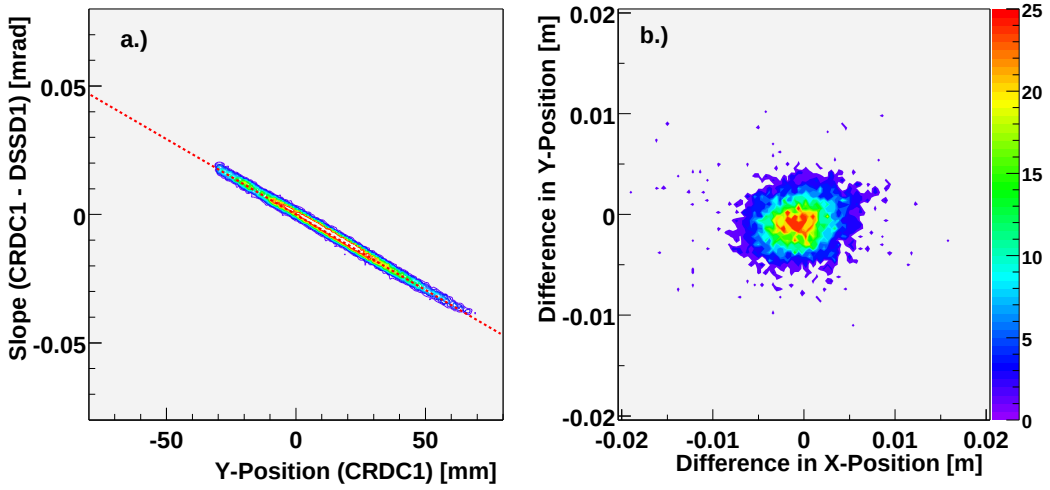

Figure 4.19: Result of the drift ellipsoid method. Part (a) shows a typical drift ellipsoid measured using the first CRDC and DSSD1. Part (b) shows the difference of the extrapolated and the measured position in DSSD1. The narrow peak centered around zero gives an impression of the precision achievable with this method.

4.3.2 Backwards-Tracking with the Proton Detectors

The possibility to determine the interaction point on the target by backtracking of the protons, i.e. using the position information behind the target, was one of the major improvements of the new experimental setup. Since the position of the protons was measured in the two DSSD's and with reduced precision also in the CsI-array, three redundant possibilities to determine the interaction point in the target were offered by the detector setup.

1. Determination of the particle trajectories by using the two DSSD's ("S1/S2-tracking").
2. DSSD1-to-CsI tracking by using the first DSSD and the CsI-array ("S1/C-tracking").
3. DSSD2-to-CsI tracking by using the second DSSD and the CsI-array ("S2/C-tracking").

In all of these cases, an individual emission origin on the target was calculated via extrapolation for each individual proton. The interaction point on the target was calculated as the middle position of the two emission points.

Fig. 4.20 demonstrates the different methods and shows how the interaction point on the target is determined from the calculated emission origins. In Fig. 4.20, however, an unavoidable error in the measurement is implied, due to the finite granularity of the detectors and due to effects such as angular scattering, which will be discussed in section 4.3.6. The spatial separation of the two extrapolated proton emission origins can serve as a first order estimate of the accuracy of the backward-tracking. This error was calculated for every tracking method so that it was possible to calculate the weighted average of the calculated interaction points. It should be noted that for events, where it was not possible to identify the hit pattern in the first DSSD due to the influence of the heavy fragment, only the S2/C-tracking method was available.

Fig. 4.21 (a) compares the backtracking methods with the forward-tracking using the drift ellipsoid method. For each coordinate the difference of the calculated interaction point positions obtained by the two methods were plotted in a two-dimensional display. The distribution is centered around a position located at (X,Y)=(0.80(46) mm, 0.10(42) mm). For the final determination of the interaction point on the target the weighted average of all backward-tracking and forward-tracking results was taken. From the errors Δx and Δy of

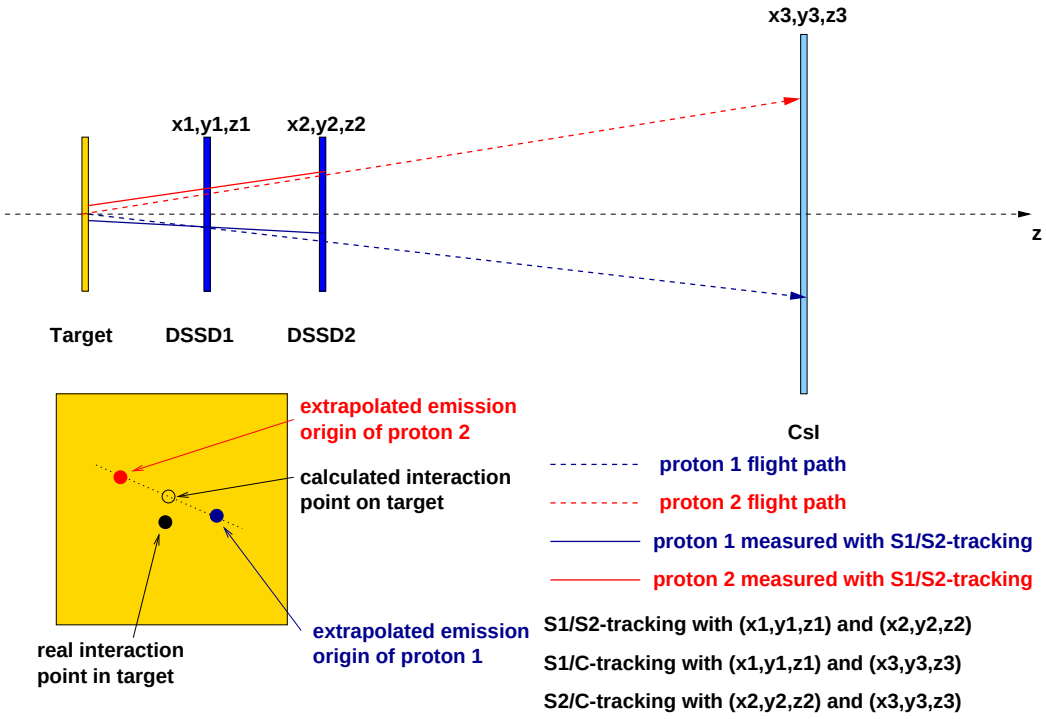

Figure 4.20: This sketch demonstrates the principle of the backward-tracking method for the determination of the proton trajectories. Shown in the upper part of the figure is the case where the two DSSD's were used for the backwards-tracking ("S1/S2-tracking"). Due to finite granularity the obtained proton trajectories (solid line) differ slightly from the true trajectories (dashed lines). Then the trajectory for each proton was extrapolated onto the target. The interaction point on the target was calculated as the center position between the two extrapolated emission origins of the protons and might differ from the true interaction point. The graph also indicates which sets of coordinates were used for the different tracking methods.

the x- and the y-coordinate the radial error was derived as $\Delta r = \sqrt{\Delta x^2 + \Delta y^2}$ and displayed in Fig. 4.21 (b). The discrete structure of this distribution is due to the use of different tracking methods.

4.3.3 Determination of the Breakup Position Along the Beam Axis

As already discussed in the framework of Fig. 4.11, it was necessary to separate the contribution from ^{17}Ne breakup reactions in the first PIN diode from the valid events, where the breakup happened in the target. Selecting the right ΔE-E region in Fig. 4.11 was not sufficient to produce clean spectra. Thus it

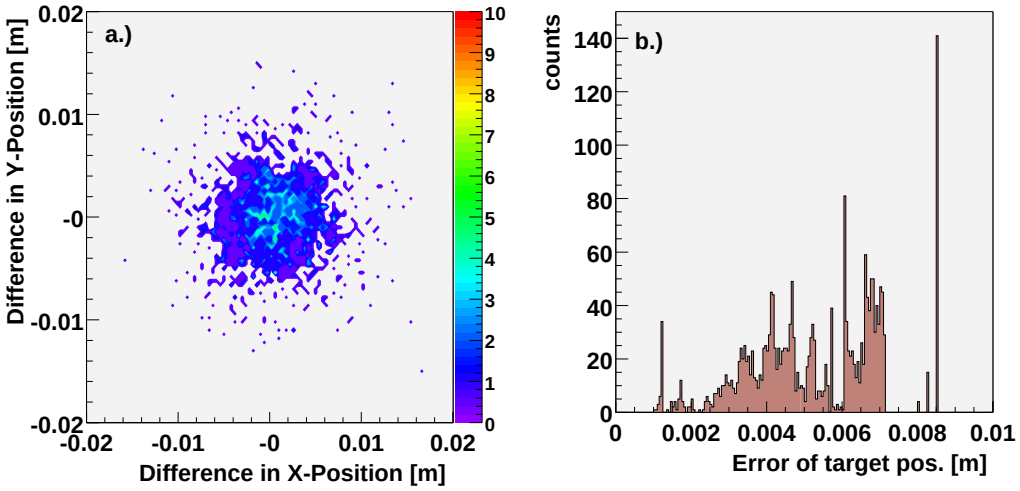

Figure 4.21: Part (a) shows the difference between reaction points on the target determined via forward-tracking and backwards-tracking (for the latter averaged over the three different redundant methods). Part (b) shows the resulting radial error Δr of the interaction point on the target, where $\Delta r = \sqrt{\Delta x^2 + \Delta y^2}$, and Δx and Δy are the errors taken from the weighted average of all tracking methods. Since sometimes certain tracking methods could not be applied one does not expect a smooth distribution.

was necessary to use a second tool. The three position measurements of the protons behind the target could also be used to determine the breakup position along the beam axis (z-axis), as demonstrated schematically in Fig. 4.22. In the three dimensional coordinate system the measured trajectories of the protons will be warped straight lines. Thus the position measurements in the two DSSD's and in the CsI-array were used to determine the z-coordinate of the crossing point of the proton trajectories individually for the xz- and yz- plane. The breakup position along the z-axis was then calculated as the average of those two values. Analogue to the determination of the interaction point on the target the three systems (DSSD1-CsI, DSSD2-CsI and DSSD1-DSSD2) could be used separately and the weighted average of those values could be taken. However, it should be noted that those breakup reactions in PIN1 or PIN2 happen so close to DSSD1 (about 3.5 cm) that it was nearly impossible to detect the two protons separately. Moreover, with a rather high probability the two protons hit a segment in DSSD1 (or its neighbouring channel) where already the heavy fragment was detected as investigated in section 4.2.4. Thus, in those cases the breakup position is typically determined only by the second DSSD and the CsI-array. In the following figures, the accuracy of this method

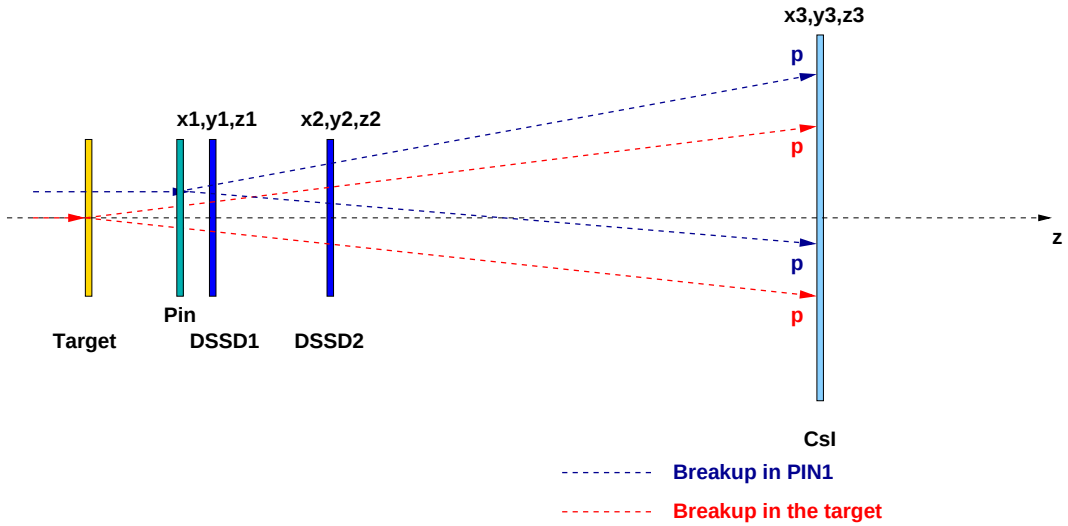

Figure 4.22: Two breakup scenarios are shown in this sketch: the breakup in the target and the breakup in the first PIN diode (PIN1). Using the position information from the two DSSD's and the CsI-array the z-coordinate could be calculated where the two protons cross in the xz plane. This was repeated analogue for the yz plane as well.

will be discussed. In order to produce those spectra, events were analyzed, requiring ^{17}Ne in the entrance channel and protons in the exit channel. For the heavy fragment two scenarios were chosen:

(a.) An energy loss signal characteristic for ^{15}O in all detectors except in PIN1 was selected, where an energy loss of ΔE=70-92 MeV was required. Those events should correspond to breakup reactions in PIN1.

(b.) An energy loss signal characteristic for ^{15}O in all detectors except PIN1 was selected, where an energy loss of ΔE=64-70 MeV was required. Those events should mainly correspond to breakup reactions in the target.

Fig. 4.23 shows the spectra of the breakup position calculated for those two scenarios. Especially for the first scenario only the system "DSSD2 - CsI" contributes to the measurement of the breakup point along the z-axis. The finite granularity of the CsI-array as well as the angular straggling discussed in section 4.3.6 limit the resolution of the method. However still a trend can be identified. In Fig. 4.23 (a) the distribution peaks around 10 cm, which is the position of PIN1. Remaining counts around zero indicate that the applied ΔE-condition (breakup reactions in PIN1) is not able to completely suppress events from breakup reactions in the target. The complementary scenario,

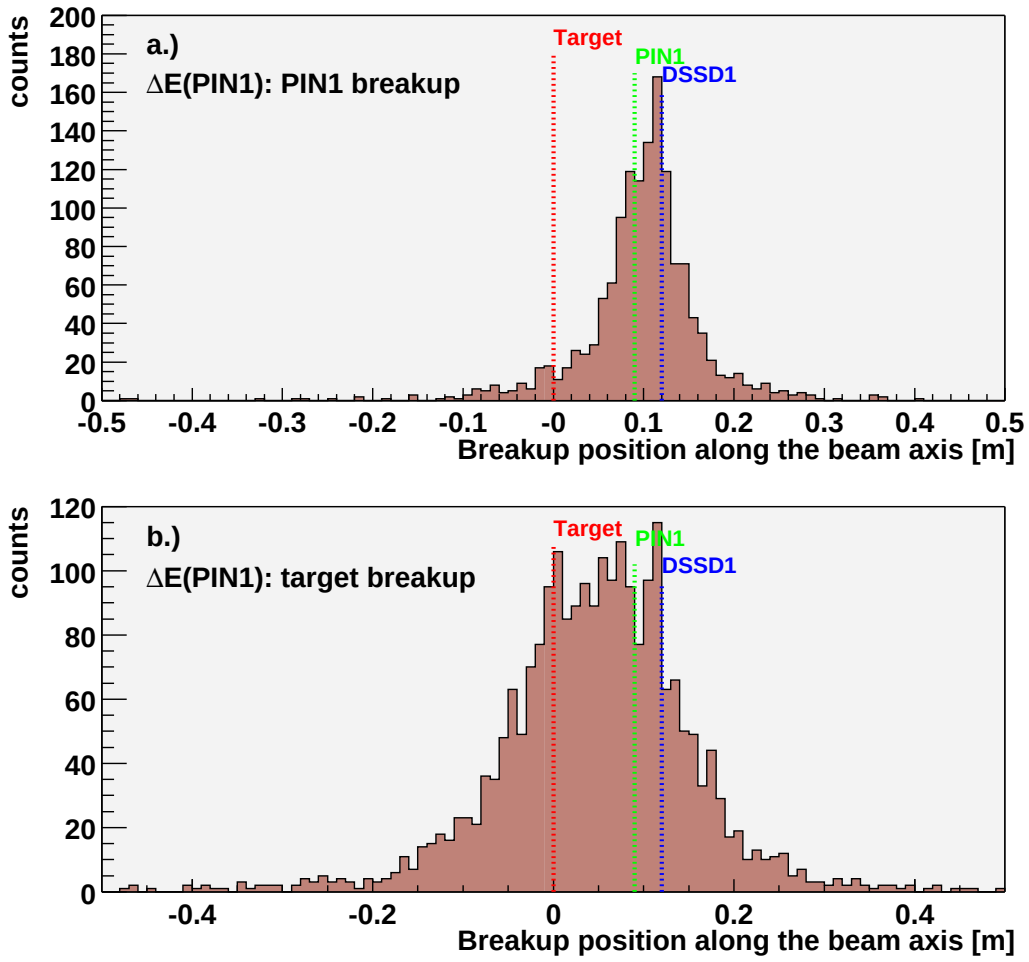

Figure 4.23: The breakup position along the z-axis for the two described cases (see main text). Part (a) shows the spectrum for reactions in the first PIN diode, part (b) for reactions in the target. In both cases contributions from the other reactions scenario are present, since the applied energy loss gate is not an unambiguous condition as shown in Tab. 4.4.

requiring breakup reactions in the target results in the distribution displayed in Fig. 4.23 (b), revealing a broad structure composed of breakup reactions in the target (around 0 cm) and still breakup reactions in PIN1 surviving the gate condition. Even though the resolution was limited, the determination of the axial breakup position still yields valuable information to distinguish valid events from target reactions from background contributions. Ambitious hopes, however, to be able to identify events with a ^{17}Ne decay in flight between the target and the detectors appear unrealistic in view of the limited resolution.

The described method to calculate the breakup position could also serve to estimate the error when averaging over the values of the crossing points of the reconstructed proton trajectories for each coordinate, potentially for each of the three tracking options. This is shown in Fig. 4.24 for the two discussed scenarios. In part (a) one can see that for most of the events (corresponding to breakup reactions in PIN1) the error is of order of at least 10 cm, since for those events only the tracking between the second DSSD and the CsI-array was possible. It is also visible, that a cut on breakup positions larger than 5 cm as indicated by the green dotted line would serve as a selective tool to suppress this background component.

In Fig. 4.24 (b) (which corresponds to breakup reactions in the target) a fraction of events with rather small tracking errors is visible around the target position. Those correspond to events where the tracking between the two DSSD's was possible resulting in a higher accuracy. For the events with larger error bars, where only the tracking with the CsI-array was possible, the two contributions from the target and PIN1 were mixed. But with the information from Fig. 4.24 (a) it seems justified to use the green line at 5 cm as a borderline to distinguish between reactions in the target and in the first PIN diode. However, the most convincing selection criterium can be derived from the two-dimensional distribution shown in Fig. 4.25, which will be described in section 4.3.5.

4.3.4 Comment on the Backtracking

The last two sections 4.3.2 and 4.3.3 might give the impression of an implicit inconsistency. For the determination of the interaction point in the target in section 4.3.2 it was assumed that the breakup occurred in the target, while in section 4.3.3 the breakup point was actually calculated. It should be noted that the breakup position along the beam axis served as an analysis condition to separate those reactions. Obviously the backward tracking as described in section 4.3.2 cannot be used in case of breakup reactions in the PIN diodes. But without valid tracking information for the heavy fragment those events had to be anyway rejected in the offline analysis. Therefore it is no contradiction to use the exact target position along the z-axis for the determination of the interaction point in the target after having shown with the calculation of the breakup position along the z-axis that those events originated from the target.

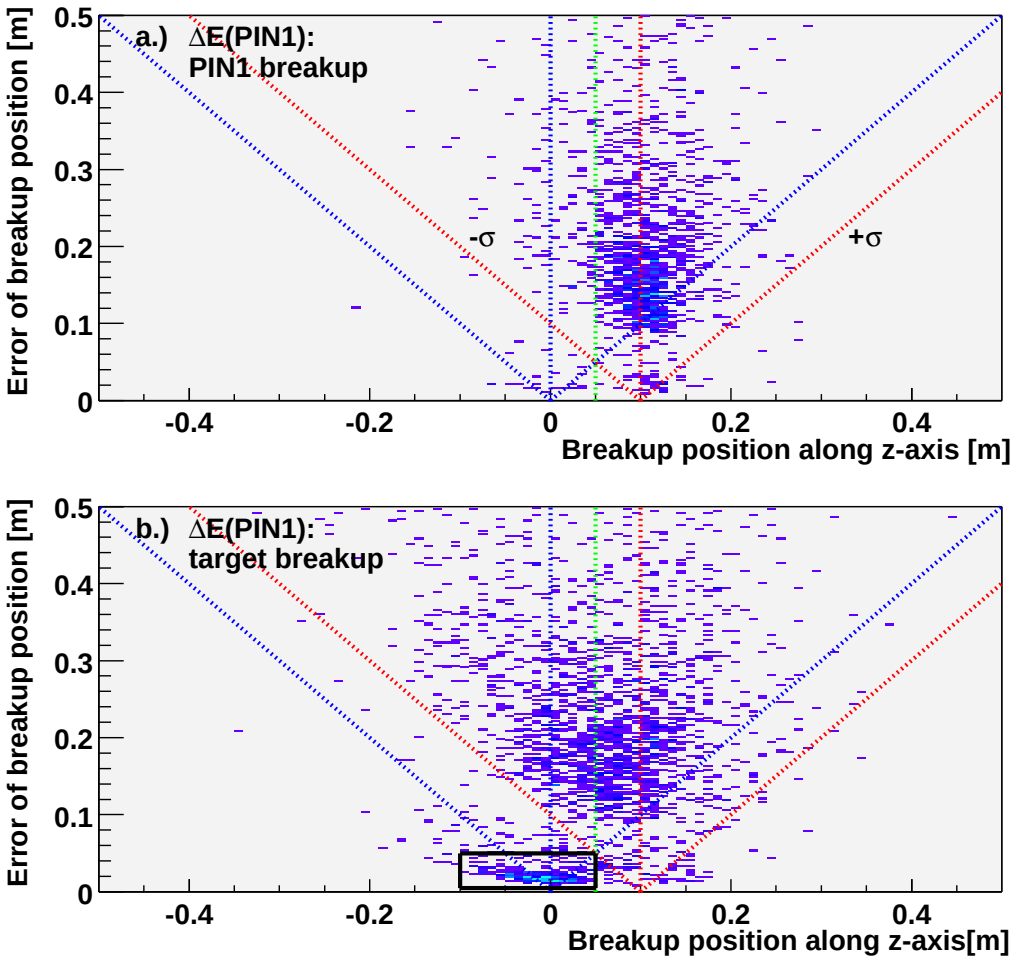

Figure 4.24: Plotted is the uncertainty of the calculated breakup position along the z-axis as a function of the breakup position. The two spectra correspond to the scenarios as described in Fig. 4.23. The vertical lines correspond to the target position (blue), the position of PIN1 (red) and to a suggested cut (green line). The diagonal lines indicated the 1σ limit. The black box in part (b) marks events associated with reactions in target with relatively small error on the position measurement. For those events the tracking information of both DSSD's could be used.

4.3.5 Combination of the ΔE- and the Breakup Position Gates

The discussion of the previous section showed that neither the energy loss nor the breakup position measured along the beam axis could act for themselves

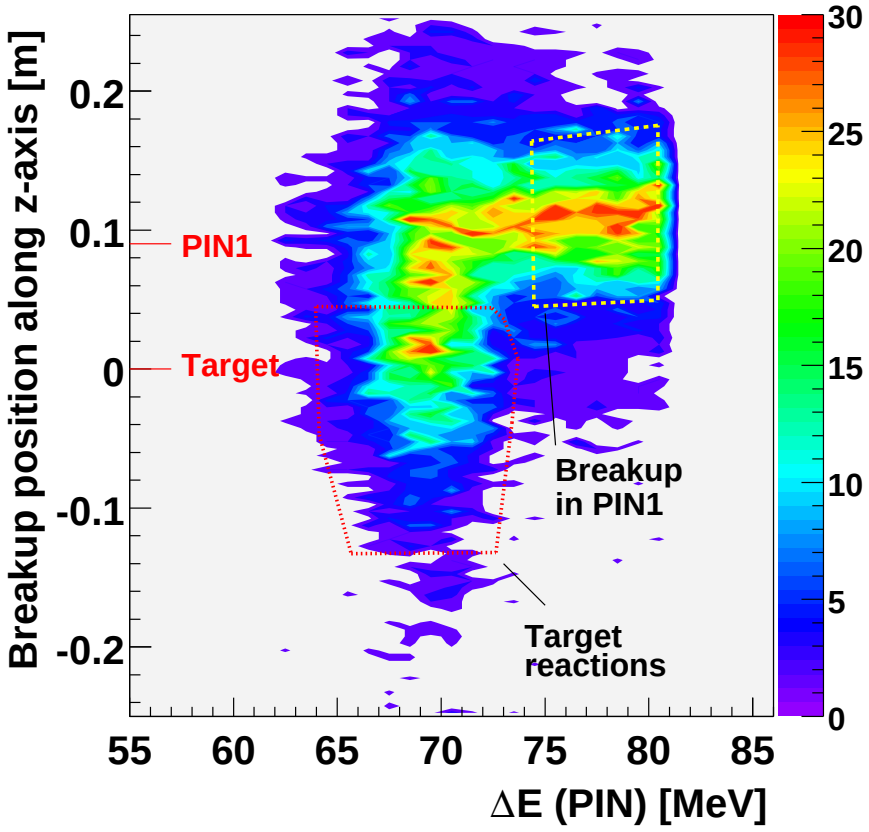

Figure 4.25: Determination of the analysis gate for breakup reactions in the target. Plotted is the measured breakup position along the z-axis versus the energy loss of the heavy fragment in the first PIN diode (limited to 80 MeV for presentation purposes). As discussed in Tab. 4.4 the ranges of the expected energy losses for the two scenarios overlap. An intensity enhancement around the target position (0 cm) and energy loss values corresponding to ^{15}O fragments originating from target reactions can be seen. Two-dimensional conditions for the selection of reactions in the target (red dotted line) and for reactions in PIN1 (yellow dashed line) were derived from this distribution. Due to the use of different tracking methods the distribution of the breakup position is not smooth.

as an efficient condition to isolate reactions in the target. However, their combination leads to a good gate. In Fig. 4.25 the measured breakup position along the z-axis is plotted against the energy loss of the heavy fragment in the first PIN diode. The proton identification was already required for this spectrum. Additionally in all fragment detectors except PIN1, an energy loss signal corresponding to ^{15}O fragments was required. For PIN1 an energy loss between 62 and 80 MeV was required, where events from reactions in the target as well as from reactions in the first PIN diode were expected (see Tab. 4.4).

The spectrum shows that indeed a clear separation of the two reaction scenarios is achievable with a two-dimensional gate condition, represented by the red dotted line for reactions in the target. The distribution of the breakup position shows a discrete structure due to the use of different tracking methods which was also discussed in the context of Fig. 4.24. The yellow dashed line marks reactions associated with breakup reactions in PIN1. The effect of these gates will be discussed in 4.4.2 in the framework of the effort to generate the decay energy spectrum.

4.3.6 Angular Scattering

One of the effects limiting the accuracy of the particle tracking and, accordingly, the resolution in the decay energy spectrum, is multiple Coulomb scattering of the projectile in the target material and the ejectiles in the target and detector materials. In principle, each collision causing scattering is governed by the Rutherford formula.

$$\frac{d\sigma}{d\Omega} = \left(\frac{Z_1 Z_2 e^2}{4E}\right)^2 \frac{1}{\sin^4(\theta/2)} \tag{4.1}$$

Due to its $1/\sin^4(\theta/2)$ dependence, the vast majority of these collisions result in a small angle scattering. Assuming the projectile to be lighter than the target nucleus, which means in turn that the energy transfer is negligible, the particle follows a zick-zack path through the material. The cumulative effect of this small-angle scattering is, however, a net deflection from the original particle direction. Neglecting large-angle scattering events, compared to small-angle deflections ($< 10°$) leads approximately to a Gaussian shape for the scattering probability as described in [Leo94]. In the current experiment the angular scattering of the protons is an effect that has to be considered in the analysis. Using the approximation by Lynch and Dahl [Lyn91, Leo94] the standard deviation σ for the Gaussian distribution of the deflection angle for protons with E=55 MeV penetrating all Si-detectors turns out to be about $\simeq 1.6°$. This translates into a deviation of $\simeq 1.3$ cm at the entrance plane of the CsI-array, a value comparable to the segmentation of the array. Therefore it is rather likely that protons get deflected either in the target or in the Si-detectors leading to a deflection in neighbouring segments of the CsI-array compared to the undeflected trajectory.
However, with the described setup it was possible to identify those events. Using the tracking procedure between the two DSSD's or between the interaction pint on the target measured with the CRDC's and one DSSD, the CsI-crystal could be predicted, which should have been hit by the proton. Whenever the

neighbouring crystal was hit, the deflection angle due to multiple Coulomb scattering was exceeding the opening angle of one CsI-crystal. It should be noted, that it was not possible to localize the origin of the angular straggling. Fig. 4.26 (a) demonstrates the effect of the Coulomb scattering: Plotted is the label-number of the CsI-crystal that actually registered a proton versus the

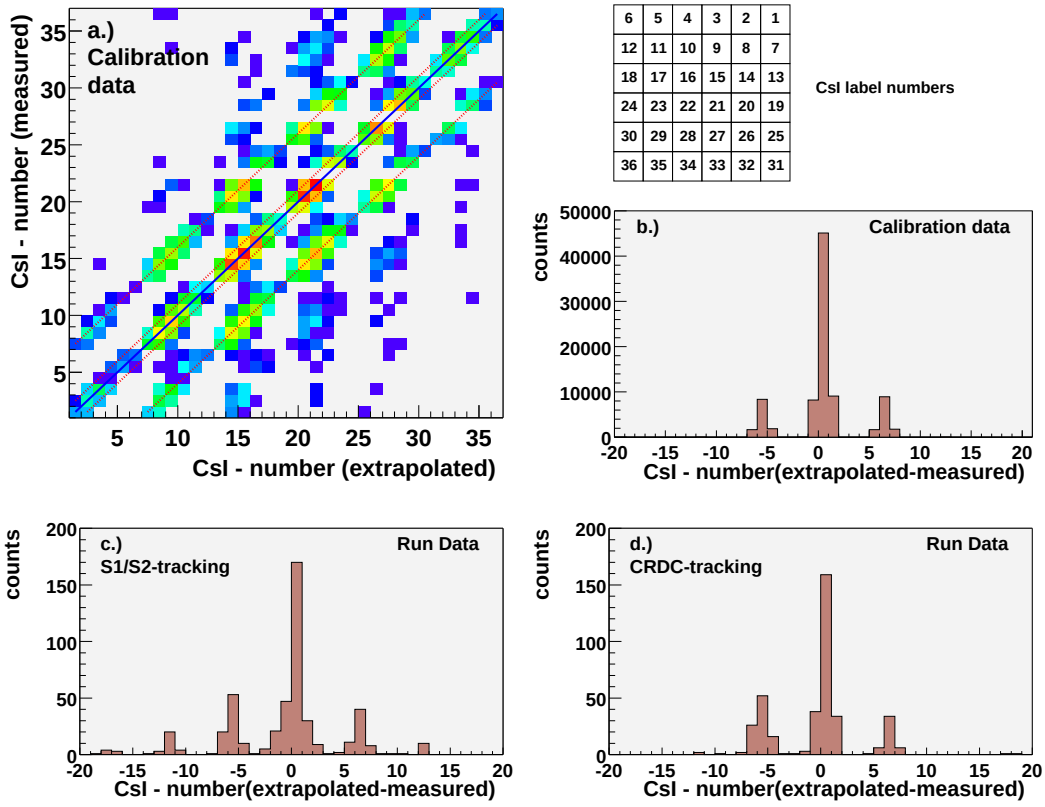

Figure 4.26: Demonstration of the angular scattering effects. Part (a) shows the measured CsI label-number plotted versus the extrapolated value using the two DSSD's and data from the calibration run with a proton energy of 56.65 MeV. The diagonal solid line represents those events in which the proton hits the expected crystal. Those events experienced just small angular scattering effects. The four dashed lines represent events where the proton was scattered in one of the next neighbours. Part (b) shows the difference between the calculated CsI label-numbers. The dashed lines in part (a) correspond here to the differences in the label-numbers of ± 1 and ± 6. The numbering of the CsI-array is illustrated in the upper right insert. Panels (c) and (d) display the same quantities as panel (b), but for data from 2p-events from the main experiment. For panel (c) the CsI label-number was calculated using the position measurements of the two DSSD's (S1/S2-tracking, see section 4.3.2), for (d) the forward tracking with the CRDC's (CRDC-tracking, see section 4.3.1).

number of the CsI-crystal that was expected to be hit. The data were taken from a proton calibration run with a proton energy of 56.65 MeV. The crystals of the CsI-array were labeled as shown in the upper right insert of Fig. 4.26. The events on the diagonal of Fig. 4.26 (a) represents events without scattering. In Fig. 4.26 (b) the difference of the expected and the measured CsI label-number is plotted. According to the labelling scheme of the CsI-array the events with differences of the CsI-numbers of ± 1 and ± 6 correspond to hits in the neighbours to the sides, while values of ± 5 and ± 7 correspond to hits in the diagonal neighbours. More than $\simeq 40\%$ of the protons were scattered in the neighbouring crystals.
For the 2p-events of the main experiment the CsI-crystal that would be hit without angular scattering could be predicted in two ways, either by using the two DSSD's or by using the second DSSD and the interaction point on the target measured by the CRDC's. This can be performed for each proton individually. Fig. 4.26 (c,d) shows the difference between the expected and the measured CsI-crystal label-number analogue to Fig. 4.26 (b). For Fig. 4.26 (c) the position in the CsI-array was calculated using the position information of the DSSD's, for (d) the position information of the second DSSD and the CRDC's was used. Both methods gave similar results and the scattering effect is in the same order of magnitude as for the proton calibration data. Fig. 4.27 proves that the two methods used to determine the difference of the extrapolated and measured CsI-label-number are in good agreement with each other. Rejecting all events in the analysis where scattering into neighbouring detector elements could be observed would have caused an unacceptable loss of statistics. Instead, the scattering information was included in the calculation of the experimental uncertainty of the position measurements. For those events the errors of the position measurements in the proton detectors were doubled. This corresponds to measurements with a pixel size of 2×2 mm^2 for the DSSD's and 3.4×3.4 cm^2 for the CsI-crystals. Since all relevant positions such as the target interaction point or the breakup point along the beam axis were always calculated using the weighed average of the results obtained with the different tracking methods, increasing the error bar as described automatically took care of this effect.

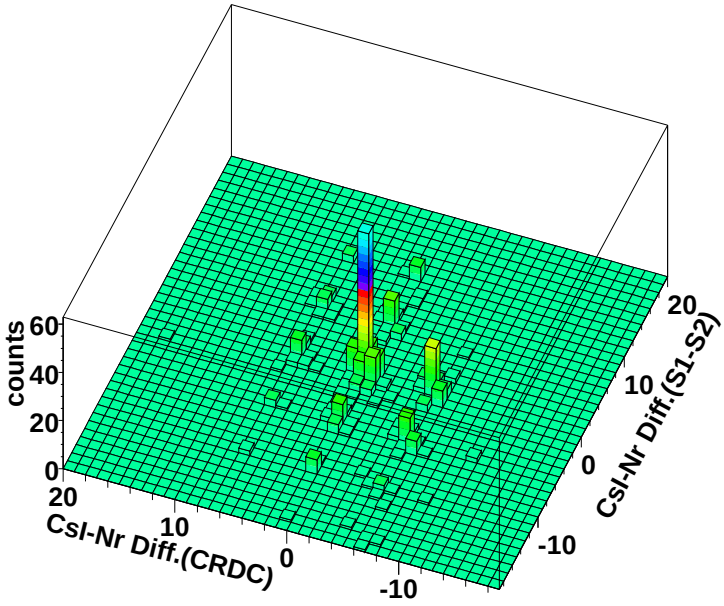

Figure 4.27: Agreement of the identification of straggling events. The two values for the difference of the CsI label-numbers (extrapolated-measured) obtained from two alternative tracking methods plotted individually in 4.26 (c) and (d) have been combined here in to a two-dimensional display The dominant peak at (0,0) proves that the two methods used to detect scattered protons with the backwards tracking between the DSSD's (S1/S2-tracking) and the forward tracking with the CRDC's (CRDC-tracking) are in reasonable agreement.

4.4 Decay Energy Spectrum of ^{17}Ne

In order to answer the question of the existence of a simultaneous 2p-decay of the first excited state in ^{17}Ne and to observe potential sequential 2p-decays from higher-lying states it is necessary to generate the reconstructed decay energy spectrum in the center-of-mass system. The complete measurement of the kinematics properties allowed to calculate the 4-momenta in the laboratory frame. This required to calculate the energy of the protons and ^{15}O fragments at the reaction points, assumed to be in the middle of the target thickness. To correct for the energy loss, ΔE tables from [Jan82, Hub90] were used. In the following the gates applied to generate the reconstructed decay energy spectrum will summarized. The effects of the combination of the ΔE- and the breakup-position gates discussed in section 4.3.5 can be understood by discussing their influence on the decay energy spectrum, especially in context with the results from the previous experiment as displayed in Fig. 2.4. Finally the new decay energy spectrum of ^{17}Ne will be presented.

4.4.1 Summary of Applied Gates

Since the analysis procedure that will finally converge in the decay energy spectrum of ^{17}Ne involves a whole set of analysis filter conditions a compact summary of the conditions will be presented in this section in order to make the analysis more transparent. The following list of filter conditions was applied to the data.

- Identification of the ^{17}Ne projectiles.
  The time-of-flight gates were set individually for each segment of PIN1 and for each of the two trigger types derived from spectra as shown in Fig. 4.10 (a,b).
- Identification of the ^{15}O reaction products.
  For the detectors of the particle telescope the energy loss gates were set according to Tab. 4.4.
- Identification of the protons.
  The 2p-events were identified by requiring the $(\Delta E, E)$ values to lie within the 2p-band discussed in Fig. 4.13 and each of the protons was identified by the single-proton band (Fig. 4.15 (c,d)). In addition about equal energy signals from the front and back side of the second DSSD were required (Fig. 4.15 (a)).

- Hit-multiplicity in the fragment counters.
  In order to assure an undisturbed tracking of the ^{15}O fragments, only events with a multiplicity greater than one in the low gain output of the first DSSD were allowed. The energy threshold for the determination of the multiplicity in the first DSSD was set to 5 MeV. The same threshold was used for the determination of the hit-multiplicity in the segmented PIN diodes. For PIN1 and PIN2 the hit-multiplicity was restricted to one to exclude pile-up events and events where the charge was collected in two segments.

- Hit-multiplicity of proton counters.
  For the identification of the 2p-events a multiplicity of two in the CsI-array was required and a multiplicity of 2 or 4 in the second DSSD. No gates were set on the multiplicity of the high-gain signals from the first DSSD. The lower threshold in the DSSD and the CsI-array was set to 1 MeV and 15 MeV, respectively.

- Tracking gates.
  The measured interaction point on the target had to fit the inner dimensions of the target frame (3.8 cm by 3.8 cm).

After the identification of the reaction channel the measured 4-momenta of the reaction products (^{15}O and two protons) had to be transformed via a Lorentz boost according to [Jac75] into the center-of-mass system, which was defined as the rest system of the total 4-momentum of the reaction products. The 4-momenta were calculated using the measured trajectories and energies of the reaction products normalizing the 4-momenta to fulfill the invariant "length" condition of the energy-momentum 4-vector $p_0^2 - \mathbf{p} \cdot \mathbf{p} = (mc)^2$ (Eq. 11.54 in ref. [Jac75]). The correct matrix for the Lorentz boost was obtained by transferring the total 4-momentum (previously rotated onto the (0,0,1)-axis) into the rest frame using the transformation matrix given by (Eq. 11.95 in ref. [Jac75]). With the individual 4-momenta of the reaction products the same operations (the rotation, transformation and then the inverse rotation) were performed.

4.4.2 Effects of the Reaction Point Gates

Since the possibility to use the reaction point along the beam axis as a filter condition is one of the main features of the improved setup for the present experiment the consequences of applying this filter condition will be discussed.

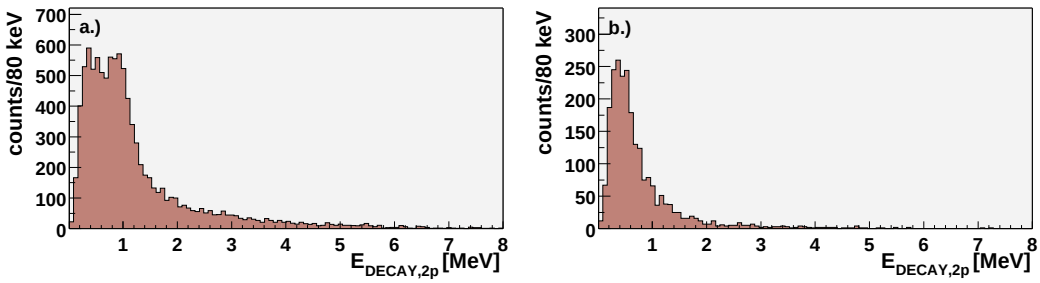

Figure 4.28: Plotted in both spectra is the decay energy of ^{17}Ne with respect to the mass of ^{15}O (g.s.) and 2 protons. Before applying a gate on reactions in the target, two peaks are visible (a). One is around $\simeq$ 300 keV, the other around $\simeq$ 900 keV. Gating on reactions in PIN1 by applying the gate described with Fig. 4.25 leaves only the peak at $\simeq$ 300 keV. Thus it is clearly shown that those counts are associated with breakup events in the detector stack (b).

This leads to an understanding of the nature of the peak at $\simeq$ 300 keV in the decay energy spectrum of the old measurement shown in Fig. 2.4. Fig. 4.28 (a) shows the reconstructed decay energy spectrum which was obtained, by applying no restriction on the reaction point along the z-axis in connection with an energy loss signal in the first PIN diode between 62 MeV and 80 MeV. It should be mentioned that Fig. 4.28 (a) and Fig. 4.25 were produced with identical filter conditions. The key question refers to the consequence of the two-dimensional conditions selecting different breakup positions represented by the red and yellow polygons in Fig. 4.25. In Fig. 4.28 (a) barely two peaks can be identified, one around $\simeq$ 300 keV and another around $\simeq$ 900 keV. The same spectrum is shown in 4.28 (b) gated on breakup reactions in the first PIN diode. This was done by applying the gate represented by the yellow dashed polygon in Fig. 4.25. The peak around $\simeq$ 300 keV remains. This peak is obviously associated with reactions in the detector stack. Fig. 4.29 demonstrates why those events showed up at small decay energies. Suppose the ^{17}Ne projectile passed the target without reacting and subsequently was excited in PIN1 before breaking up. In this case the kinematics is represented by the solid lines. Without identification of the reaction point the analysis code assumed a reaction in the target, thus leading to wrong trajectories with narrower opening angles for the protons, represented by the blue dotted lines. Those smaller opening angles will transform into smaller decay energies when executing the transformation into the center-of-mass system. As a concluding remark to the analysis procedure it can be stated that the decay energy structure around 300 keV, that had already been seen in the previous experiment, where it was interpreted as an indication for a simultaneous 2p-decay, now unambiguously

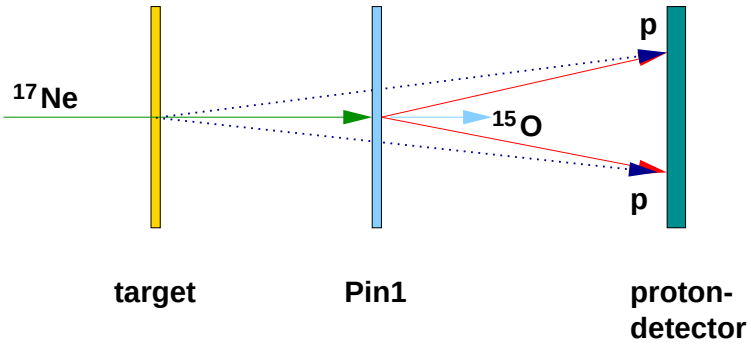

Figure 4.29: Transformation error for breakup reactions in the target. The solid lines represent the kinematics in case of a breakup reaction in the first PIN diode. Assuming a breakup reaction in the target results in the dotted trajectories. When executing the transformation into the center-of-mass system this translates into smaller decay energies.

could be attributed to breakup reactions in the detector material, predominantly in the first PIN diode. It is only due to the significantly improved particle tracking capabilities of the current experiment that this effect could be identified, whereas the previous experiment had no chance to identify and separate this background contribution.

4.4.3 The Decay Energy Spectrum

Selecting reactions in the target by applying a filter condition as described by the red dotted polygon in Fig. 4.25, enables to generate the new decay energy spectrum of ^{17}Ne as shown in Fig. 4.30 (a). Only one prominent peak around $\simeq 900$ keV remains from the originally double-humped structure in Fig. 4.28 (a). This peak is associated with transitions from the $\frac{5}{2}^-$ state in ^{17}Ne ($E^* = 1764$ keV) to the ground state in ^{15}O. Transitions from higher-lying states could not be identified. In the decay energy region around 300 keV, where a potential 2p-decay from the first excited $\frac{3}{2}^-$ state would have been expected, only a few counts remained from the before intense structure. It is likely that these counts originate from the tail of the decay peak around $E_{\mathrm{DECAY}} \simeq 900$ keV, however, remaining background counts from an incomplete removal of contributions from breakup reactions in the detector material cannot be ruled out totally. For further purification an additional filter condition was introduced: in addition to measured breakup positions associated with breakup reactions in the target also a restriction on the error bar obtained for those values was introduced as indicated by the black polygon in Fig. 4.24 (b) (which means the selection of events where the most precise

tracking method could be applied). The corresponding spectrum is shown in Fig. 4.30 (b). With the new strict analysis condition no counts in the region around 300 keV remain. Thus, no evidence for simultaneous 2p-decays from the the $\frac{3}{2}^-$ state in ^{17}Ne was found, which would also have been observed in that energy range. Applying this last strict conditions is reducing the efficiency by a factor of 5.1($\pm$0.4). This was estimated by scaling the number of observed counts in the peak around $\simeq$ 900 keV. Based on this spectrum a limit on the lifetime of the simultaneous 2p-decay of the first excited state in ^{17}Ne will be extracted in section 6.1.
Since the cut applied to produce the spectrum in Fig. 4.24 (b) is reducing the statistics significantly, for further steps in the analysis to interpret the prominent the peak around $\simeq$ 900 keV the spectrum shown in Fig. 4.28 (a) will be used and the simulations presented in the following chapter will refer to this spectrum as well.

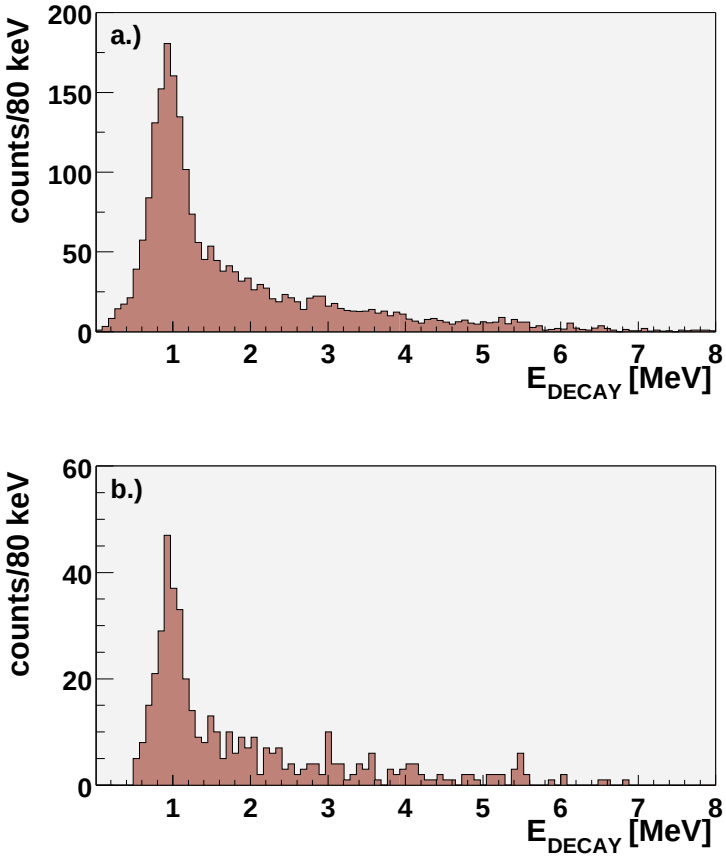

Figure 4.30: The decay energy spectrum of ^{17}Ne from the present experiment. In part (a) the decay energy is plotted with respect to the mass of ^{15}O (g.s.) and two protons. The peak around 900 keV is associated with transitions form the $\frac{5}{2}^-$ state in ^{17}Ne. Part (b) shows the identical property after requiring small error bars on the measured breakup positions along the z-axis (indicated by the black polygon in Fig. 4.24 (b)) as an additional analysis filter condition. No contribution around 300 keV remains. Thus the observed decay energy spectrum is in agreement with the observation of less than one simultaneous 2p-decay from the $\frac{3}{2}^-$ state in ^{17}Ne.

4.4.4 Investigation of the Peak around 900 keV

The peak around 900 keV shown in Fig. 4.30 (a) was further analyzed. In order to extract the measured decay energy and the excitation cross section (leading to the B(E2) values) Monte Carlo simulations were performed, which will be discussed in the following chapter. However the analysis of the events in the measured decay energy spectrum will also allow to identify the sequential nature of the 2p-decays from the $\frac{5}{2}^-$ state in ^{17}Ne. This was done by analyzing the individual proton kinetic energies and their relative kinetic energy in the center-of-mass system. Additionally the opening angle in the center-of-mass system between the protons should show an isotropic distribution for a sequential 2p-decay.

Fig. 4.31 (a,b) depicts the individual decay step energies for events with a decay energy between 620 and 1220 keV. The decay step energy was obtained by adding the decay energy of a individual proton to the corresponding recoil energy. The decay step energies were sorted in a way, that panel (a) contains the larger decay energy and panel (b) the smaller one. With a Gaussian fit values of 609 keV and 301 keV for the individual decay energies of the two protons were obtained. Thus the decay events from the $\frac{5}{2}^-$ state in ^{17}Ne show clear evidence of a sequential 2p-decay. This is confirmed when calculating the difference of the decay step energies. Fig. 4.31 (c) displays this quantity, which peaks around 200 keV with a steep slope to smaller decay energies, while a symmetrical distribution peaking around zero would have been expected for simultaneous 2p-decays, where the individual protons are expected to be emitted with equal energies, as stated already by Goldansky 40 years ago [Gol60]. Fig. 4.31 (d) shows the opening angle of the two protons in the center-of-mass system with the isotropic distribution expected for a sequential decay. In addition, Fig. 4.31 (e) shows the measured Coulomb deflection angle in the center-of-mass system for those events, which will be discussed in section 5.4.3 in the framework of the Coulomb excitation process.

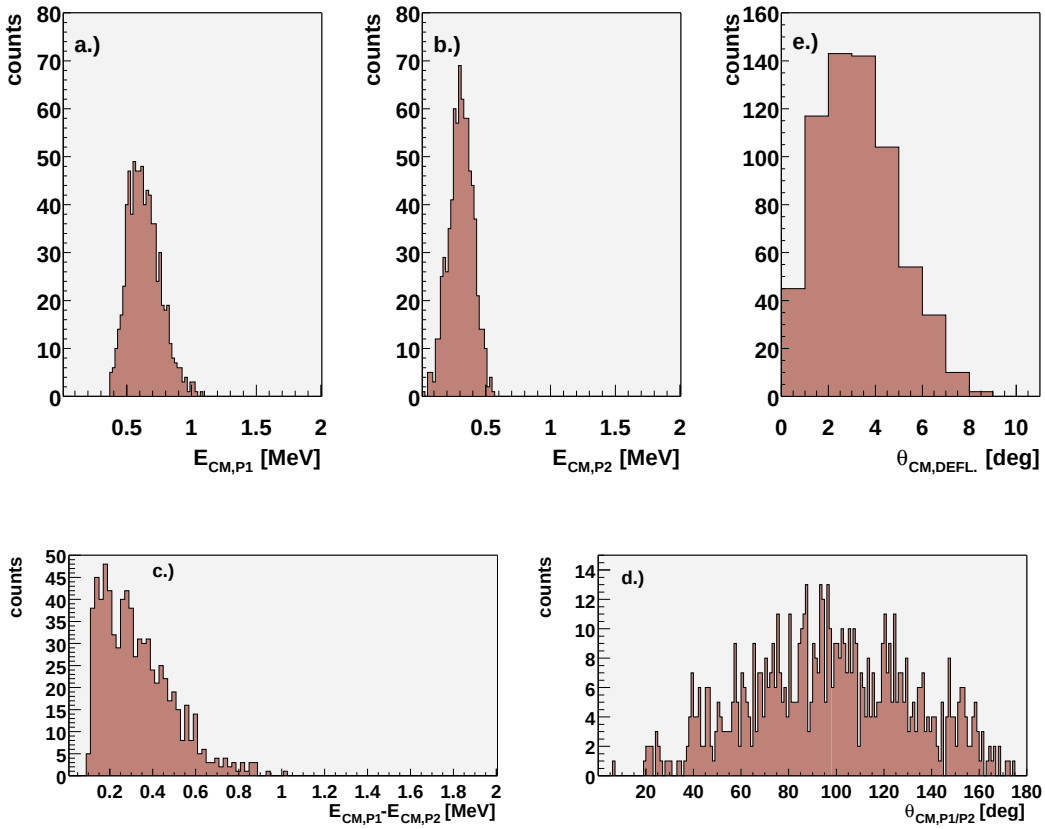

Figure 4.31: Investigation of the decay energy peak around $\simeq$ 900 keV: Panels (a) and (b) show the energies of the two decay steps derived from the individually measured proton energies. Plotted is the decay energy attributed to the emission of each proton corrected for the recoil energy of the fragment. Only events contributing to the peak around $\simeq$900 keV in Fig. 4.30 (a) were included in this analysis step. The left panel (a) shows the energy for the proton with the larger energy, while panel (b) contains the smaller proton decay energies. In part (c) the energy difference of the protons is plotted. Part(d) shows the opening angles of the protons in the center-of-mass system, showing an isotropic distribution characteristic for a sequential 2p-decay. In (e) the measured Coulomb deflection angles for events originating from the peak around $\simeq$ 900 keV is shown, which will discussed in section 5.4.3.

Chapter 5

Simulation of the Results

This chapter describes the Monte Carlo simulation used for the further data analysis. The main purpose of the simulation was the determination of the efficiency of the stacked particle telescope, which was essential for the extraction of the B(E2) values for the $\frac{1}{2}^- \rightarrow \frac{5}{2}^-$ excitation and for the extraction of an upper limit for the lifetime of the simultaneous 2p-decay of the $\frac{3}{2}^-$ state. The simulation was also used to support the analysis procedure as described in the previous chapter. However, the simulation was used to describe only the 2p-decay events originating in the target. It was not within the scope of the simulation to describe other effects such as breakup reactions in the detectors, since those were separated sufficiently by the data analysis filter conditions and therefore could be explained independently. In the following sections the simulation procedure will be described and its performance will be demonstrated by comparing measured and simulated spectra. The final goal is to reproduce the decay energy spectrum shown in Fig. 4.30 (a), to determine the correct decay energy of the $\frac{5}{2}^- \rightarrow \frac{1}{2}^-$ transition together with its detection efficiency and to investigate potential transitions from the first excited state in ^{17}Ne.

5.1 General Description of the PBREAK Code

The Monte Carlo code PBREAK [Chr00] simulates the full detector responses for the reaction of interest: An incoming projectile (^{17}Ne) is Coulomb-excited in the target and breaks up into the heavy fragment ^{15}O and two protons by either a sequential, a simultaneous correlated ("diproton") or a simultaneous uncorrelated ("democratic") decay. Then the particles follow their trajectories

and may be detected in the detector array. While the first part, the reaction mechanism, can be used easily for other reactions, the response of the detector is more or less customized for the described setup. Measured properties, e.g. the beam profile, the energy spread of the beam and the energy resolutions of the different detectors were incorporated into the simulation code.

5.2 Ingredients of the Simulation

The following paragraph describes the key points of the simulation procedure. Structured in three groups dedicated to the properties of the projectiles, the description of the reaction properties and the detection of the reaction products, the main ingredients for the simulations are introduced.

5.2.1 ^{17}Ne

- **Time-of-flight**
  In the analysis, the time-of-flight condition was used only to identify the ^{17}Ne projectiles. In the simulation, every incoming particle was per default ^{17}Ne and thus the value for the time-of-flight condition was chosen in a way to reproduce the situation of the offline analysis.

- **Beam energy**
  The beam energy was adjusted to the momentum spread of $\frac{\Delta P}{P} = 3\%$ present in the experiment, assuming a Gaussian shape of the energy distribution.

- **Beam profile**
  Derived from the drift ellipsoid method described in section 4.3.1 a two-dimensional probability distribution was included into the simulation to obtain a realistic description of the slope and offset parameter of the beam profile.

5.2.2 Reaction in the Target

- **Energy loss**
  The correct energy loss in the target both for projectiles and reaction products was accounted for by assuming a uniform breakup probability

over the target thickness. The energy loss was calculated using the range tables of [Jan82, Hub90].

- **Population of excited states**
  The simulation program was designed to populate one selectable excited state per simulation run. Each ^{17}Ne projectile was excited whenever it hit the target. The width of the excited states was chosen according to [Gui98, Til93, Ajz91].

- **Mechanism of the 2p-decay**
  The simulation code offers three possible decay mechanisms: The simultaneous correlated "diproton" decay, the simultaneous uncorrelated "democratic" decay, treated as a three-body breakup and a sequential decay mode. For all of these types the final state including the width has to be given as input to the simulation; for the sequential decay mode additionally the intermediate state must be described. The decay is treated in the center-of-mass system. After having calculated the complete kinematics in the center-of-mass frame the 4-momenta of all particles are transformed back into the laboratory frame.

- **Angular straggling**
  The angular scattering was simulated for all particles (^{17}Ne projectiles, ^{15}O fragments and the two protons). The average scattering angles were taken from [Lyn91, Leo94] and both, scattering in the ^{197}Au target and scattering in the Si-detectors was taken into account.

- **Coulomb deflection**
  The Coulomb deflection of the projectile in the field of the ^{197}Au target was calculated by deriving a distribution of the Coulomb deflection angles, after exciting states of given excitation energies, using the virtual photon method as described by [Ber88].

5.2.3 Particle Detection

- **Energy loss**
  The energy losses in the detectors were calculated using the range tables of [Jan82, Hub90].

- **Detectors response**
  The detector responses were simulated using their geometric properties together with their energy and position resolutions as measured in the calibration runs.

- **Angular straggling**
  The angular straggling of the particles in the detectors was taken into account in the same way as for the target straggling described earlier.

- **Crosstalk in the first DSSD**
  Whenever a ^{15}O fragment hit the first DSSD a signal amplitude corresponding to 1% of the deposited energy of the fragment was assigned to each of the neighbouring strips. This way the cross-talk observed in the high-gain setting of the first DSSD was simulated.

5.2.4 Generation of the Simulated Data Stream

A event-by-event data stream was generated, with the same structure as the measured data, allowing to use the same analysis routine with the same filter conditions as used for the measured data.

5.3 Simulation Inputs and Performance Tests

The following section compares the measured and the simulated spectra. All spectra for the measured data have been introduced and discussed in the sections of the previous chapter. The aim of this effort is to demonstrate the reliability of the simulation procedure as well as to point out some remaining open questions. Fig. 5.1 (top row) shows the ΔE-E plot as discussed in Fig. 4.11 for the identification of the ^{15}O fragments. In the simulated data only the ^{15}O peaks shows up, since the simulation cannot treat other effects, like breakup in the detectors or non-reacting ^{17}Ne projectiles. The simulation confirms the identification obtained in the data analysis. For the identification of the 2p-events the ΔE_{SUM}(DSSD2) - E_{SUM}(CsI) plot is shown (Fig. 5.1 (middle row)), which was discussed in Fig. 4.13. The same bands can be identified. In addition to the known structures a low-intensity band appears, associated with events where both protons were recorded in the CsI-array but only one of them in DSSD2. These events were not visible in Fig. 4.13 due to the large background. The two spectra in the bottom row of Fig. 5.1 show the correlation of the front and the back signal of the second DSSD (see also Fig. 4.15). It should be noted here, that while simulating the response of the front and the back side of the DSSD, the correlation between the two sides has to be taken into account. Since the front and the back side of a detector segment detect the same particle the number of generated free charge carriers is the same for

both sides. The signals differ only due to effects in the electronics. Therefore the detector response has to be simulated using the same Monte Carlo starting values for the measured energy loss for both sides instead of treating the two sides separately. In a further step the electronics effects were taken into account by smearing out the measured value to reproduce the deviation of the front and back side as shown in Fig. 4.15.

The simulation nicely confirms the interpretation of the structure of the ΔE_{SUM} - E_{SUM} distribution measured with the first DSSD and the CsI-array as discussed in section 4.2.4. This can be shown in the top row of Fig. 5.2. The structure of the bands and their intensities are comparable, however in the experiment additional efficiency losses occurred, e.g. due to occasional crosstalk between the next-but-one neighbouring strips or electronical problems. In the simulation those losses were quantitatively corrected as well. The effects of angular scattering (see section 4.3.6) are also very well reproduced, as can be seen in the middle row of Fig. 5.2. The bottom row of Fig. 5.2 demonstrates the determination of the breakup position along the beam axis. Even though the simulation contains in principle only events which break up in the target, the resulting peak denoting the breakup position is slightly shifted to higher z-values, but is still in reasonable agreement with the measurement. A gate condition on breakup positions less than $\simeq$ 5 cm behind the target decreases the efficiency to detect reactions from the target by about $\simeq$ 40%. This number reproduces the large amount of losses in the peak associated with reactions in the target as it was demonstrated in Fig. 4.28.

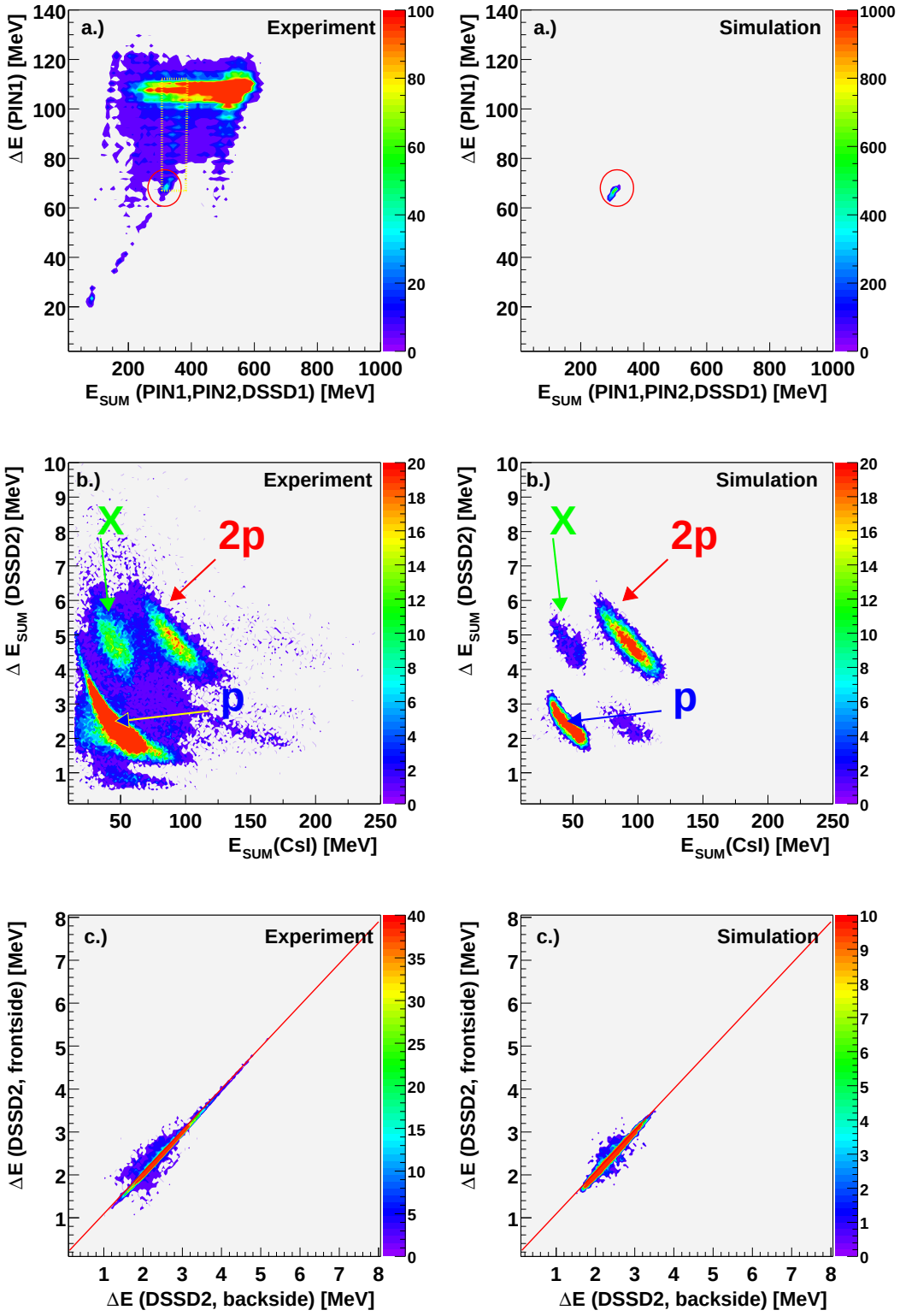

Figure 5.1: Comparison of measured data and simulation results for steps in the particle ID. The left column shows the measured data, the right column the simulated spectra. The identification of the ^{15}O (top row), the identification of the 2p-band (middle row) and the front-to-back correlation of the second DSSD (bottom row) are displayed.

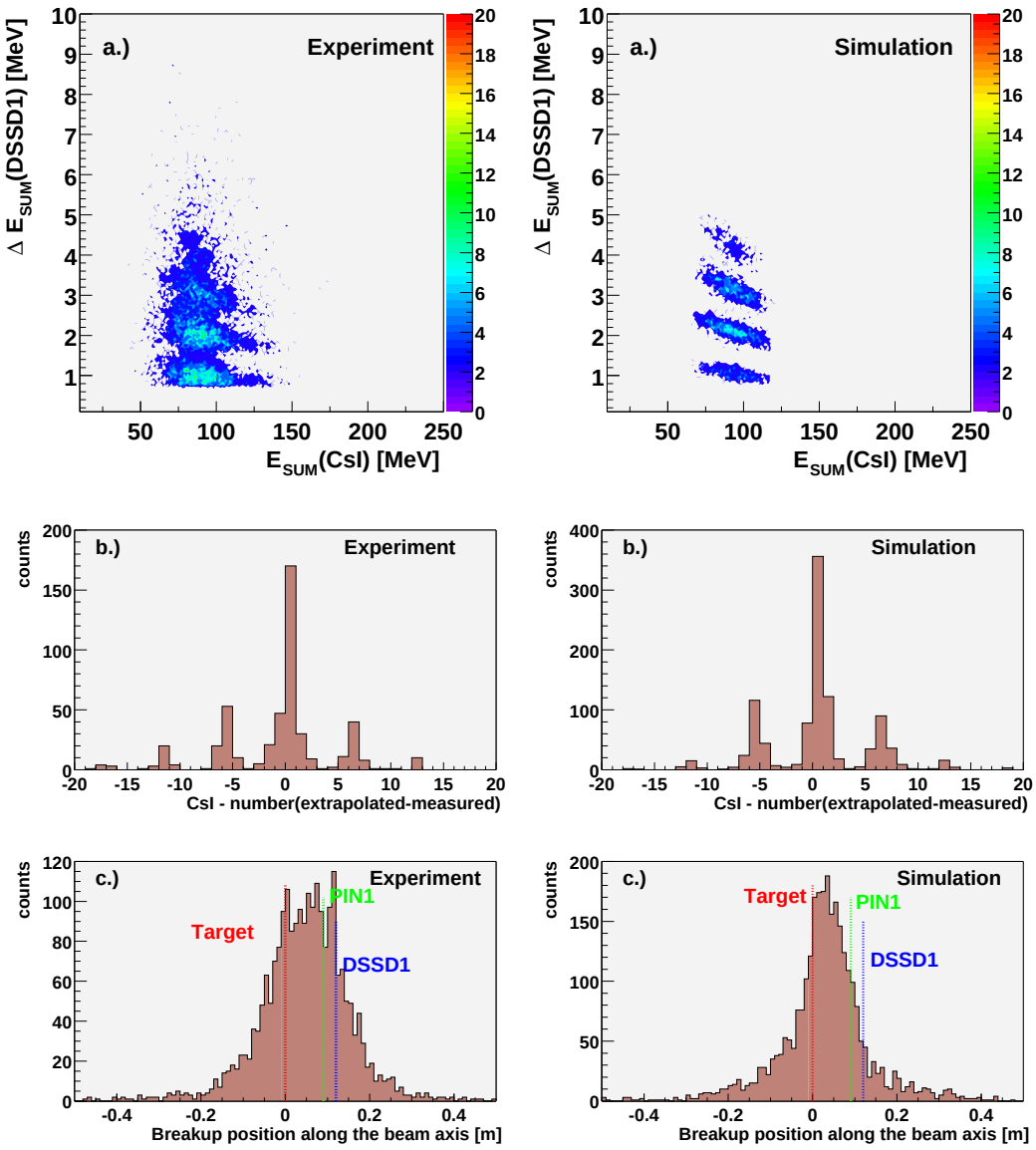

Figure 5.2: Comparison of the measured data and simulation results. The left column shows the measured data, the right column the simulated spectra. The top row shows the observed ΔE_{SUM} - E_{SUM} spectra accumulated with the first DSSD and the CsI-array and gated on the clear identification of 2p-events with the second DSSD as done for Fig. 4.17 (a). The simulation qualitatively explains the effect due to the blocking of strips where crosstalk was identified. The middle row depicts the difference of the extrapolated and the measured CsI label-numbers to illustrate the agreement between observed and simulated angular straggling. The bottom row shows the measured and predicted breakup positions along the z-axis.

5.4 Extraction of Properties for the Calculation of the Cross Sections

In order to calculate the cross sections certain properties have to be extracted from the simulation:

- The decay energy and the number of counts in the peak associated with the 2p-decays from the $\frac{5}{2}^-$ state.
- The upper limit of identified 2p-decays from the $\frac{3}{2}^-$state.
- The energy dependent 2p-detection efficiency.
- The efficiency for detecting events with certain Coulomb deflection angles equivalent to the simulation of the opening angle of the detectors.

5.4.1 The Simulated Decay Energy Spectrum

The simulations can also be used to determine exactly the decay energy of the observed 2p-decay. Aiming to reproduce the structure around $E_{\mathrm{DECAY}} \simeq 900$ keV (i.e. $E^* \simeq 1800$ keV) in Fig. 4.30 (a) the decay energy of the $\frac{5}{2}^-$ state in ^{17}Ne used for the simulation was varied in in steps of 10 keV from a range of 1688 keV to 2048 keV. For the determination of the number of observed counts a more realistic description of the high-energy tail of the structure around $E_{\mathrm{DECAY}} \simeq 900$ keV was needed. Thus, 2p-decays from the $\frac{5}{2}^+$ state at 2651 keV were included. This state can be populated via E3 excitation. The widths for both states in ^{17}Ne were taken from [Gui98]. Then a χ^2-fit was used to fit the simulation to the data in order to reproduce the measured spectrum and to obtain a value for the decay energies for the transitions from the $\frac{5}{2}^-$ state. In Fig. 5.3 the normalized χ^2/N of the resulting fits (only including the $\frac{5}{2}^-$ state and not the $\frac{5}{2}^+$ state) is plotted for different fit ranges. The lower boundary was chosen to be ≥ 320 keV in order to neglect the small contribution from breakup reactions in the Si-detectors still present in Fig. 4.30 (a). A fairly good estimate of the decay energy and its error can be extracted from this plot. For each series of simulated data points the normalized χ^2/N was fitted with a quadratic function of the energy of the $\frac{5}{2}^-$ state in ^{17}Ne. .

$$\chi^2/N = a + b * E_{5/2^-} + c * E_{5/2^-}^2, \tag{5.1}$$

where a,b and c are the fit parameters and $E_{5/2^-}$ the excitation energy of the $\frac{5}{2}^-$state. The minimum of χ^2/N indicates the best value for the excitation energy of the $\frac{5}{2}^-$ state. A clear prescription exists how to derive the error (i.e. the standard deviation σ) from the width of the χ^2/N - parabola, (see [Bev92]).

$$\sigma^2 = 2\left(\frac{\partial^2\chi^2}{\partial E^2_{5/2^-}}\right)^{-1} \tag{5.2}$$

and thus $\sigma^2 = \frac{1}{c}$. Tab. 5.1 summarizes the different values for the excitation energy and the uncertainty of the peak at $E_{\mathrm{DECAY}} \simeq 900$ keV from Fig. 4.30 (a) obtained from the described fit series with the varied fit range.

Simulation Input	Fit range E^* [keV]	MIN (χ^2/N) for E^* [keV]	σ [keV]	Counts	$(\chi^2/N)_{\mathrm{MIN}}$
$\frac{5}{2}^-$	320-1200	1901	70	-	2.06
$\frac{5}{2}^-$	320-1280	1905	57	-	1.92
$\frac{5}{2}^-$	320-1400	1898	44	-	1.84
$\frac{5}{2}^-$	320-2000	1897	41	-	1.89
$\frac{5}{2}^-$	480-1440	1900	44	-	1.08
$\frac{5}{2}^-,\frac{5}{2}^+$	320-1600	1885	56	1242	1.73
$\frac{5}{2}^-,\frac{5}{2}^+$	320-1680	1885	52	1232	1.61
$\frac{5}{2}^-,\frac{5}{2}^+$	320-1760	1873	51	1196	1.91
$\frac{5}{2}^-,\frac{5}{2}^+$	320-1920	1870	51	1180	1.91
$\frac{5}{2}^-,\frac{5}{2}^+$	320-2000	1868	52	1171	1.92
$\frac{5}{2}^-,\frac{5}{2}^+$	320-2240	1861	54	1156	1.95

Table 5.1: The peak position obtained from the χ^2-fits. Two types of fits were performed, one including only decays from the $\frac{5}{2}^-$ state, the other including also decays from the $\frac{5}{2}^+$ state. The fits were repeated for different fit ranges in order to estimate the systematic errors. For the fit series including the two states also the number of observed counts in the peak originating from decays of the $\frac{5}{2}^-$ state are given.

Fig. 5.4 shows again the measured decay energy spectrum as from Fig.4.30 (a) together with the simulated spectrum based on the peak properties derived from the optimum fit discussed above. The simulated spectrum reproduces the peak at an decay energy of 956 $(\pm 44^{\mathrm{stat.}} \pm 16^{\mathrm{syst.}})$ keV , where the statistical error is taken from the best χ^2-fit and the systematical error is derived from the standard deviation of the results for the different fit ranges and methods. The analysis of the fits including the $\frac{5}{2}^+$ state results in an number of

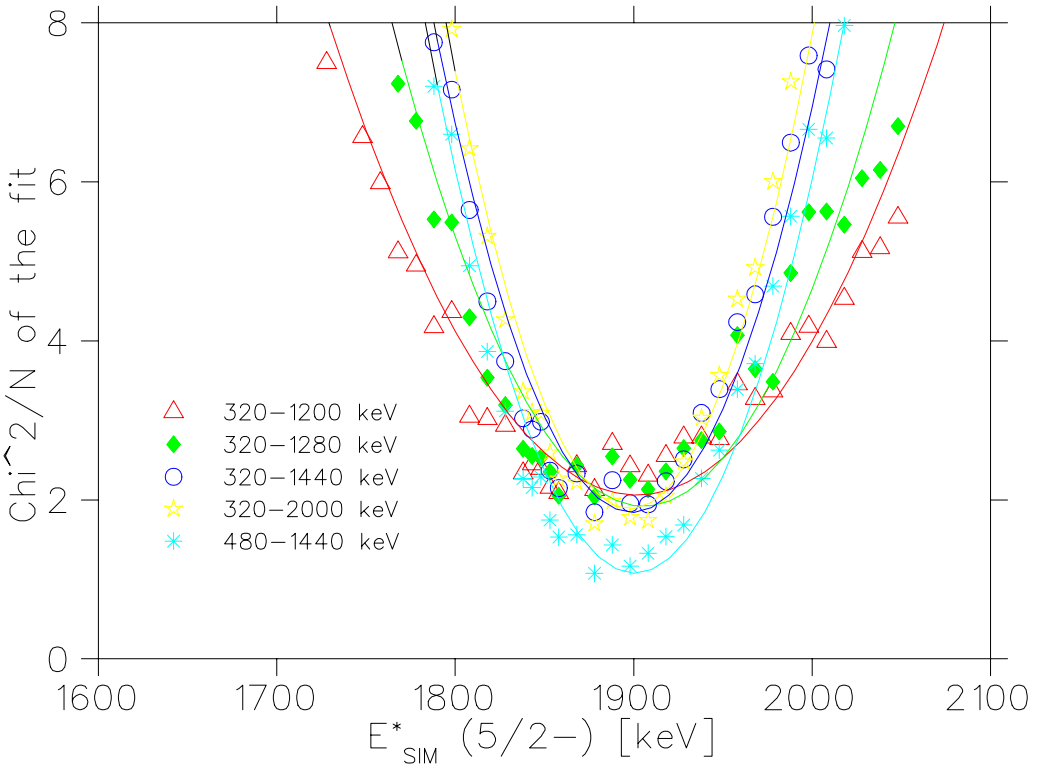

Figure 5.3: Determination of the decay energy via χ^2-fits. Plotted is the the normalized χ^2 as a function of the excitation energy of the $\frac{5}{2}^-$ state, which was used in the simulation for different fit ranges. Here the fit series including only the $\frac{5}{2}^-$ state are shown.

$N_{2p,obs.} = 1196(\pm 35^{stat.} \pm 34^{syst.})$ events in the peak, where the systematical error is derived from the standard deviation of the results for the different fit ranges. The decay energy of 956 ($\pm 44^{stat.} \pm 16^{syst.}$) keV corresponds to an energy of the $\frac{5}{2}^-$ state of 1900($\pm$78) keV, considering in addition to the experimental error of the decay energy from the present experiment also the experimental error of the mass of ^{17}Ne of $\pm$50 keV [Men70, Aud97]. At decay energies around 340 keV the simulation does not account for all of the measured intensity. However, it has been already discussed in the context of Fig. 4.30 (a) and (b) that those counts are associated with breakup reactions in the Si-detectors and do not influence the fit results.

5.4.2 Detection and Analysis Efficiency

In order to extract the experimental efficiency (comprising the detection and analysis efficiency), it was necessary to compare the number of initial ^{17}Ne

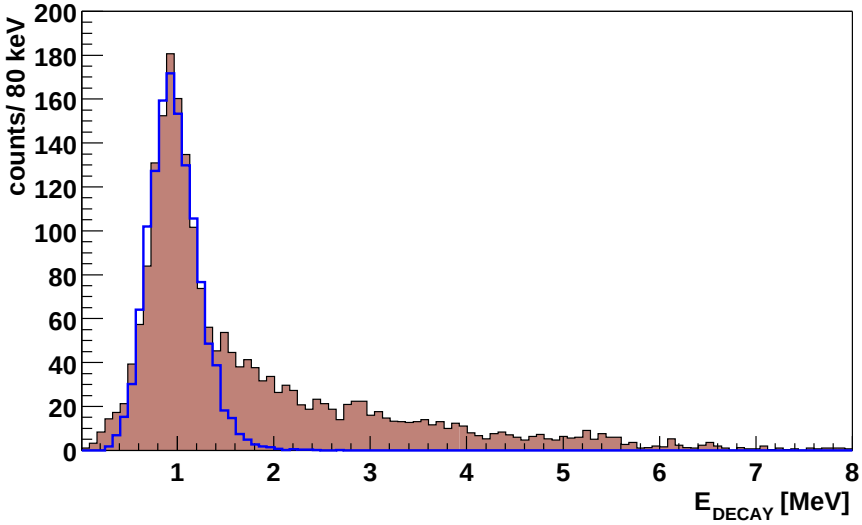

Figure 5.4: The simulated decay energy spectrum represented by the blue line is shown together with the measured spectrum from Fig. 4.30. The simulation reproduces the position and the width of the peak. At small decay energies around $\simeq$ 300 keV the simulation is underestimating the measured data, since those counts correspond to breakup events in the Si-detectors which were not considered in the simulation. For the determination of the peak position only the $\frac{5}{2}^-$ state was included in the simulation.

projectiles with the number of detected two proton decays from the $\frac{5}{2}^-$ state in ^{17}Ne. The following effects that reduce the detection efficiency have to be considered:

- Losses of ^{15}O fragments due to geometrical constraints of the detector setup.
- Losses of protons either due to double hits in the detector segments or due to geometrical constraints of the detectors. Those losses can be quantitatively deduced from the middle row of Fig. 5.1.
- Losses of protons due to the applied filter conditions on the proton-identification. The gate conditions applied to the 2p-band and to the single-proton bands as well as requirements such as correlation between the back- and frontsignal of the DSSD's effect the analysis efficiency.
- Losses of ^{15}O fragments due to gate conditions applied to detect the heavy reaction product.

- Losses due to the gate on the reaction point along the beam axis. This quantitatively significant effect was already discussed in Fig. 5.2.
- Losses due to incomplete charge collection, pile up and split charge collection in the segmented detectors as evaluated in section 4.1.4 reduced the efficiency by a factor of 43.9(±3.1)%.

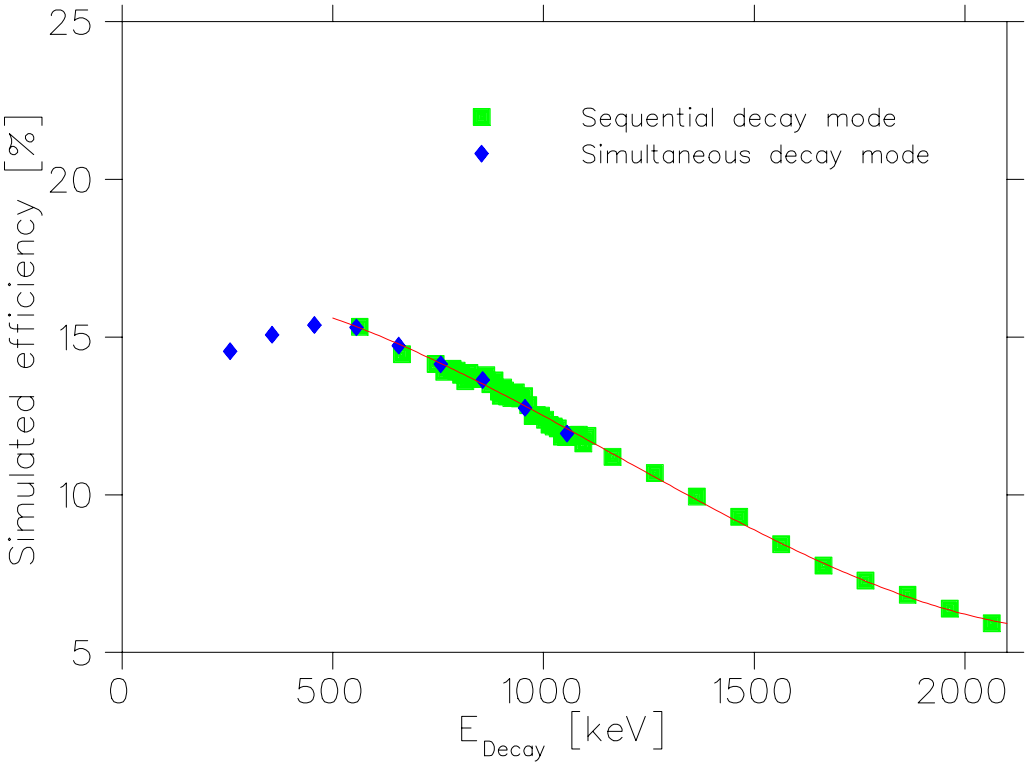

Figure 5.5: Simulated efficiency curve. The simulated efficiency is plotted as a function of the decay energy that entered the simulations. The green squares represent the sequential 2p-decay mode, while the blue diamonds correspond to the simultaneous uncorrelated decay mode. The simulated efficiencies for the sequential 2p-decay were fitted with a third polynomial (red solid line).

Among those effects the geometric losses of the protons and the gate on the reaction point put the most significant constraints of the experimental efficiency. Fig. 5.5 shows the resulting efficiency curve, plotted for both the sequential 2p-decay mode and the simultaneous uncorrelated 2p-decay mode. Obviously the efficiencies calculated in both scenarios are in good agreement. The red line in Fig. 5.5 represents a third order polynomial fit used to describe the efficiency curve for the sequential 2p-decays. The efficiency in the energy region of the $\frac{5}{2}^-$ state ($\simeq$ 900 keV) is 13.0(±0.6)%, while for the decay from the first excited state an efficiency of 15.1(±1.5)% was obtained. Multiplied

with the detection efficiency from Tab. 4.2 of $\epsilon_{\mathrm{DET}} = 43.9(\pm 3.1)\%$ one obtains efficiencies of $\epsilon_{2\mathrm{p},3/2^-} = 6.6(\pm 0.8)\%$ and $\epsilon_{2\mathrm{p},5/2^-} = 5.7(\pm 0.8)\%$ for the decays from the $\frac{3}{2}^-$and the $\frac{5}{2}^-$ states, respectively. Applying the strict analysis condition used to generate the spectrum in Fig. 4.30 (b) reduces the efficiency to detect simultaneous 2p-decays from the $\frac{3}{2}^-$ state to $\epsilon_{2\mathrm{p},3/2^-} = 1.3(\pm 0.2)\%$.

5.4.3 Simulation of the Opening Angle of the Detector

In order to be able to compare the previously measured γ-strength [Chr97] with the observed 2p-strength of this experiment and aiming at the extraction of the excitation cross sections for the higher-lying states it is necessary to ensure that for all cases Coulomb excitation is the dominant excitation mechanism. In typical intermediate energy Coulomb excitation γ-spectroscopy experiments [Sch96, Chr97] it has to be taken care that Coulomb excitation is the dominant process by limiting the opening angle of the projectile detector placed under zero degree relative to the beam. By doing that a limit is put on the maximum Coulomb deflection angle corresponding to a minimum impact parameter. Choosing this value to be significantly larger than the distance of touching spheres for the projectile and the target nucleus reduces the fraction of nuclear excitation to a negligible amount. For the γ-experiment of [Chr97] the opening angle of the detector was $\theta_{Lab} = 4.05°$, corresponding to $\theta_{cm} = 4.41°$.

In the present case, the situation is slightly more complicated since the ^{17}Ne

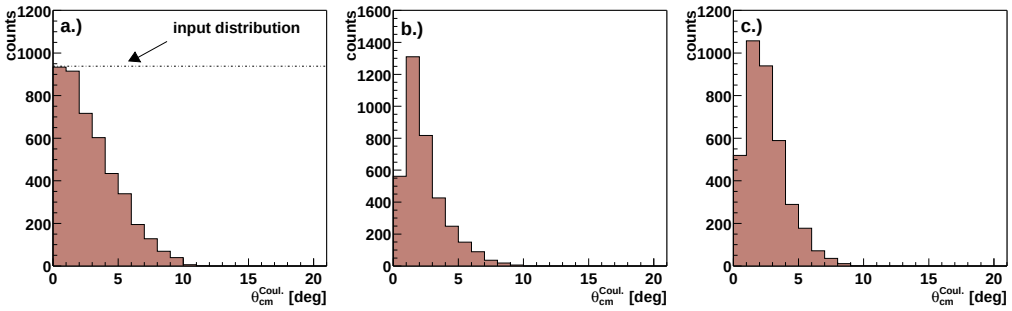

Figure 5.6: Simulation of the Coulomb deflection angle. In part (a) an isotropic distribution was used in order to obtain the efficiency of detecting events with given deflection angles. Part (b) shows the realistic input distribution used for the simulations and part (c) the respective output. The latter one agrees well with the experimental distribution from Fig. 4.31 (e).

breaks up after being excited, which means in turn that the Coulomb deflec-

tion process has to be understood qualitatively and quantitatively. Fig. 5.6 (a) shows the simulated efficiency for detecting a specific Coulomb deflection angle. For this purpose the Monte Carlo simulation was started with an isotropic distribution of the Coulomb deflection angle leaving all the other parameters fixed, e.g. the decay energy. Plotted in Fig. 5.6 (a) is the number of events identified as valid events, as a function of the Coulomb deflection angle in the center-of-mass system, that served as input to the simulation. This distribution can be fitted by the right half of a single Gaussian. Normalized to one at its maximum this function reflects the relative efficiency of detecting events under a given Coulomb deflection angle. The centroid of the Gaussian is $< \theta_{\rm cm}^{\rm Coul.} >= 0.1^\circ \pm 0.3^\circ$ and the width is $3.5^\circ \pm 0.2^\circ$. Hence, the efficiency of detecting deflection angles of $\theta_{\rm cm}^{\rm Coul.} > 6^\circ$, which correspond to impact parameters of smaller than 14 fm (compared to 11.2 fm for the "touching spheres" [Kox84]) is smaller than 25%. Thus Coulomb excitation is the dominant process. Fig. 5.6 (b) shows the realistic $\theta_{\rm cm}^{\rm Coul.}$ input distribution used for the simulations and Fig. 5.6 (c) displays simulated output which is in agreement with the measured Coulomb deflection angle for events originating from the $\frac{5}{2}^-$ state in ^{17}Ne (compared to Fig. 4.31 (e)). With the simulated efficiency curve from Fig. 5.6 (a) it is also possible to calculate quantitatively the number of virtual photons needed to extract the B(E2) values for the excitation of the $\frac{3}{2}^-$ and $\frac{5}{2}^-$ states.

5.4.4 Extracted Excitation Cross Sections

The measured cross section for the 2p-decay of ^{17}Ne is given by

$$\sigma_{exp,2p} = \frac{N_{obs}}{\epsilon_{2p} \cdot N_T \cdot N_{^{17}Ne}} \tag{5.3}$$

with $\mathrm{N}_T = 3.42 \cdot 10^{-6}$ nuclei in the target per fm^2, $\mathrm{N}_{^{17}Ne} = 2.05 \cdot 10^9$ detected ^{17}Ne projectiles. The efficiency for detecting 2p-decays from the $\frac{3}{2}^-$ - and from the $\frac{5}{2}^-$ - state is $\epsilon_{\rm 2p,3/2^-} = 1.3(\pm 0.2)\%$ and $\epsilon_{\rm 2p,5/2^-} = 5.7(\pm 0.8)\%$, respectively. In the peak originating from decays of the $\frac{5}{2}^-$ - state 1196 ($\pm 35^{\rm stat.} \pm 34^{\rm syst.}$) counts were observed, and less than one count from the $\frac{3}{2}^-$ - state. Thus we measure an excitation cross section of $\sigma_{\rm exp,2p,5/2^-} = 29.9(\pm 4.4)$ mbarn for the 2p-decays from the $\frac{5}{2}^-$ state and a limit of
$\sigma_{\rm exp,2p,3/2^-} < 0.011(\pm 0.002)$ mbarn for the simultaneous 2p-decay from the first excited state in ^{17}Ne.

Chapter 6

Extraction and Discussion of the Results

The experimental result at the end of the fourth chapter was the decay energy spectrum of ^{17}Ne. With the simulation developed in the fifth chapter cross sections for the excitations of the $\frac{3}{2}^-$ and the $\frac{5}{2}^-$ states were extracted. These measured cross sections for the 2p-branches and the γ-branch can be used in turn to extract the B(E2) values for their excitation as well as for a lifetime limit for the simultaneous 2p-decay from the $\frac{3}{2}^-$ state. The virtual photon method will be used to obtain those results. However, since competing excitation processes have to be considered as well, this implies some theoretical input for the extraction of the B(E2) values. Taking this into account, the extraction of the B(E2) values will be combined with the theoretical discussion in this chapter.

6.1 Lifetime Limit for the Simultaneous 2p-Decay of the $\frac{3}{2}^-$ State.

From the spectrum in Fig. 4.30 (b) it could be concluded that less than one 2p-transition from the $\frac{3}{2}^-$ state in ^{17}Ne was observed. As discussed above, it is now possible to compare the present experiment with the γ-spectroscopy experiment of Ref. [Chr97] in order to extract an upper limit for the branching ratio $\Gamma_{2p}/\Gamma_\gamma$ for the decay of the $\frac{3}{2}^-$ state. This can be transformed into a lower lifetime limit for the simultaneous 2p-decay of the $\frac{3}{2}^-$ state.

Tab. 6.1 summarizes the ratios of relevant properties for the calculation of the branching ratio $\Gamma_{2p}/\Gamma_\gamma$ from the present 2p-spectroscopy and the previous γ-spectroscopy experiment. The higher counting rate capabilities due to the improved detector segmentation led to an increase of the number of registered ^{17}Ne projectiles compared to the γ-experiment by a factor of 24.9. The target thickness was reduced by a factor of 5 compared to the γ-experiment, in order to optimize the decay energy resolution in the 2p-experiment. Due to the strict analysis conditions applied to obtain the spectrum in Fig. 4.30 (b) the overall detection efficiency of the present experiment was about four times smaller as for the γ-experiment, while the virtual photon number, which determines the excitation process, was increased by about 40% due to the larger effective opening angle of the detector setup. Multiplying the product of the listed factors with the number of observed transitions in the γ-experiment $N^{\gamma}_{\mathrm{Obs.}} = 86(\pm 22)$ leads to the conclusion that ≤ 1 measured simultaneous 2p-decay in the present experiment corresponds to the observation of 148^{+47}_{-60} γ-transitions which would be observable with a γ-detector setup of the same efficiency and opening angle as the actually used particle telescope, where the error includes the uncertainty of the efficiency of both experiments and the statistical error of the observed γ-transitions. Since no counts in the 2p-branch were observed, the upper two-

Property	Factor $\frac{2p}{\gamma}$
1. Number of ^{17}Ne projectiles	24.91
2. Target thickness	0.210
3. Efficiency	0.243
4. Virtual Photons	1.358
Product	1.73

Table 6.1: Comparison of the properties entering the lifetime calculation. Shown is the ratio of those properties between the current 2p- and the previous γ-spectroscopy [Chr97] experiment. The ratio of virtual photons takes the different detector opening angles into account and the value was derived from the virtual photon numbers for the $\frac{1}{2}^- \rightarrow \frac{3}{2}^-$ excitation from Tab. 6.2.

sigma limit for the branching ratio has to be given. For this case, where zero counts from the one branch (the 2p-branch) and n counts from the other (the γ-branch) were observed, the upper two-sigma limit for the branching ratio is given by [Scn96] as:

$$\Gamma_{2p}/\Gamma_\gamma \leq \frac{1-(0.32)^{1/n}}{(0.32)^{1/n}} \tag{6.1}$$

With $n = 148$ it follows that the branching ratio is $\Gamma_{2p}/\Gamma_\gamma \leq 0.0077$ with a confidence level of 68%. Thus, the simultaneous 2p-decay from the $\frac{3}{2}^-$ state in ^{17}Ne is at least a factor of 130 slower compared to the γ-decay, which is

dominated by the M1 decay. With the theoretical value for the lifetime of the $\frac{3}{2}^- \rightarrow \frac{1}{2}^-$ M1 transition in ^{17}Ne of 0.20±0.05 ps (see Tab. 2.1) one can translate the experimental lower limit on the branching ratio into a lower two-sigma limit for the simultaneous 2p-decay of the first excited state of $\tau_{2p} > 26$ ps. As mentioned, this limit was derived from the strictly gated decay energy spectrum shown in Fig. 4.30 (b). However, if the few counts around $\simeq 300$ keV in the less restrictive spectrum in Fig. 4.30 (a) would be interpreted as background from breakup reactions in the detectors and accordingly concluded that already less than one 2p-decay from the first excited state in ^{17}Ne was observed in Fig. 4.30 (a), the lower limit on the lifetime could be increased by a factor of five.

6.2 Extraction of the Experimental B(E2) Values

Transition matrix elements $B(\pi\lambda)$ carry important structure information on the collectivity and deformation of nuclear levels. In order to extract the B(E2) values for the excitation of the $\frac{3}{2}^-$ and the $\frac{5}{2}^-$ states of ^{17}Ne, the virtual photon method was used in the intermediate energy approach by Baur and Bertulani [Ber88]. This approach is similar to the relativistic one, except that the Rutherford-bending of the projectiles trajectory is taken into account. This leads in the present case to $\simeq 5\%$ smaller virtual photon numbers compared to the relativistic approach. The case of ^{17}Ne is discussed in detail in [Chr97, Chr98a]. In the following the main equations will be introduced.

The excitation cross section of a nuclear level via Coulomb excitation can be expressed as the product of the photo-absorption cross section $\sigma_\gamma^{\pi\lambda}$ ($\pi\lambda$ denoting the electrical or magnetic radiation characteristics of multipolarity λ) with the number $n_{\pi\lambda}$ of respective virtual photons. The total excitation cross section $\sigma_{\text{exc.}}$ can be obtained by summing over all allowed transitions [Ber88]:

$$\sigma_{\text{exc.}} = \sum n_{\pi\lambda} \cdot \sigma_\gamma^{\pi\lambda} \tag{6.2}$$

The photon absorption cross section $\sigma_\gamma^{\pi\lambda}$ given by:

$$\sigma_\gamma^{\pi\lambda} = \frac{(2\pi)^3(\lambda+1)}{\lambda[(2\lambda+1)!!]^2} \sum_f \rho_f(\epsilon) k^{2\lambda-1} B(\pi\lambda). \tag{6.3}$$

$\rho_f(\epsilon)$ is the density of final states in the energy region of interest, which in the

present case is taken to be a δ-function at the excitation energy ϵ of the $\frac{3}{2}^-$ and the $\frac{5}{2}^-$ state and k is the wavenumber. Since in the present case the two relevant final states are treated separately, no summation over final states is needed.

6.2.1 Calculation of the Virtual Photon Numbers

In the intermediate energy approach the differential virtual photon numbers are calculated as $dn_{\pi\lambda}/d\Omega$ and have to be integrated over the actual solid angle element $d\Omega$. With $d\Omega = d\sin\theta d\phi$, the integration has to be performed over the Coulomb deflection angles $\theta_{\rm cm}^{\rm Coul.}$, which correspond to the impact parameter. The lower boundary is given by the impact parameter, which is either determined by the distance of touching spheres taken from [Kox84] or by an experimental restriction on the Coulomb deflection angle $\theta_{\rm cm}^{\rm Coul.}$. In the γ-experiment the opening angle of the projectile detector was $\theta_{lab} = 4.05°$ which transforms in the center-of-mass system to $\theta_{cm} = 4.41°$. For the 2p experiment the number of virtual photons per solid angle element had to be folded with the efficiency of detecting events with a given Coulomb deflection angle, as described by the distribution in Fig. 5.6. The virtual photon numbers relevant for the excitation process of the $\frac{3}{3}^-$ and the $\frac{5}{2}^-$ state as well as for the $\frac{1}{2}^+$ state are given in Tab. 6.2.

Experiment	Transition	E^* [keV][Gui98]	$n_{\rm E1}$	$n_{\rm E2}$	$n_{\rm M1}$
2p-spec. (present)	$\frac{1}{2}^- \rightarrow \frac{3}{2}^-$	1288	-	47357	30
2p-spec. (present)	$\frac{1}{2}^- \rightarrow \frac{5}{2}^-$	1764	-	24990	-
2p-spec. (present)	$\frac{1}{2}^- \rightarrow \frac{1}{2}^+$	1908	184	-	-
γ-spec. [Chr97]	$\frac{1}{2}^- \rightarrow \frac{3}{2}^-$	1288	-	34881	20

Table 6.2: Calculated virtual photon numbers for all relevant transitions to be considered for the extraction of the B(E2) values and the lifetime for the simultaneous 2p-decay. The two $n_{\rm E2}$ values for the $\frac{1}{2}^- \rightarrow \frac{3}{2}^-$ excitation were used for the extraction of the lifetime. For the calculation of the virtual photon numbers the energy levels from [Gui98] were used because of their smaller uncertainties.

6.2.2 Excitation Process of the $\frac{3}{2}^-$ State

Obviously, the $\frac{3}{2}^-$ state in ^{17}Ne can be excited via M1 and E2 excitation (see Fig. 6.1). The virtual photon numbers are $n_{\rm M1}$=20 and $n_{\rm E2}$=34881 as listed

in Tab. 6.2. With the average of two B(M1) values obtained with the effective operators from Tab. 2.1 and the error bar deduced by comparing the theoretical prediction and the result for ^{17}N, as discussed in section 2.1.1, a value of B(M1,^{17}Ne,$\frac{1}{2}^- \rightarrow \frac{3}{2}^-$)=0.271(111) μ^2 could be obtained. This leads to an M1 photo absorption cross of section of $\sigma_\gamma^{\mathrm{M1}} = 12.0 \pm 0.49 \cdot 10^{-3}$ mbarn, which finally results in an M1 excitation cross section $\sigma_{\mathrm{exc.,M1}} = 0.24 \pm 0.1$ mbarn. Compared to the measured cross section of $\sigma_{\mathrm{exp},3/2^-} = 11.9^{+3.3}_{-4.5}$ mbarn this contribution is small and thus will be neglected for the calculation of the B(E2) value. With $n_{\mathrm{E2}} = 34881$ Eq. (6.2) leads to $\sigma_\gamma^{\mathrm{E2}} = 3.4^{+1.0}_{-1.3} \times 10^{-4}$ mbarn. Using the energy of the first excited state of 1288 keV Eq. (6.3) results in a B(E2) value of B(E2,^{17}Ne,$\frac{1}{2}^- \rightarrow \frac{3}{2}^-$)= 66^{+18}_{-25} e^{2}fm^4.

6.2.3 Excitation Process of the $\frac{5}{2}^-$ State

The $\frac{1}{2}^- \rightarrow \frac{5}{2}^-$ excitation can proceed only via E2. However, the decay energy peak of Fig. 4.30 that so far was exclusively attributed to decays from the $\frac{5}{2}^-$ state in ^{17}Ne could include a contribution from the decay of the neighbouring $\frac{1}{2}^+$ state (144 keV higher in excitation energy), which can be excited via E1. The resolution in the decay energy spectrum is not sufficient to separate between decays from those two states. Since no experimental data on the B(E1,^{17}Ne, $\frac{1}{2}^- \rightarrow \frac{1}{2}^+$) is available, the upper limit for the B(E1,^{17}N, $\frac{1}{2}^- \rightarrow \frac{1}{2}^+$) $\leq 1.1 \cdot 10^{-4}$ e^2 fm^2 from [Rog74] was used to calculate the excitation cross section. The number of virtual photons can be calculated as n$_{E1}$=184 (see Tab. 6.2). This leads to an excitation cross section $\sigma_{\mathrm{E1}} \leq 0.1$ mbarn, which is negligible. Similar to the B(M1) values of ^{17}Ne and ^{17}N the mirror asymmetry in the B(E1) values for those nuclei is also not expected to be significant [Bro01]. Thus, the experimental limit for ^{17}N can be used for ^{17}Ne as well, and the measured cross section
$\sigma_{\mathrm{exp},5/2^-} = 29.9(\pm 4.4)$ mbarn observed in the peak in Fig. 4.30 can be interpreted as the result of a Coulomb excitation exclusively to the $\frac{5}{2}^-$ state followed by a sequential two proton emission. From the virtual photon number $n_{\mathrm{E2}} = 24990$ a value of
B(E2,^{17}Ne,$\frac{1}{2}^- \rightarrow \frac{5}{2}^-$)= 124(18) e^{2}fm^4 can be derived.

6.3 Discussion

Fig. 6.1 summarizes the measured properties. In the decay energy spectrum shown in Fig. 4.30 (a) a peak was observed corresponding to decays from a state with a level energy of $E^* = 1900(78)$ keV. The width of the measured peak is reproduced by the simulation (see Fig. 5.4) assuming 2p-decays originating from a single state in ^{17}Ne. This state corresponds to the $(\frac{5}{2}^-, \frac{1}{2}^+)$ doublet ob-

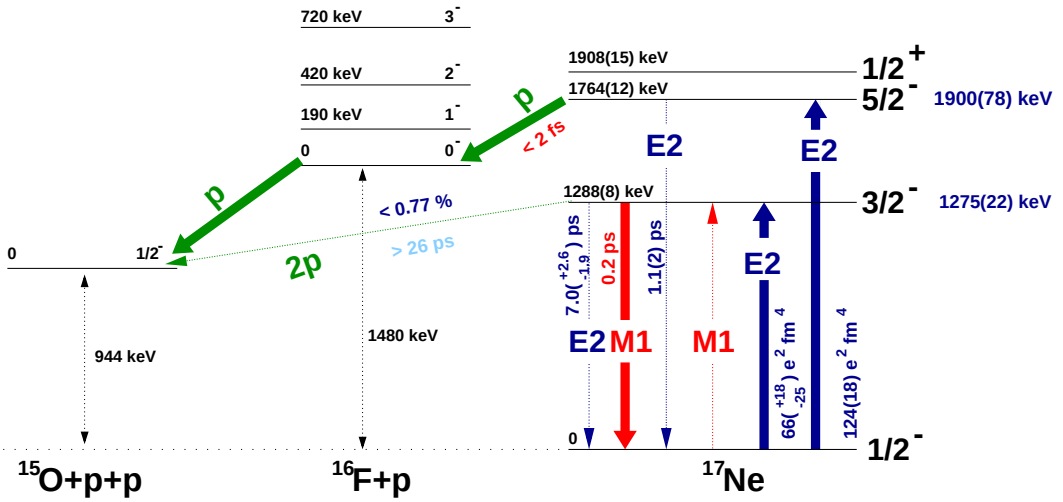

Figure 6.1: Summary of the excitation and deexcitation processes for the lowest excited states in ^{17}Ne. The properties measured in the present work are given in dark blue, the literature values from [Gui98, Ajz91, Til93] in black, theoretical predictions in red and properties extracted by combining measurement and theoretical predictions in light blue.

served by [Gui98] at energies of 1764(12) keV and 1908(15) keV, respectively. In section 6.2.3 it was discussed that contributions of decays from the $\frac{1}{2}^+$ state can be neglected. Thus this state was assigned to be the $\frac{5}{2}^-$ state in ^{17}Ne. The measured value of $E^*(5/2^-) = 1900(78)$ keV differs from the value measured by [Gui98]. The values agree only within the 2σ-limit. One possible source of an systematic error in the present experiment could be an unresolved contribution from decays of the $\frac{1}{2}^+$ state. However, even if the $\frac{1}{2}^+$ state would be populated by a factor of $\simeq 30$ stronger than expected, the peak in Fig. 4.30 (a) would contain only a $\simeq 10\%$ contribution from this state, reducing the value for $E^*(5/2^-)$ only about $\simeq 10 - 20$ keV. Other sources of potential systematic errors are not evident. Thus, the measured level energy in combination with the spin assignment derived here question the spin assignment from the 3n-pickup reaction experiment by [Gui98]. In [Gui98] the $(\frac{5}{2}^-, \frac{1}{2}^+)$ doublet could not be resolved. A peak was measured at $\simeq 1850$ keV with a width indicating about equal contributions from two states. Two states were fitted into the measured

peak at 1764(12) keV and at 1908(15) keV. The uncertainties correspond to the statistical errors obtained by the fit as can be seen by comparing the errors of single states present in the same energy spectrum. The spin assignment by [Gui98] was derived by measurements of the angular distribution and could be confirmed by the IMME calculation presented in Tab. 1.1.
However, careful analysis of the excitation energy spectrum given in [Gui98] shows that the FWHM used to fit the peaks of the $\frac{1}{2}^-$,$\frac{3}{2}^-$,$\frac{5}{2}^-$,$\frac{1}{2}^+$ and the $\frac{5}{2}^+$ states were approximately 180 keV, 195 keV, 195 keV, 225 keV and 250 keV, with their corresponding level energies of 0 keV, 1288 keV, 1764 keV, 1908 keV and 2651 keV, respectively. The experimental energy resolution is given as 180 keV at FWHM. For "some" peaks above the particle threshold slightly broader widths were used [Gui98]. A slightly broader width used to fit the doublet (for example using the same width of 225 keV for both states, or a width similar to the one obtained from the other states above the particle threshold) would bring the two states closer together, resulting in a higher level energy for the $\frac{5}{2}^-$ state and a lower level energy for the $\frac{1}{2}^+$ state. Thus the discrepancy in the $E^*(5/2^-)$ value between the present measurement and [Gui98] could be reduced. In summary, the present experimental results cannot be used to question the level ordering for the ($\frac{5}{2}^-$,$\frac{1}{2}^+$) doublet as derived by [Gui98], especially because this level ordering is supported by the IMME calculations which reproduce also all the other level energies very well. However, the uncertainties given for those level energies by [Gui98] do not take the influence of the widths into account, chosen for the fit of the peak corresponding to the ($\frac{5}{2}^-$,$\frac{1}{2}^+$) doublet.

The decay energy spectrum was further analyzed to extract the B(E2) value for the $\frac{1}{2}^- \rightarrow \frac{5}{2}^-$ excitation of B(E2,^{17}Ne,$\frac{1}{2}^- \rightarrow \frac{5}{2}^-$)= 124(18) e^{2}fm^4. This value was derived assuming the excitation of the $\frac{5}{2}^-$ state at the energy given by [Gui98]. However, it should be noted here that this value would differ by less than 1% even if the spin assignment of the $\frac{5}{2}^-$,$\frac{1}{2}^+$ state by [Gui98] had to be reversed. The energy dependence of the photo absorption cross section $\sigma_\gamma^{\pi\lambda}$ and the energy dependence of the virtual photons numbers nearly compensate each other for that system. The B(E2,^{17}Ne,$\frac{1}{2}^- \rightarrow \frac{5}{2}^-$) will be discussed later in combination with the B(E2,^{17}Ne,$\frac{1}{2}^- \rightarrow \frac{3}{2}^-$) value. From the B(E2,^{17}Ne,$\frac{1}{2}^- \rightarrow \frac{5}{2}^-$) a lifetime for the E2-deexcitation of $\tau_{\mathrm{E2}} = 1.1(2)$ ps can be extracted. Since no evidence for this transition was found in the γ-experiment (see Fig. 2.1), an upper limit for the lifetime of the first decay step of the sequential 2p-decay of the $\frac{5}{2}^-$ state in ^{17}Ne can be extracted. Considering the energetical picture given by [Gui98], the decay of the $\frac{5}{2}^-$ state in ^{17}Ne can only proceed through the 0^- and the 1^- state in ^{16}F. Taking into account that the protons are either in an (sd) or in an (d^2) configuration and considering

parity arguments, the decay through the 1^- state in ^{16}F would be only possible for a proton with $l = 2$. With the Q-value of $Q_p = 94$ keV a simple barrier penetration calculation results in a lifetime of $\simeq 300ps$. Thus the decay of the $\frac{5}{2}^-$ state in ^{17}Ne has to proceed through the 0^- state in ^{16}F by the emission of a proton with $l = 2$. Lifetime calculations give a theoretical value of $\simeq 1.4$ fs for this decay. A decay through the 0^- state in ^{16}F is also in agreement with the measured decay energy of the protons in the center-of-mass system of $\simeq 200$ keV (see Fig. 4.31 (c)) and the single proton energies in the center-of-mass system (Fig. 4.31 (a,b)).

The other measured property derived from the present experiment in combination with the previous γ-experiment [Chr97] is the branching ratio of $\Gamma_{2p}/\Gamma_\gamma \leq 0.0077$ for the two possible decay modes of the $\frac{3}{2}^-$ state in ^{17}Ne, which could be converted in a lifetime limit of $\tau_{2p} > 26$ ps for the simultaneous 2p-decay of the first excited state in ^{17}Ne. This lifetime limit can now be discussed in the framework of the lifetime predictions from the different models as summarized in Tab. 2.2. Even though the experimental lifetime limit is of the same order of magnitude compared to the value of $\tau_{2p,L=0,l=2} = 16$ ps predicted by the diproton model, considering a relative angular momentum between the diproton and the ^{15}O core of $L = 0$ and the angular momentum between the protons of $l = 2$ (see section 1.3.1), it seems rather unlikely that this decay mode was realized in our experiment, keeping in mind that the experimental lifetime limit could well be a factor of 5 larger, as discussed at the end of section 6.1.

The measured lifetime limit is in agreement with all other lifetime predictions which were summarized in Tab. 2.2, namely the diproton decay with a relative angular momentum between the diproton and the ^{15}O core of $L = 2$ and the angular momentum between the protons of $l = 0$ ($\tau_{2p,L=2,l=0} = 411$ ps), the three body decay with $\tau_{3-body} = 470(100)$ ns and the approach for the simultaneous uncorrelated 2p-decay considering the protons being in a d^2-configuration and an (sd)-configuration resulting in $\tau_{uncorr.,(d^2)} = 1.4$ μs and $\tau_{uncorr.,(sd)} = 1.8$ ns, respectively. In order to further investigate the simultaneous 2p-decay of the first excited state in ^{17}Ne it would be necessary to increase the sensitivity towards larger lifetimes by orders of magnitudes. This will require much higher beam currents and newly designed experimental setups, which will be discussed in the outlook. In conclusion, it can be stated that the experimental lower lifetime limit obtained with a significantly improved experimental technique forces to revise the interpretation of the previous 2p-decay experiment [Chr98b, Chr99] and postpones the identification of the simultaneous 2p-decay in ^{17}Ne.

In addition the comparison of the present experiment with [Chr97] allowed to obtain a B(E2) value for the excitation of the first excited state of $B(\mathrm{E2},{}^{17}\mathrm{Ne},\frac{1}{2}^- \rightarrow \frac{3}{2}^-) = 66^{+18}_{-25}$ e^{2}fm^4. These values can be interpreted in the context of calculations within the shell model approach. Those calculations were performed by B.A. Brown [Bro01] and were partly published in [Chr97]. The B(E2) values presently obtained for the excitation of the $\frac{3}{2}^-$ and the $\frac{5}{2}^-$

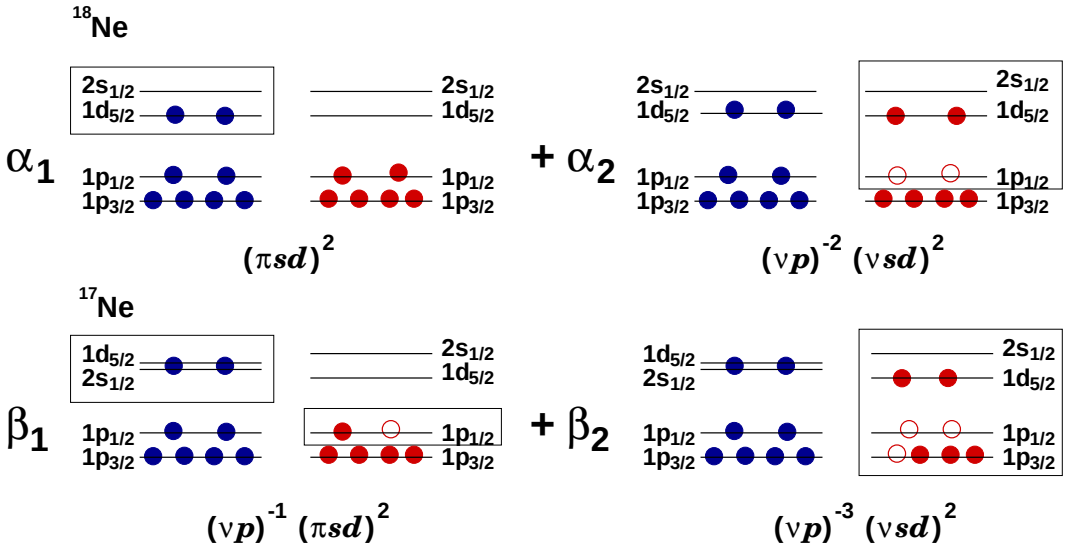

Figure 6.2: Configuration space used in the shell model calculations. The important part of the configuration space is marked by the rectangular boxes. An earlier theoretical approach (second column in Tab. 6.3) took only the left part into account ($\alpha_2 = 0, \beta_2 = 0$), while recent calculations (third column in Tab. 6.3) also acknowledge the importance of the right-hand side including the assumption that $\alpha_2 \gg \beta_2$ ($\alpha_2 \simeq 40\%$, $\beta_2 \simeq 10\%$). For ^{17}Ne the level-crossing of the $s_{1/2}$- and the $d_{5/2}$-shells [Tan95] is taken into account.

state are over-estimated by the earlier calculated values from [Chr97] (listed in the second column of Tab. 6.3). In that paper the B(E2) values in ^{18}Ne and ^{17}Ne were discussed in a configuration space of $(\pi sd)^2$ for the ^{18}Ne and $(\nu p)^{-1}(\pi sd)^2$ for ^{17}Ne. The configuration space is illustrated in Fig. 6.2. The results obtained with the WBP interaction [War92] are close to those expected in the weak coupling of a $p_{1/2}$ neutron hole to the states in ^{18}Ne. In the weak coupling approach (described in detail in [Boh98]) the momentum J of the proton hole is coupled to a vibrational excitation with the angular momentum R giving rise to a multiplet of states with total angular momentum I:

$$I = |J - R|, |J - R| + 1, ...J + R \tag{6.4}$$

In the limit of weak coupling, the various nuclear moments can be expressed as a sum of contributions from the vibrational and intrinsic degrees of freedom. In

the weak coupling situation, only the vibrational moment contributes to such transitions and the $B(\mathrm{E}\lambda)$ value is directly related to the vibrational transition rate:

$$B(E\lambda; RJI \rightarrow R'JI') = (2I'+1)(2R+1) \begin{Bmatrix} R & J & I \\ I' & \lambda & R' \end{Bmatrix}^2 B(E\lambda; R \rightarrow R') \quad (6.5)$$

The sum of the transition probabilities to the different members I' of the final multiplet is equal to $B(E\lambda; R \rightarrow R')$ [Boh98]. In the present case the $p_{1/2}$ neutron hole is coupled to the collective $0^+ \rightarrow 2^+$ excitation in ^{18}Ne. With $R = 0$, $R' = 2$, $J = \frac{1}{2}$, $\lambda = 2$, $I = \frac{1}{2}$ and I'=$\frac{3}{2}$ or I'=$\frac{5}{2}$ for the $\frac{3}{2}^-$ and the $\frac{5}{2}^-$ state, respectively, the weak-coupling relationship for the B(E2) values in ^{17}Ne and ^{18}Ne can be obtained from Eq. (6.5):

$$B(\mathrm{E2},^{18}\mathrm{Ne}, 0^+ \rightarrow 2^+) = B(\mathrm{E2},^{17}\mathrm{Ne}, \frac{1}{2}^- \rightarrow \frac{3}{2}^-) + B(\mathrm{E2},^{17}\mathrm{Ne}, \frac{1}{2}^- \rightarrow \frac{5}{2}^-), \quad (6.6)$$

where the B(E2) values to the $\frac{3}{3}^-$ and the $\frac{5}{2}^-$ states are in the ratio 2:3 [Chr97]. Thus ^{17}Ne could be interpreted in terms of the known B(E2) value from ^{18}Ne. Using a Woods-Saxon potential it was also demonstrated in [Chr97] that the smaller single-particle separation energies in ^{17}Ne compared to those in ^{18}Ne led to about a 50% increase in the B(E2) values in ^{17}Ne, compared to the B(E2) values expected in the oscillator model. The results obtained in the above described model space using Woods-Saxon single-particle wave functions [Chr97] are given in the second column of Tab. 6.3. They were deduced with effective charges of $e_p = 1.50$ and $e_n = 0.65$ chosen to reproduce the ^{18}Ne B(E2) value. In addition the corresponding picture in the mirror system (^{17}Ne and ^{18}O) is listed. The predicted B(E2) values for ^{17}Ne were about a factor of two larger than the values obtained in the present experiment, and the B(E2) values for ^{17}N were almost an order of magnitude larger compared to the experiment.

The earlier shell model approach disregarded the fact that the 0^+ and 2^+ states in ^{18}Ne have large admixtures ($\alpha_2 \simeq 40\%$, see Fig. 6.2) of $(\nu p)^{-2}(\nu sd)^2(\pi sd)^2$ configurations which have a strong influence on the B(E2) values [Bro77]. The rather large effective charges required in the earlier calculations were related to the influence of these core-excited configurations [Bro77].
The potential admixture of $(\nu p)^{-3}(\nu sd)^2(\pi sd)^2$ in ^{17}Ne may not be that important ($\beta_2 \simeq 10\%$, see Fig. 6.2), since the third neutron-hole had to go into the lower-lying $p_{3/2}$ orbital (the respective discussion for ^{18}O and ^{17}N follows an analogue pattern except that the role of protons and neutrons is

reversed). The difference of the influence of the $(\nu p)^{-2}(\nu sd)^2(\pi sd)^2$ and the $(\nu p)^{-3}(\nu sd)^2(\pi sd)^2$ admixtures for ^{18}Ne and ^{17}Ne, respectively, shows up in the disagreement of the present experimental B(E2) values with the theoretical values listed in the second column in Tab. 6.3. Together with the discrepancy in the mirror system this can be interpreted as a breakdown of the weak-coupling model applied to the restricted configuration space illustrated in the left half of Fig. 6.2.
To estimate this effect, the full $(p_{1/2}, d_{5/2}, s_{1/2})^n$ model space was used in more recent calculations with the REWIL Hamiltonian (the F interaction in Ref. [Mcg73] which allowed to incorporate the core-excited configurations).
This new theoretical approach resulted in the values listed in the third column of Tab. 6.3. For these calculations effective charges of e_p=1.40 and e_n=0.40 are chosen to reproduce the A=18 values within the experimental uncertainty. Considering an error for the theoretical values of about $\simeq$ 20% due to model dependencies and due to the experimental uncertainty of the B(E2) value for ^{18}Ne [Chr97], the A=17 values are now in better agreement with the experimental results. These calculations are not as complete as one would like (the $p_{3/2}$ and $d_{3/2}$ orbits are still missing) and an improved model would be desirable. It should be noted that the equation for the B(E2) values (Eq. (6.6)) derived from the weak coupling model is still fulfilled by the new theoretical values and is also in agreement with the experimental values.

This discussion illustrates the limitations of the weak coupling approach in cases where the configuration space used is not able to describe the structure of all nuclei involved in the calculation, stressing the necessity of a careful consideration of the configuration space before applying this approach.

transition	earlier theory e^2fm^4	recent theory e^2fm^4	experiment e^2fm^4	Reference
B(E2,^{18}Ne,$0^+ \rightarrow 2^+$)	256	256	266(25)	[Ram87]
B(E2,^{17}Ne,$\frac{1}{2}^- \rightarrow \frac{3}{2}^-$)	151	105	66^{+18}_{-25}	this work
B(E2,^{17}Ne,$\frac{1}{2}^- \rightarrow \frac{5}{2}^-$)	235	155	124(18)	this work
B(E2,^{18}O,$0^+ \rightarrow 2^+$)	46	46	45(2)	[Ram87]
B(E2,^{17}N,$\frac{1}{2}^- \rightarrow \frac{3}{2}^-$)	33	7.1		
B(E2,^{17}N,$\frac{1}{2}^- \rightarrow \frac{5}{2}^-$)	42	10.3	6.7(1.2)	[Til93]

Table 6.3: Comparison of calculated and experimental B(E2) values. The calculated values are given for two theoretical approaches for shell model calculations using different configuration spaces. The theoretical values for ^{17}Ne in the second column are published in [Chr97], all the other theoretical values are calculated by B.A. Brown [Bro01].

Chapter 7

Outlook

Based on the results of the present investigations this chapter contains some ideas about perspectives for 2p-spectroscopy studies. The use of the 2p-spectroscopy as a spectroscopic tool to study nuclei near or beyond the proton dripline will be discussed. The study of those nuclei and other future candidates for the simultaneous 2p-decay such as ^{48}Ni brings up new experimental challenges depending on the lifetime of the 2p-decay.

7.1 New Goals for Two Proton Spectroscopy Experiments

So far all 2p-spectroscopy experiments were performed with the primary intention to observe a simultaneous 2p-emission. And also all experiments where so far evidence for that decay mode was obtained motivated follow-up experiments in order to understand the nature of the observed transitions. The present experiment adds to this together with the examples discussed in the introduction. Even the first observation of a simultaneous 2p-emission from a resonance in ^{18}Ne will hopefully be confirmed in follow-up experiments. However, in all other examples the experiments revealed interesting information, e.g. the mass of the ground state in ^{11}N, new states in ^{30}S and in ^{31}Ar and in the present case the B(E2) values of ^{17}Ne. Thus the 2p-spectroscopy offers many possibilities besides the proof of Goldansky's postulate [Gol60]. The current generation of radioactive beam facilities gives already access to many nuclei near and beyond the proton dripline. The next generation (e.g. the Coupled Cyclotron Project at the NSCL [Mor97]) and future generations (e.g.

the Rare Isotope Accelerator, planed in the US [Ria00]) will give access to even heavier nuclei beyond the proton dripline. Proton- and 2p-spectroscopy will be among the primary tools to study those nuclei.
Besides testing various nuclear models on extreme range of the isospin degree of freedom the main interest will be the investigation of the astrophysical rp-process. The rp-process together with the hot CNO cycle have been proposed as the dominant nucleosynthesis process in explosive hydrogen burning, which takes place most notably in cataclysmic binary systems, such as novae and x-ray bursts [Ria00].

The nucleosynthesis time scale τ_{tot} depends on the sum of the individual reaction and delay times τ_i (see ref. [Goe95]),

$$\tau_{tot} = \sum_i \tau^i = \sum_i [\tau^i_\beta + (Y_\mathrm{p}\rho N_A \langle\sigma\nu\rangle_{\mathrm{p}i})^{-1}] \tag{7.1}$$

with τ^i_β as the lifetime of the β^+-decay, Y_p indicating the hydrogen abundance, ρ the stellar density,N_A the Avogadro constant and $\langle\sigma\nu\rangle_{\mathrm{p}i}$ the cross section for the proton absorption. Eq. (7.1) illustrates that two processes play a role in the rp-process. The first term stands for the β-decay time scale τ^i_β and the second term for the effective proton capture time scale. The latter depends on astrophysical parameters such as the hydrogen abundance Y_p and on the stellar density ρ and on the reaction cross section $\langle\sigma\nu\rangle$, where σ and ν stand for all possible reactions that could play a role, e.g. for the proton capture cross section $\langle p\gamma\rangle$. The reaction cross sections and the β-decay time scale are the ingredients that have to be delivered by nuclear physics. The main obstacles for a continuous reaction flow between the CNO - and the FeNi-mass region are the waiting point nuclei ^{15}O ($T_{1/2}$=122 s), ^{18}Ne ($T_{1/2}$=1.67 s) and ^{38}Ca ($T_{1/2}$=0.44 s). The compound nuclei ^{16}F, ^{19}Na and ^{39}Sc, formed by proton captures of these waiting point isotopes are particle unbound. This implies that the nucleosynthesis proceeding from ^{15}O, ^{18}Ne and ^{38}Ca to heavier nuclei has to wait for their β^+ decays. At high temperature and density conditions, however, these "waiting points" can be bridged by α-induced reactions and the rp-process turns into an αp-process. As an alternative reaction to the (α,γ)-capture process the 2p-capture is possibly also capable to bridge the waiting points, because the product isotopes ^{17}Ne,^{20}Mg and ^{40}Ti are particle stable with short lifetimes compared to those of the waiting points. Thus, the two-proton capture could reduce the time-scale of the nucleosynthesis. Since it is not feasible to study the (2p,γ) reaction directly, the inverse (γ,2p) reaction (i.e. Coulomb breakup reactions) could be used instead to study those nuclei.

The ^{15}O (2p,γ) ^{17}Ne-reaction in particular has been pointed out as possible break-out from the hot CNO cycle [Goe95]. The CNO cycle is a hydrogen burning process important at temperatures above 1.5×10^7 K. In this reaction

chain the ^{12}C serves as a catalyst while hydrogen is burned to helium:

$$^{12}\mathrm{C}+\mathrm{p} \rightarrow {}^{13}\mathrm{N} + \gamma \rightarrow_{\beta} {}^{13}\mathrm{C};$$
$$^{13}\mathrm{C}+\mathrm{p} \rightarrow {}^{14}\mathrm{N} + \gamma;$$
$$^{14}\mathrm{N}+\mathrm{p} \rightarrow {}^{15}\mathrm{O} + \gamma \rightarrow_{\beta} {}^{15}\mathrm{N};$$
$$^{15}\mathrm{N}+\mathrm{p} \rightarrow {}^{12}\mathrm{C} + {}^{4}\mathrm{He}.$$

The question, however, is how this process is linked to the rp-process. At high temperatures and densities the ^{15}O(α,γ)^{19}Ne reaction begins to dominate the β-decay of ^{15}O to ^{15}N. The ^{15}O (2p,γ) ^{17}Ne reaction could in principle compete with the ^{15}O(α,γ)^{19}Ne reaction to be a break-out process. Those astrophysical reactions are very sensitive to the energy levels of the involved nuclei, in this case ^{17}Ne. In [Chr99] it was demonstrated how the knowledge of the level scheme of ^{17}Ne provided by [Gui95, Gui98] changed the calculations by [Goe95], which before were based on the levels taken from the mirror nucleus. But still the ^{15}O(α,γ)^{19}Ne reaction remains the dominant process. In the case of ^{17}Ne the level scheme was determined by the ^{3}He(^{20}Ne,^{17}Ne)^{6}He reaction. However, for the next interesting case (the ^{18}Ne(2p,γ)^{20}Mg reaction) the level scheme of ^{20}Mg could not be obtained so easily with such a multi-neutron transfer reaction, since the last stable Mg isotope is ^{24}Mg. The ^{20}Mg(γ,2p)^{18}Ne reaction would be the best way to study the excited states in ^{20}Mg. The experimental procedure needed in this case would be comparable with the present studies.

7.2 Future 2p-Spectroscopy Experiments

The intensity upgrades at the radioactive beam facilities worldwide will produce much higher secondary beam intensities to study those nuclei. This will allow to study very small 2p-decay branches like in ^{17}Ne as well as to study heavier systems, like ^{48}Ni which are so far only accessible in rates of one particle/week. The experiments will mainly depend on properties such as the lifetime and the Q-value of the 2p-decay and the beam properties of the used radioactive ion beam, such as purity, intensity etc. Especially due to the complicated kinematics, experiments will always be customized for each reaction. On the other hand typical setups for future experiments can be defined already at present. The main criterium defining the technique of choice is the lifetime of the 2p-decay. In the following section, two new techniques for two different lifetime regions will be discussed together with the production mechanism for the radioactive species.

7.2.1 Production Mechanism

Two methods are currently available to produce radioactive ion beams: Projectile fragmentation, which was used in all the described experiments to produce the ^{17}Ne projectiles and the ISOL-technique, briefly described in section 3.1. A detailed comparison of those two methods is given in [Ria00]. When selecting the suitable production method for a given isotope, lifetime considerations are of crucial interest. For e.g. Nickel isotopes the extraction times are rather large. From experiments at ISOLDE (CERN) the release curve for $^{67-70}$Ni was fitted with a rise time of 0.2 s [Kos00]. The extraction time for ^{48}Ni, a possible ground state 2p-emitter, should be similar. The production time with the method of projectile fragmentation is around 1μs, basically determined by the flight path from the production target to the experiment and by the velocity of the fragments. If the lifetime of ^{48}Ni would be shorter than $\simeq$ 0.2 s it could only be produced via projectile fragmentation. Moreover, the release times in ISOL-facilities depend on the chemistry of the elements, which means that each radioactive ion beam has to be considered individually. For cases like ^{17}Ne, where the projectile needs to be excited in a secondary target, both techniques can be applied.

7.2.2 Setup for Lifetimes τ_{2p} Shorter than $\simeq$5 ns

An extension of the search for the simultaneous 2p-decay in ^{17}Ne to longer lifetimes will be possible soon after the intensity upgrade at the National Superconducting Cyclotron Laboratory [Mor97], providing a factor of 100 more intensity for a ^{17}Ne beam. With up to $2 \cdot 10^6$ ^{17}Ne particles/s it will not be possible to use the same setup as described for the present experiment due to rate limitations in the detectors. A solution can be to use a setup which bends away the secondary non-reacting beam. This could be done by placing the target inside a dipole magnet as it is proposed in the sketch in Fig. 7.1. After passing the target, the non-reacting secondary beam is deflected into a suitable beam dump, while the ^{15}O fragments are bent into a magnet spectrograph. The protons, which will be bent even more, will be detected in a charged particle array, which could consist of a ΔE-E telescope similar to the used one in the present experiment. This setup would not only allow for higher beam currents, it would also avoid breakup reactions in the detectors. The magnet needed is currently built at the NSCL and can be used in combination with the S800 magnet spectrograph [Yur99]. The geometry of the magnet would even allow for the use of γ-detectors in order to perform combined γ-decay studies. This method is basically limited by the lifetime of the 2p-decay. A lifetime of 5 ns

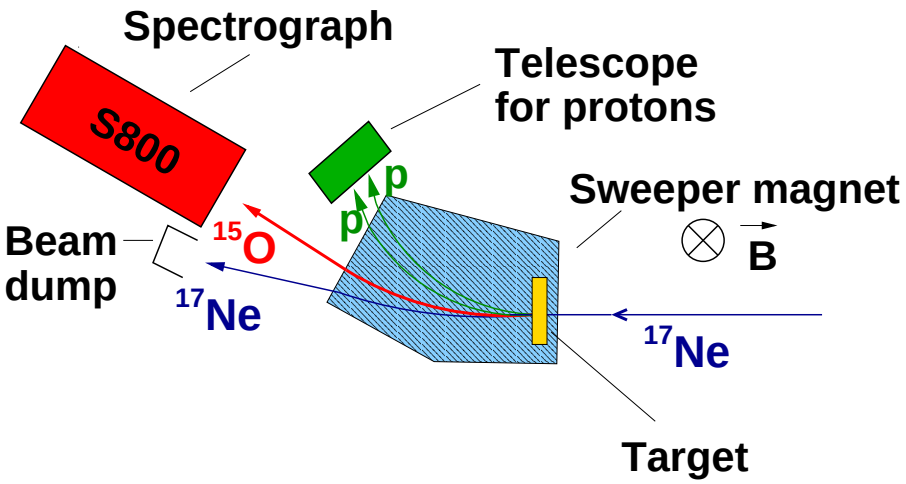

Figure 7.1: Proposed setup for future studies of ^{17}Ne. The target is placed at the entrance of a dipole magnet. The secondary beam is bent into a beam dump, while the heavy fragment is detected in a magnet spectrograph, for example the S800-spectrograph at the NSCL. The protons, which are bent even more, will be detected in a particle telescope similar to the one which was used here.

would correspond to a flight path up to $\simeq$ 50 cm, assuming the same beam velocity as used in the presented experiment. Thus most of the breakup reactions would happen far behind the target and the whole kinematic would become much more difficult and would require sophisticated particle tracking even through the magnetic field. This setup would also be applicable to study ^{19}Mg, another candidate for simultaneous 2p-emission [Gri00], although the width of the intermediate state in ^{18}Na might be too broad [Aud95], so that the decay would probably proceed sequentially. To study ^{19}Mg a secondary ^{20}Mg beam would be bombarded on to a secondary target to strip off the last proton, similar to the production of ^{12}O [Kry95].

7.2.3 Setup for Lifetimes τ_{2p} Longer than $\simeq$ 500 ns

For longer lifetimes the experimental procedure would be much more complicated. A prominent candidate is ^{48}Ni, which has been observed just recently [Bla00]. A comparison of the number of observed and expected counts yields in a lower limit of 0.5 μs for the 2p-decay of ^{48}Ni. By using barrier penetration calculations this value translates into an upper limit for the Q-value of 1.5 MeV. In Fig. 7.2 the calculated 2p half-life is plotted against the Q-value for the 2p-decay. The predicted values can be fitted by the dashed-dotted curve which is then used to translate the lifetime limit into a Q-value limit.

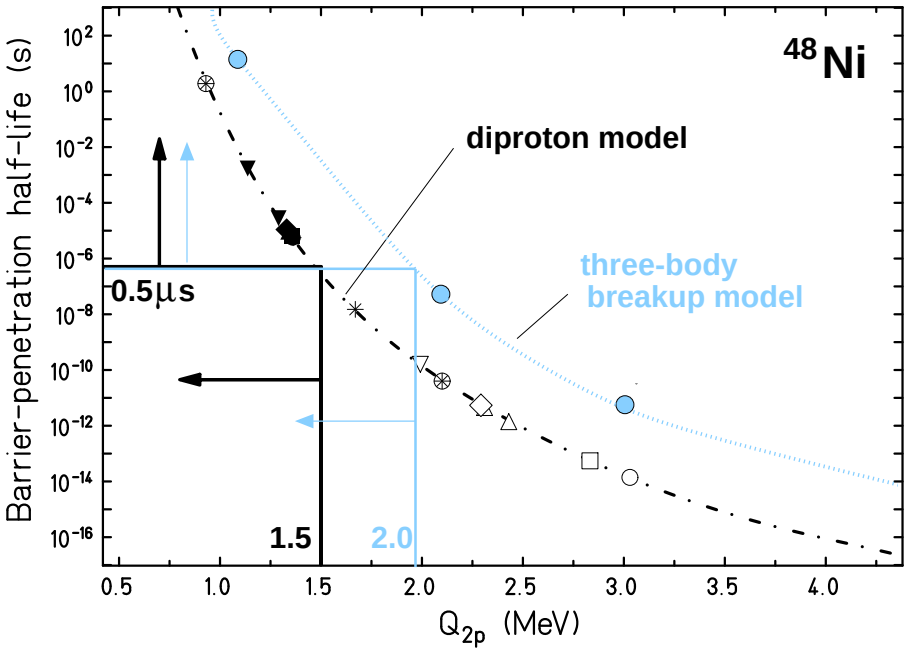

Figure 7.2: Lifetime limits for the 2p-decay of ^{48}Ni. The experimentally obtained lifetime limit [Bla00] is translated into a Q-value by using the diproton model (dashed-dotted curve). The symbols represent Q-value predictions by various models (see [Bla00] and references therein). From the experimental lower limit on the lifetime of the 2p-decay $\tau_{2p} \geq 0.5\mu$s and the relation between the Q-value and τ_{2p} represented by the black dashed-dotted curve an upper limit on the Q-values $Q_{2p} \leq 1.5$ MeV was derived by [Bla00], indicated by the black solid lines and the black arrows. The blue circles and the dotted curve represents the results of the lifetime calculations performed with the three-body breakup model [Gri00]. This would increase the upper limit for the Q-value to $Q_{2p} \leq 2$ MeV.

The new three-body breakup model [Gri00] shifts this curve to larger values, which results in a new Q-value limit of 2 MeV. In order to study the 2p-decay of ^{48}Ni with a lifetime limit of $\tau_{2p} > 0.5$ μs, the ^{48}Ni has to be implanted, preferably into a silicon detector, as it was done in single proton-spectroscopy experiments before (e.g. [Sew97]). So far it was necessary to wait for the processing of the implantation signal before detecting the decay. Thus, one could only study decays with lifetimes longer than some microseconds. A new development by the Oak Ridge group [Ryk01] allows to record particle decays as fast as 0.5 μs after the implantation of the recoil or fragment. The technique is based on the digitization and pulse shape analysis of the particle signals. With this technique one could measure the Q-value of the 2p-decay of ^{48}Ni and its lifetime would be accessible. A sequential nature of the 2p-decay could only be detected if the second decay occurred a substantial amount of time after the first decay. Furthermore, other information about the decay process

such as the relative energy difference of the protons and the angular correlation would not be accessible with this technique, because the protons would not be able to leave the detector after the implantation since all their kinetic energies, determined by the Q-value, would be too small. Hence, the protons would be detected in the same detector segment and in case of a simultaneous 2p-decay at the same time. This technique would only be applicable for lifetimes much shorter than 0.5 μs if the pulse shape analysis technique could be pushed to even shorter time differences between the implantation and the decay. For lifetimes with 5 ns $< \tau_{2p} <$500 ns none of the described techniques would be applicable. In those cases the isotopes could only be produced via fragmentation reactions, which means that they would travel between 1 and 100 meters in one lifetime, which is too far for direct detection and too fast for implantation techniques. Perhaps the use of decelerated beams together with some sort of time projection chambers will allow for those studies. However, with the current techniques one can study already a broad range of nuclei and potential candidates for the simultaneous 2p-decay.

7.2.4 Consequences for the Search for the Simultaneous 2p-Decay in ^{17}Ne

As discussed in section 1.3, lifetime predictions for the simultaneous 2p-decay of the $\frac{3}{2}^-$ state in ^{17}Ne cover a range up to 470 ns (Tab. 2.2). With the experimental limit of $\tau_{2p} > 26$ ps the lifetime could fall in a range that is three orders of magnitude wide. Using the setup described in section 7.2.2 and the intensity (increased by a factor of $\simeq 100$ for ^{17}Ne) after the completion of the Coupled Cyclotron Project at the NSCL [Mor97] it should be possible to extend the search for the simultaneous 2p-decay in ^{17}Ne up to the experimental lifetime limit of the method described in Fig. 7.2.2 of $\simeq 5$ ns. This search would be the next logical step in the search for the simultaneous 2p-decay of the first excited state in ^{17}Ne. In general the present experiment demonstrated the importance of particle tracking for those experiments. Considering a setup as described in Fig. 7.2.2 with bent trajectories due to the magnetic field an accurate tracking comes even more important. Redundant measurements of the trajectories and especially the backwards tracking will be essential. On the other hand, and this has also been demonstrated by the present experiment, each detector even if just used for tracking purposes can cause a significant background, which has to be identified in order to generate a clean decay energy spectrum.

Bibliography

[Ald56] K. Alder *et al.*, Rev. Mod. Phys. **28**,432 (1956).

[Ald75] K. Alder and A. Winther, Electromagnetic Excitation (North-Holland, Amsterdam, 1975).

[Ajz91] F. Ajzenberg-Selove, Nucl. Phys. **A523**, 38 (1991).

[Any74] N. Anyas-Weiss *et al.*, Phys. Rep. **12**, 201 (1974).

[Aud95] G. Audi and A.H. Wapstra, Nucl. Phys. **A595**, 409 (1995).

[Aud97] G. Audi *et al.*, Nucl. Phys. **A624**, 1 (1997)

[Azh98a] A. Azhari *et al.*, Phys. Rev. C **57**, 628 (1998).

[Azh98b] A. Azhari *et al.*, Phys. Rev. C **58**, 2568 (1998).

[Bar88] J. Barrette *et al.*, Phys. Lett. B **209**, 182 (1988).

[Baz92] D. Bazin *et al.*, Phys. Rev. C **45**, 69 (1992).

[Ben79] W. Benenson and E. Kashy, Rev. of Mod. Phys. **51**, 527 (1979).

[Bla00] B. Blank *et al.*, Phys. Rev. Lett **84**, 1116 (2000).

[Ber88] C.A. Bertulani,G. Baur, Phys. Rep. **163**, 299 (1988).

[Bev92] P.R. Bevington and D.K. Robinson, Data reduction and error analysis for the physical sciences, WCB McGraw-Hill, Boston (1992).

[Boh98] A. Bohr and B. Mottelson, Nuclear Structure (World Scientific Publishing Co. Pte. Ltd, 1998), Vol. II.

[Bro77] B.A. Brown *et al.*, Nucl. Phys. **A277**, 77 (1977).

[Bro82] B.A. Brown *et al.*, Phys. Rev. C **26**, 2247 (1982).

[Bro87] B.A. Brown *et al.*, Nucl. Phys. **A474**, 290 (1987).

[Bro91] B.A. Brown *et al.*, Phys. Rev. C **43**, R1513 (1991).

[Bro01] B.A. Brown, private communications.

[Buc92] B. Buck *et al.*, Phys. Rev. C **45**, 1688 (1992).

[Chr97] M.J. Chromik *et al.*, Phys. Rev. C **55**, 1676 (1997) and references therein.

[Chr98a] M.J. Chromik, diploma thesis, Ludwig-Maximilians-Universität München (1998), unpublished.

[Chr98b] M.J. Chromik *et al.*, AIP Conference Proceedings **455**, 286 (1998).

[Chr99] M.J. Chromik *et al.*, AIP Conference Proceedings **481**, 187 (1999).

[Chr00] M.J. Chromik, "PBREAK" was written to fully simulate the detector repsonses as in the experiments 95045 and 98019. The decay kinematics was taken from the simulation code, originally written by R.B. Kryger and modified by P.G. Thirolf, NSCL/MSU.

[Dav96] C.N. Davids *et al.*, Phys. Rev. Lett **76**, 592 (1996).

[Dav98] C.N. Davids *et al.*, Phys. Rev. Lett **80**, 1849 (1998).

[Fae94] A. Faessler, Nucl. Phys. **A570**, 39c (1994).

[Fox89] R. Fox *et al.*, IEEE Trans. Nucl. Sci. **36**, 1562 (1989).

[Fyn00] H.O.U. Fynbo *et al.*, Nucl. Phys. **A677**, 38 (2000).

[Gla97] T. Glasmacher *et al.*, Phys. Lett. B **395**, 163 (1997).

[Goe95] J. Görres *et al.*, Phys. Rev. C **51**, 392 (1995).

[Gol60] V.I. Goldansky, Nucl. Phys. **19**, 482 (1960).

[Gom01] J. Gómez del Campo *et al.*, Phys. Rev. Lett. **86**, 43 (2001).

[Greta] Proceedings of the conference on nuclear structure at the limits, ANL/PHY-97/1 (1996).

[Gri00] L.V. Grigorenko *et al.*, Phys. Rev. Lett **85**, 22 (2000).

[Gui67] G. Guillaume *et al.*, Nucl. Phys. **A272**, 338 (1976).

[Gui95] V. Gũimaraes *et al.*, Z. Phys. A **353**, 117 (1995).

[Gui98] V. Gũimaraes *et al.*, Phys. Rev. C. **58**, 116 (1998).

[Hab97] D. Habs *et al.*, Nucl. Phys. **A616**, 29c (1997).

[Har81] L.H. Harwood *et al.*, Nucl. Instruments and Methods **186**, 435 (1981).

[Her01] F. Herfurth *et al.*, to be published in Phys. Rev. Lett.

[Hof82] S. Hofmann *et al.*, Z. Phys. A **305**, 111 (1982).

[Hub90] F. Hubert *et al.*, At. Data Nucl. Data Tables **46**, 1 (1990).

[Ibb98] R. Ibbotoson *et al.*, Phys. Rev. Lett. **80**, 2081 (1998).

[Jac75] J.D. Jackson, Classical Elektrodynamics, (Wiley New York) (1975).

[Jan82] J.F. Janni, At. Data Nucl. Data Tables **27**, 150 (1982).

[Kos00] U. Köster, PhD-thesis, Technical University Munich (2000), unpublished.

[Kox84] S. Kox *et al.*, Nucl. Phys. **A420**, 162 (1984).

[Kra87] J. Kramp *et. al.*, Nucl. Phys. **A474**, 412 (1987).

[Kry95] R.A. Kryger *et al.*, Phys. Rev. Lett **74**, 860 (1995).

[Leo94] W.R. Leo, Techniques for Nuclear and Particle Physics Experiments, Springer Verlag (1994).

[Lyn91] G.R. Lynch and O.I. Dahl, Nucl. Instr. and Meth. **B58**, 6 (1991).

[Mad01] V. Maddalena *et al.*, Phys. Rev. C **63**, 024613 (2001).

[Mar00] K. Markenroth *et al.*, Phys. Rev. C **62**, 034308 (2000).

[May83] T. Mayer-Kuckuk, Kernphysik, 4.Aufl.,
B.G. Teubner Verlag Stuttgart (1984).

[Mcg73] J.B. McGrory and B.H. Wildenthal, Phys. Rev. C**7**, 974 (1973).

[Men70] R. Mendelson *et al.*, Phys. Rev. Lett. **25**, 533 (1970).

[Mor97] D.J. Morrisey *et al.*, Nucl. Phys. **A616**, 45c (1997).

[Mot95] T. Motobayashi *et al.*, Phys. Lett. B **346**, 9 (1995).

[Muk98] I. Mukha *et al.*, Nucl. Phys. **A630**, 394c (1998).

[Mus95] G. Musiol *et al.*, Kern- und Elementarteilchenphysik, 2.Aufl.,
(Verlag Harri Deutsch, Frankfurt a. Main) (1995).

[Oli00] J.M. Olivera *et al.*, Phys. Rev. Lett. **84**, 4056 (2000).

[Oza94] A. Ozawa *et al.*, Phys. Lett. B **334**, 18 (1994).

[Ram87] S. Raman *et al.*, At. Data Nucl. Data Tables **36**, 1 (1987).

[Ray88] J. Raynal, Computer code ECIS 88, unpublished.

[Ria00] The White Paper of the RIA 2000 workshop and references therein. Available at:www.nscl.msu.edu/conferences/riaws00/home.html.

[Rog74] D.W.O. Rogers *et al.*, Nucl. Phys. **A226**, 424 (1974).

[Ryk01] K. Rykaczewski *et al.*, Nucl. Phys **A682**, 270 (2001).

[Sch96] H. Scheit *et al.*, Phys. Rev. Lett. **77**, 3967 (1996).

[Sch98] H. Scheit, PhD-thesis MSU, East Lansing (1998).

[Scn96] R. Schneider, PhD-thesis, Technical University Munich (1996), unpublished.

[She92] B.M. Sherrill *et al.*, Nucl. Instrum. Methods Phys. Res. **70**, 298 (1992).

[Sew97] D. Seweryniak *et al.*, Phys. Rev. C **55**, R2137 (1997).

[SMAUG] S.R. Hanchar, MSU Software.

[Sta92] The STAR Collaboration, LBL Pub-5347 (1992).

[Suo90] T. Suomijärvi *et al.*, Nucl. Phys. **A509**, 369 (1990).

[Swa94] D. Swan *et al.*, Nucl. Instrum. Methods Phys. Res. **A348**, 314 (1994).

[Tan95] I. Tanihata *et al.*, Nucl. Phys. **A583**, 769 (1995).

[Til93] D.R. Tilley and H.R. Weller., Nucl. Phys. **A588**, 161c (1995) and references therein.

[ToI96] *Table of Isotopes*, 8th ed., edited by R.B. Firestone and V.S. Shirley (Wiley, New York) (1996).

[War92] E.K. Warburton and B.A. Brown, Phys. Rev. C **46**, 923 (1992).

[Wei34] C.F.v. Weizsäcker, Z. Phys. **88**, 612 (1934).

[Wil34] E.J. Williams, Phys. Rev. **45**, 729 (1934).

[Wil96] K. Wille, Physik der Teilchenbeschleuniger und Synchrotronstrahlungsquellen, (Teubner, Stuttgard, 1996).

[Win79] A. Winther and K. Alder, Nucl. Phys. **A319**, 518 (1979).

[Woo95] P.J. Woods *et al.*, Proposal for CYCLONE, Louvain-la-Neuve 1995, unpublished.

[Woo97] P.J. Woods, and C.N. Davids, Ann. Rev. Nucl. Part. Sci. **47**, 541 (1997).

[Won90] S.S.M. Wong, Introductory Nuclear Physics, (Prentice-Hall, Inc., New Jersey)(1990).

[Yur99] J. Yurkon *et al.*, Nucl. Instr. **A422**, 291 (1999).

[Zhu95] M.V. Zhukov and I.J. Thompson, Phys. Rev. C **52**, 3505 (1995).

Acknowledgements

First of all I would like to thank my "Doktorvater" Prof. Dietrich Habs for supporting my thesis project in all aspects. In our discussions you put our results always to the hardest test, most of the times resulting in improvements in the analysis and understanding of the results. Thanks for giving me the freedom to choose, plan and execute this project and for supporting my long term stays in the US.

Special thanks goes to Prof. Michael Thoennessen for his enormous support from the US-side in all phases of my thesis projects. Especially during the planing and setup time. Thanks for the many discussions about handball and the analysis in your office or via phone and email, your suggestions and your input in this work. I enjoyed joining your group during my stays at the NSCL, our beamtimes ending with the sunrise in the hallway of the cyclotron were always the best. Thank you for organizing always support for my housing at MSU, especially during my stay in June 1999 and for setting me up for the PACIFICHEM 2000.

I thank Peter Thirolf for being my "mentor" in Munich, for having always an open door and for listening to my most recent struggles in the analysis and suggesting solutions and for proofreading my thesis. I guess you used a couples of pens for the corrections, I will keep this copy! Thank you for teaching me so much about experimenting and of course for setting me up with the 2p-spectroscopy back in 1996. Thanks for the outstanding help during the experiment at MSU, I remember what a hard job it was to send you home to take a break after a long night shift. From the experiments in Munich I know meanwhile, that you could have stayed awake for another day or two. Thanks for reminding us of the other existing segmented PIN diodes hidden somewhere in some secret cabinets!

I thank all the other "Big Uglies" and Joann Prisciandaro for participating

and helping before and during the experiment and Patrick Lofy for giving our collaboration this nickname. Without Tom Davinson and Phil Woods, our World Champions in DSSD instrumentation, the experiment would have not been feasible. It was great to be able to rely on you. Phil, I think by being the person bringing you the news about ManU's 2:1 victory (by scoring two simultaneous goals) against Munich I gave you something back in return.
I thank the students from the NSCL, Eric Tryggestad, Paul Heckman and Joann Prisciandaro for their help. Joann, thanks for giving us your DSSD. Now I can tell you that we placed your DSSD in front. ;−)
Eric and Paul, thank you for great help in so many details during the setup and the experiment. You two were like the offensive linemen, keeping all troubles away from me. You two took over many boring jobs like looking for special adapters, connectors and screws. But you always would find a solution. If I would have asked you for BNC-2-CF140 adapter, I am sure you would have digged it out.
Thank goes also to David Gassmann and Peter Reiter for coming to East Lansing to participate in the experiment and for dedicating their expertise and so much time.
I guess for inventing the mechanical steerer "g206ms" we really deserve our nickname.
Jeff Stetson:"A bello is not an optical element."
"But a hammer is!" (The Big Uglies!)

I thank Alex Brown for the long discussions and for performing shell model and lifetime calculations for ^{17}Ne.

I thank the Staff in Munich for the support, especially Alfred Kolbe for the design work and the machine shop for building the parts in time for the experiment.
Special thanks goes to Otto Schaile, who made it possible to convert the MSU-data into ROOT format and to implement the analysis routines written for the NSCL analysis system into a new analysis package for ROOT. To be allowed to call him at his cell phone at evening hours or during weekends and to receive always prompt help, for sure speeded up my work.

During the preparation and the execution of the experiments I received an outstanding support from the NSCL staff. Special thanks goes to Len Morris, for taking care of our last minute changes in the experimental design, John Yurkon for helping us with the setup and the trouble shooting of the CRDC's (and there were a lot of troubles to shoot...), Jeff Stetson and Mathias Steiner for developing the radioactive beam, the operators for finding the optimum compromise between our desires and the radiation safety concerns, Ron Fox for the help with the data acquisition and Barb Pollack for given me more and

more disc loan and never taking it back again. For sure the NSCL's success is based on this highly motivated staff. Where else can one find a welder in the machine shop willing to do a welding job at 6pm on a Friday. In most places in the world one wouldn't even find the welder.

Due to the international nature of this project I had the pleasure to be at home in two institutes, the Lehrstuhl of Prof. Habs and the NSCL. I thank all fellow students and assistants in Munich for creating this nice environment. At least sometimes we managed to have a break all together resulting in nice skiing trips (sorry that I missed the last one) and in outstanding visits of the Oktoberfest. I enjoyed our daily breaks at lunch, most of the time resulting in controversial discussions. Thank goes to my "running mates" Peter and Tobias for the many runs together along the Isar. I guess we pushed each other quite a bit. Tobias thanks for the many runs from km 130.0 to 125.0 and back. I enjoyed our conversations during the warm up to km 125.0 as well as the race back. I benefitted from those runs in many ways and I am looking forward to our annual races! And then there was my officemate David, we shared this huge office, our struggles and little successes for many years. It was really a nice working atmosphere with the possibility to take a break whenever we wanted it for a little talk. I promise not to stop Your career in the CSU by reporting Your true opinions to the headquarters. After all I think that it's good that the HSV stepped back this year in the championship race. You wouldn't have deserved such a punishment at all. The "Gottesbeweis" from Barcelona was already hard enough for you. I am writing this acknowledgements three days after Bayern München clinched a back-2-back-2-back national title and one day before the final of the Champions League. So I don't know yet, who will be laughing tomorrow.

But also at MSU I spend beautiful times. I guess I have to start with the fabulous lunch group, including Rich, Navin and sometimes Anu, Andreas, Tom, Takashi, Theo, Yorick, Stephane, Heiko, when he managed to get up before lunch and of course "unser kleines Luder" Marielle. Until now she didn't get a correct translation for this nickname and I hope nobody will ever tell her. Sharon and Rich, thank You for the many invitations to your place. The fact that we all met again about a year later in Nice is a sign that we really were more than just a lunch group. The second institution was the Peanut Barrel crew, which changed a lot since my first stay at the NSCl 1995. But the burgers stayed the same! It took about four years until Eric and I combined our favourite burgers "the Chicken Rodeo" and the "Chicken 'Shroom" to the famous "Chicken 'Shroom w/ Bacon on rye, with swiss and fries". I hope they gonna put it on the menu. The creation of this Burger was one of several legendary moments with Eric: The last game of the BIG TEN Basketball championship 1999 with MSU reaching the second step of a backtobacktobacktoback

(current status) BIG TEN championship, celebrating A.J. Granger and the final four appearance in Atlanta and of course the unforgettable Euro School 2000. The other unforgettable time I spend with most of you was for sure the Enam'98 in Schuss Mountain. Lofy, thanks for reminding me of the "fall guy song". I guess the most unbelievable story about the Enam Eric has to tell, so i am looking forward to your acknowledgements. (I am not talking about the Swedish umpire...). Thanks to Heiko and Jac for offering 305, 407 or whatever apartment number that was. Thanks to Valentina and Marilena, for the many nice hours within the Italian Club and your place in Jolly Road.
During most of my stays, I stayed in Don's, and was always a welcome guest again. You were the only person in that office I could really talk to... . ;−) Thank you for buying the "Bismarck", when I finally left, I guess you got a great deal and I am glad that you sold it to a NSCL member when you left, so we kept the boat for at least four generations in the lab.

Well, now I need to say something about Heiko. Similar you started the part of your acknowledgements when you were talking about me. I guess I could copy your words one by one and just exchange our names, except that I didn't appreciate your soccer expertise, because you didn't know anything about soccer. I learned many experimental tricks from you and appreciated your suggestions for my setup. We spent long times together in East Lansing during my various stays and I really enjoyed our trips to the RIV as much as you did. Thank you for selling me the Bismarck for such a great price, the car was really worth it. It was even running without any oil. During the years in the states you lost your east German accent, but your desperate tries to order a "pork burrito" at this Mexican place will be unforgettable. I still think that the "Driftellipsen-method" was the best result of all our discussions.

I am thankfull for the support of the Studienstiftung des deutschen Volkes during my PhD studies.

Lebenslauf

Persönliche Daten

Name:	Chromik
Vorname:	Marcus Johannes
Adresse:	Luisenstr.67a
	80798 München
Geburtsdatum:	13.05.1972

Schulausbildung

08/78 - 07/80	Klaus-Groth-Schule Husum (1. und 2. Schuljahr)
08/80 - 07/82	Reventlouschule Kiel (3. und 4. Schuljahr)
08/82 - 05/91	Kieler Gelehrtenschule, altsprachliches Gymnasium
05/91	Allgemeine Hochschulreife

Zivildienst

08/91 - 10/92	Zivildienst als staatl. geprüfter Rettungssanitäter bei der Johanniter Unfall Hilfe Kiel

Hochschulausbildung

10/92 - 09/94	Grundstudium der Physik an der Georgia Augusta in Göttingen
09/94	Vordiplom in Physik (Gesamtnote: sehr gut)
10/94 - 08/95	Studium der Physik (5. und 6. Semester) an der Christiana Albertina zu Kiel
08/95 - 10/96	Aufenthalt am National Superconducting Cyclotron Laboratory an der Michigan State University
11/96 - 06/98	Beendigung des Hauptstudiums an der Ludwig-Maximilians-Universität München
06/98	Diplom in Physik (Gesamtnote: sehr gut) Diplomarbeit: "Anregung und der Zerfall des ersten angeregten Zustands in ^{17}Ne".
08/98	Beginn der Dissertation

Auszeichnungen

11/92 - 06/98	Stipendiat der Studienstiftung des deutschen Volkes
08/95 - 10/96	USA - Stipendium der Studienstiftung des deutschen Volkes
01/99	Promotionsstipendium der Studienstiftung des deutschen Volkes